



Review Article

Optical measurements of the Moon as a tool to study its surface

Y. Shkuratov ^{a,b,*}, V. Kaydash ^a, V. Korokhin ^a, Y. Velikodsky ^a, N. Opanasenko ^a, G. Videen ^c^a Astronomical Institute of Kharkov V.N. Karazin National University, Sumskaya 35, Kharkov 61022, Ukraine^b Institute of Radio Astronomy of NASU, Chervonopraporna 4, Kharkov 61002, Ukraine^c Space Science Institute, 4750 Walnut Street, Suite 205, Boulder CO 80301, USA

ARTICLE INFO

Article history:

Received 8 November 2010

Received in revised form

14 June 2011

Accepted 17 June 2011

Available online 30 June 2011

Keywords:

The Moon
Photometry
Spectrophotometry
Polarimetry
Regolith
Light scattering

ABSTRACT

This survey is a general overview of modern optical studies of the Moon and their diagnostic meaning. It includes three united parts: phase photometry, spectrophotometry, and polarimetry. The first one is devoted to the progress in the photometry of the Moon, which includes absolute albedo determination to refine the albedo scale (e.g., to connect lunar observations and the data of lunar sample measurements) and mapping the parameters of a lunar photometric function (e.g., the phase-angle ratios method) with the aim of making qualitative estimates of regolith structure variations. This part also includes observations of the lunar opposition effect as well as photogrammetry and photoclinometry techniques. In particular, available data show that because of the low albedo of the lunar surface, the coherent backscattering enhancement hardly influences the lunar opposition spike, with the exception of the brightest lunar areas measured in the NIR. The second part is devoted to chemical/mineral mapping of the Moon's surface using spectrophotometric measurements. This section also includes analyses related to the detection of water ice or hydroxyl, prognoses of maturity, and helium-3 abundance mapping. In particular, we examine the relationship between superficial OH/H₂O compounds spectrally detected recently and bulk "water ice" found earlier by the *Lunar Prospector* GRS and *LRO LEND*, assuming that the compounds are delivered to cold traps (permanently shadowed regions) with electrostatically levitated dust saturated by solar wind hydrogen. Significant problems arise with the determination of TiO₂ content, as the correlation between this parameter and the color ratio C(750/415 nm) is very non-linear and not universal for different composition types of the lunar surface; a promising way to resolve this problem is to use color ratios in the UV spectral range. The third part is devoted to mapping of polarization parameters of the lunar surface, which enable estimates of the average size of regolith particles and their optical inhomogeneity. This includes considerations of the Umov effect and results of spectropolarimetry, negative polarization imagery, and measurements of other polarimetric parameters, including the third Stokes parameter. Although these three research divisions have not been developed equally and the numbers of proper references are very different, we try to keep a balance between them, depicting a uniform picture. It should be emphasized that many results presented in this review can be applied to other atmosphereless celestial bodies as well.

© 2011 Elsevier Ltd. All rights reserved.

Contents

1. Introduction	1327
2. Definitions and designations	1328
3. Phase photometry	1330
3.1. Albedo	1331
3.2. Disk function	1332
3.3. Phase function in a wide range of phase angles	1334
3.4. Opposition effect	1335
3.5. Phase ratio imagery	1336
3.6. Phase dependence of color ratio	1338
3.7. Photogrammetry	1340
3.8. Photoclinometry	1340

* Corresponding author at: Astronomical Institute of Kharkov V.N. Karazin National University, Sumskaya 35, Kharkov 61022, Ukraine.
E-mail address: Yuriy_Shkuratov@hotmail.com (Y. Shkuratov).

3.9. Interpreting photometry	1342
4. Spectrophotometry	1343
4.1. Introduction	1343
4.2. Spectral bands in visible and NIR range	1344
4.3. Emission removal from reflectance spectra	1348
4.4. Detecting superficial water	1349
4.5. Chemical prognoses	1352
4.6. Prognoses of mineral abundance and maturity degree	1355
4.7. Mapping of helium-3 abundance	1356
5. Polarimetry	1358
5.1. Positive polarization and deviation from the Umov law	1358
5.2. Spectropolarimetry	1360
5.3. Negative polarization	1361
5.4. Other polarimetric parameters	1363
6. Conclusion	1364
Acknowledgment	1366
References	1366

1. Introduction

The Moon has fascinated mankind throughout the ages. In the time since the existence of civilization, the surface of the Moon can be considered almost unchanged. Much of the lunar surface carries information about events that took place millions or even billions of years ago. In the next decades and centuries, intensive utilization of the Moon may commence. For example, it may become profitable to use its natural resources, in particular, ${}^3\text{He}$ as nuclear fuel. The face of the Moon will gradually change due to human activity. Therefore, the collection of information on the original face of the Moon is of mankind importance for the historical record. Aside from their universal appeal, lunar explorations are interesting for fundamental and applied science.

The aim of lunar explorations is to comprehend the origin and evolution of the Moon, as well as to describe the state of its surface and its interaction with the environment. It is necessary to estimate the chemical compositions of basic geologic formations and the structure of their regolith layers. It is not feasible to obtain enough samples from the Moon to provide global information for this; therefore, planetary scientists search for ways to extrapolate characteristics of lunar samples to any lunar site using remote sensing that includes global optical studies.

The Moon is unique as an astrophysical object in that its samples have been delivered and used for verification and calibration of remote-sensing techniques. For instance, if we believe that some lunar samples are representative of given landing sites, correlations between spectral parameters and chemical/mineral contents can be established and used for estimating the lunar surface composition of non-sampled areas. Optical methods are the most effective in the arsenal of remote sensing. Optical measurements with Earth-based telescopes or spacecraft in lunar orbit would allow the global chemical/mineral mapping of the lunar surface and determination of the surface roughness. The history of such measurements is long and interesting in the context of modern lunar studies.

About 40 years ago during the lunar race, when the American and Soviet lunar missions were being realized, astronomers studying the Moon became witnesses and victims of a great invasion of allied sciences into their field, which was unprecedented in its extent. At that time, many lunar astronomers wished to turn their attention to other astronomical objects; they were justifying the decision that the Moon had become the subject of geology and other sciences. Nevertheless, optical investigations of the Moon continued. In our time the Moon is a topical object of space exploration and still remains attractive for ground-based telescope observations. The methodology of ground-based measurements is often used in space-born experiments.

At present, there is considerable activity in optical studies of the Moon using spacecraft. These studies carried out by the probes *Clementine*, *Lunar Prospector*, *Smart-1*, *Kaguya (Selena)*, *Chandrayaan-1*, *Chang'E-1*, and *Lunar Reconnaissance Orbiter (LRO)* significantly extend our knowledge about the Moon. It is enough to say that *Chandrayaan-1* (Pieters et al., 2009a), *Deep Impact* (Sunshine et al., 2009), and *Cassini* (Clark, 2009) observations of the Moon in the NIR spectral ranges have allowed the determination of water ice and/or hydroxyl near the lunar poles. In modern planetology this perhaps is one of the most resonant discoveries.

The number of different methods for making optical measurements of the Moon is not too large. Electromagnetic radiation scattered from any atmosphereless celestial body, e.g., from the Moon, can be described with four characteristics that are named the Stokes parameters (e.g., Bohren and Huffman, 2004). The first one is the intensity of scattered radiation I . This is the most important parameter, which provides our principal knowledge about the Moon. The second parameter $Q=I_{\perp}-I_{\parallel}$ where I_{\perp} and I_{\parallel} are the intensities of light passing through an analyzer oriented perpendicular and parallelly, respectively, to the scattering plane. Usually Q is used in its normalized form, as the linear polarization degree $P=(I_{\perp}-I_{\parallel})/(I_{\perp}+I_{\parallel})=Q/I$, which characterizes the ability of a surface to polarize the incident, initially unpolarized, solar light. This parameter is potentially useful to analyze the lunar surface structure; however, it is not popular in the planetary-science community. The third Stokes parameter $U=I_{\pi/4}-I_{3\pi/4}$ characterizes the orientation of the polarization plane relative to the scattering plane. The angle of orientation is defined as $\theta=(1/2)\arctan(I_{\pi/4}-I_{3\pi/4})/(I_{\perp}-I_{\parallel})$. This parameter may potentially be useful to indicate the surface anisometry and anisotropy. Ground-based polarimetric observations have shown that the third Stokes parameter of the lunar surface is negligibly small. The fourth parameter $V=I_R-I_L$ is responsible for the circular polarization. The indexes R and L correspond to right and left circular polarization. The degree of circular polarization is defined as $P_C=(I_R-I_L)/(I_R+I_L)=V/I$. Unfortunately, the degree of circular polarization is too small to be studied and used as a tool of surface diagnostic; moreover, this signal is dominated by geometrical factors rather than the physical properties of the lunar surface.

Thus, only the first two Stokes parameters I and P have been used to characterize the lunar surface. These parameters depend on the wavelength λ and phase angle α . This angle is the most important variable in planetary photometry. Measurements of the functions $I(\alpha, \lambda)$ and $P(\alpha, \lambda)$ or their parameters are the gist of lunar optical remote sensing. Accordingly, we distinguish phase photometry (phase polarimetry) from spectrophotometry (spectropolarimetry). Among these four directions, spectrophotometry is the most elaborate as a tool of optical remote sensing. Recently, a

phase photometry technique, also called phase-ratio imagery, is experiencing a surge in development. Unfortunately, polarimetry is still a Cinderella in lunar optical studies; it is enough to say that polarimetry of the Moon never was conducted from lunar orbit.

Although the importance of lunar optical studies is widely accepted, during the last 40 years since the review by Hapke (1971), no overviews of a wide observational and interpretative context were proposed, which might concisely and clearly explain what interesting and useful information about the lunar surface one could learn from photometry, spectrophotometry, and polarimetry, and how lunar observation data correlate with the enormous amount of information obtained from the many space missions.

The main purpose of this paper is to review the current status of optical studies of the Moon in the wide context and to attract the attention of readers to a number of worthwhile observational problems related to the Moon. It should be emphasized that this article is not a full historical review of existing papers on optical observations, but rather a sketch mainly based on the experience of the authors. In this review we consider not only the methods that are providing impressive practical results, like spectrophotometry, but also approaches that satisfy an academician's curiosity and do not yet have effective applications and wide dissemination.

This review consists of three parts. The first part is devoted to lunar photometry including problems of absolute albedo determination, the opposition effect, phase-ratio imagery, and phototopography techniques. In the second part we consider spectrophotometric measurements, problems relating to the detection of water ice and/or hydroxyl on the lunar poles, and color-ratio imaging that allows the determination of chemical/mineral composition. Finally, the third part is devoted to lunar polarimetry, including polarimetric mapping at different phase angles. These three directions of lunar optics are closely connected with each other and, therefore, it seems to be important to consolidate them into one paper.

2. Definitions and designations

There are different sets of angles that characterize the geometry of illumination and observation of a planetary surface. One such a set includes the incident and emerging angles i and e , and azimuth φ that is the angle between the planes of scattering and incidence (Fig. 1). For many applications another set can be used. It includes the so-called photometric (luminance) coordinates α , β , and γ that are the phase angle, and photometric latitude and longitude, respectively. These sets depend on each other as follows (Sharonov, 1964; Hapke, 1993):

$$\begin{aligned} \cos i &= \cos \beta \cos(\alpha - \gamma), \\ \cos e &= \cos \beta \cos \gamma, \\ \cos \varphi &= \frac{\cos \alpha - \cos i \cos e}{\sin \alpha \sin e}, \end{aligned} \quad (1)$$

and

$$\begin{aligned} \cos \alpha &= \cos i \cos e + \sin i \sin e \cos \varphi, \\ \cos \beta &= \sqrt{\frac{(\sin(i+e))^2 - (\cos(\varphi/2))^2 \sin 2e \sin 2i}{(\sin(i+e))^2 - (\cos(\varphi/2))^2 \sin 2e \sin 2i + (\sin e)^2 (\sin i)^2 (\sin \varphi)^2}}, \\ \cos \gamma &= \frac{\cos e}{\cos \beta}. \end{aligned} \quad (2)$$

The combination of the angles α , i , e may be used too.

The first Stokes parameter is associated with the directional luminous intensity $I(\alpha, i, e, \lambda)$ [$\text{W}/\text{m}^2 \text{sr} \mu\text{m}$]. The light flux Φ scattered by a lunar surface element of square S in the observer direction in a solid angle Ω_0 centered in the direction e is

$$\Phi(\alpha, i, e, \lambda) = S \int_{\Omega_0} I(\alpha, i, e, \lambda) d\Omega. \quad (3)$$

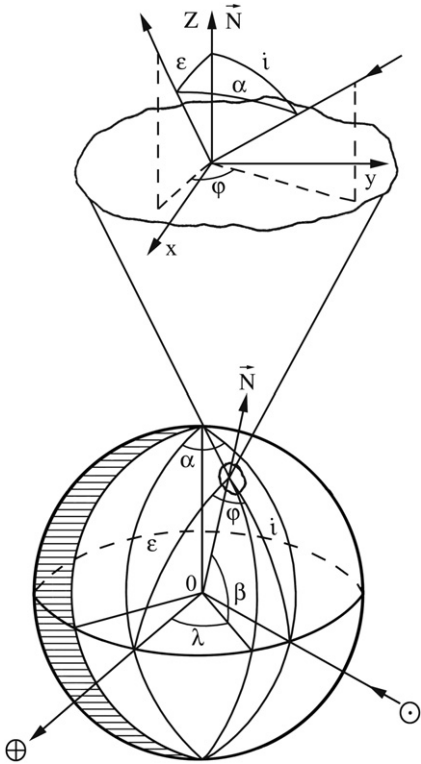


Fig. 1. Designations of the angle variables i , e , and φ as the angles of incidence, emergence, and azimuth, respectively. The photometric coordinates α , β , and γ are phase angle, photometric latitude, and photometric longitude, respectively.

The function $\Phi(\alpha, i, e, \lambda)$ is experimentally measurable. Both $\Phi(\alpha, i, e, \lambda)$ and $I(\alpha, i, e, \lambda)$ are symmetric relative to the permutation of i and e , i.e., satisfy the Helmholtz reciprocity principle (Minnaert, 1941). The directional luminous intensity may be presented as

$$I(\alpha, i, e, \lambda) = E_0(\lambda) r_0(\lambda) F(\alpha, i, e, \lambda), \quad (4)$$

where $E_0(\lambda)$ is the normal incident solar irradiance, $r_0(\lambda)$ is the so-called normal reflectance at a given wavelength λ , and $F(\alpha, i, e, \lambda)$ is the photometric function. The surface brightness is

$$B(\alpha, i, e, \lambda) = I(\alpha, i, e, \lambda) / \cos e \quad (5)$$

and this parameter should not be confused with the brightness coefficient, that is

$$\Gamma(\alpha, i, e, \lambda) = \frac{F(\alpha, i, e, \lambda)}{\cos i \cos e}. \quad (6)$$

This coefficient also is symmetric relative to the permutation of i and e .

As a rule the function $F(\alpha, i, e, \lambda)$ explicitly includes factors $\cos i$ and $\cos e$ that may be canceled in the numerator and denominator of Eqs. (5) and (6) (e.g., Hapke, 1993). For instance, for the Lambert law $F \sim \cos i \cos e$ and for the Lommel-Seeliger law $F \sim \cos i \cos e / (\cos i + \cos e)$. However, this is not universal, e.g., the Akimov law does not include these cosines (see below).

The surface bidirectional reflectance is defined as (Sharonov, 1964; Hapke, 1993)

$$r(\alpha, i, e, \lambda) = I(\alpha, i, e, \lambda) / E_0 \cos e. \quad (7)$$

If the photometric function is normalized $F(0, 0, 0, \lambda) = 1$ at $\alpha = i = e = 0$, formulas (4) and (7) yield the normal reflectance

$$r_0(\lambda) = r(0, 0, 0, \lambda) = I(0, 0, 0, \lambda) / E_0(\lambda). \quad (8)$$

Measurements of the normal reflectance $r_0(\lambda)$ requires observations exactly at $\alpha = 0$. Such measurements are difficult for the Moon. For Earth-based observations phase angles $< 1^\circ$ are

impossible because of lunar eclipses. Spacecraft may provide data at smaller α , but the Sun illuminating the Moon has an angular radius of 0.25° , which is the minimal phase angle in photometry of the Moon. Extrapolations of phase curves to zero α are possible, but not reliable, since the amplitude of the opposition effect, manifesting itself as a non-linear increase of brightness when α approaches zero, varies over the lunar surface.

For ideally conductive and flat metallic surfaces the parameter $r_0(\lambda)=1$ at $\alpha=i=e=0$. However, if a surface scatters incident radiation diffusely even without absorption, this parameter is significantly smaller, since not all scattered rays meet the condition $\alpha=i=e=0$. It is more convenient in planetary photometry to use ideally diffusing surfaces for comparison rather than ideally conductive metals with a flat interface. In this case, the parameter called albedo is used. There are several different albedos. The hemispherical (or flat) albedo A_h is the ratio of the light flux Φ scattered into the upper hemisphere by a surface that is illuminated by irradiance E_0 . For orthotropic scattering ($\Gamma=1$, see Eq. (6)) without absorption for any λ , which corresponds to an absolutely white Lambert surface

$$A_h = \frac{\Phi}{E_0} = r_0^{Lamb} \int_{e=0}^{\pi/2} \int_{\varphi=0}^{2\pi} \cos e \sin d\varphi de = \pi r_0^{Lamb} = 1. \quad (9)$$

To avoid inconveniences when $r_0^{Lamb} = 1/\pi$, a photometric parameter called the radiance factor $A(\alpha, i, e, \lambda)$ is used (Hapke, 1993). In older papers this parameter was called apparent albedo (e.g., Sytinskaya, 1964; Sharonov, 1964). Unfortunately, now this term that is so natural for planetology is exploited in spacecraft or airplane observations of the Earth landscapes to indicate that the atmosphere influence is not excluded in the albedo measurements (e.g., Qiu et al., 2003); nevertheless, we use the term below. Thus, the apparent albedo is introduced as follows:

$$A(\alpha, i, e, \lambda) = \frac{I(\alpha, i, e, \lambda)}{r_0^{Lamb} E_0(\lambda) \cos e} = \pi r(\alpha, i, e, \lambda) = A_n(\lambda) \frac{F(\alpha, i, e, \lambda)}{\cos e}, \quad (10)$$

where $A_n(\lambda) = A(0, 0, 0, \lambda) = \pi r_0(\lambda)$ is normal albedo.

Thus, the apparent albedo is the surface bidirectional reflectance at arbitrary illumination/observation geometry divided by the reflectance of the Lambertian surface with the normal oriented to the light source. The apparent albedo $A(\alpha, i, e, \lambda)$ relates to the reflectance factor $R(\alpha, i, e, \lambda)$ as $A(\alpha, i, e, \lambda) = R(\alpha, i, e, \lambda) \cos i$ (Sharonov, 1964; Hapke, 1993).

In practice, it is very convenient to use the equigonal albedo $A_{eq}(\alpha, \lambda)$. This value equals the apparent albedo converted to the so-called mirror geometry: $A_{eq}(\alpha, \lambda) = A(\alpha, \alpha/2, \alpha/2, \lambda)$. Using the concept of equigonal albedo, the radiance factor can be naturally factorized:

$$A(\alpha, i, e, \lambda) = A_{eq}(\alpha, \lambda) D(\alpha, i, e, \lambda), \quad (11)$$

where $A_{eq}(\alpha, \lambda)$ describes the phase dependence only, and the disk function $D(\alpha, i, e, \lambda)$ describes the brightness distribution over the lunar disk relative to the mirror point at fixed α . Demonstration of the difference between apparent (a) and equigonal albedo (b) suggests Fig. 2 that presents these values at $\alpha=22.2^\circ$. The scale shows albedo in natural units. As can be seen, the equigonal albedo image has no brightness trend from the limb to terminator.

The function $A_{eq}(\alpha)$ can be expressed as

$$A_{eq}(\alpha, \lambda) = A(\alpha_0, \lambda) f(\alpha, \lambda), \quad (12)$$

where $f(\alpha, \lambda)$ is the phase function normalized to unity at $\alpha=\alpha_0$ and $A(\alpha_0, \lambda)$ is the equigonal albedo value at $\alpha=\alpha_0$. When $\alpha_0=0$, $A(\alpha_0, \lambda)$ is the normal albedo $A_n(\lambda)$. The factor $A(\alpha_0, \lambda)$ is the absolute apparent albedo measured in % at α_0 . This albedo contains information about absorption of light in the lunar regolith, while the normalized phase dependence $f(\alpha, \lambda)$ allows one to study the shadow-hiding effects that are controlled by the regolith structure.

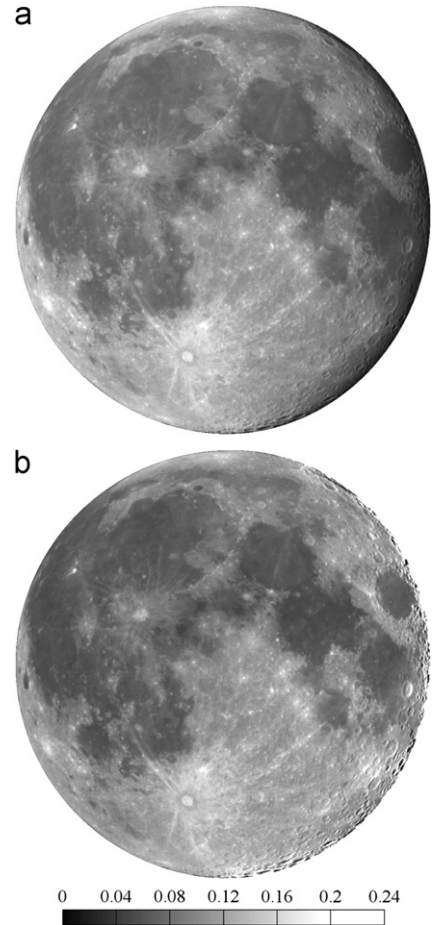


Fig. 2. (a) Apparent albedo and (b) equigonal albedo maps at $\alpha=22.2^\circ$ and $\lambda=603$ nm. The equigonal albedo was computed from apparent albedo using Eq. (19).

Fig. 3a shows results of phase photometry of the Moon in the visible spectral range. The phase curve is normalized to 1 at $\alpha=10^\circ$. We here combine the Clementine (Shkuratov et al., 1999a) and Earth-based integral (Rougier, 1933) data at $\lambda=0.43 \mu\text{m}$. We consolidated the integral telescope data with the average Clementine measurements using the factor of sphere self-shadowing $(1+\cos \alpha)/2$ (Muinonen et al., 2002). As one can see, the Moon demonstrates prominent backscattering over a wide range of phase angles; the brightness peak near small phase angles is a manifestation of the opposition effect.

Fig. 4 presents the average spectral dependence of equigonal albedo ($\alpha=6^\circ$) for mare and highland areas. These curves were obtained using Pieters' lunar spectral catalog that were processed and calibrated in Shkuratov et al. (2001). The spectra depicted in Fig. 4 show a monotonic growth with wavelength in the visible and NIR range. Two weak absorption bands corresponding to pyroxenes are seen near 1 and $2.2 \mu\text{m}$; pyroxene is one of the main rock-forming minerals in lunar maria.

Sunlight is unpolarized to a level of sensitivity of 10^{-6} (Kemp et al., 1987). This restricts the possibilities of polarimetric analysis that is applied in ellipsometry when incident light can be polarized, as necessary for experiments (e.g., Azzam and Bashara, 1977). Nevertheless, studying the phase and spectral dependence of the linear polarization degree of the Moon is fairly interesting and informative. Fig. 3b depicts phase curves of the polarization corresponding to integral measurements by Lyot (1929) before and after the full Moon; the curves have minima and maxima at small and large angles, respectively. These

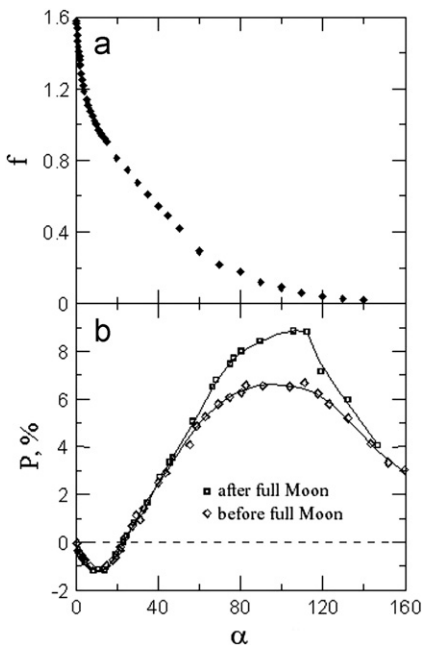


Fig. 3. (a) Phase-angle curves of normalized integral albedo and (b) linear polarization degree of the Moon.

The plots are adapted from Muinonen et al. (2002).

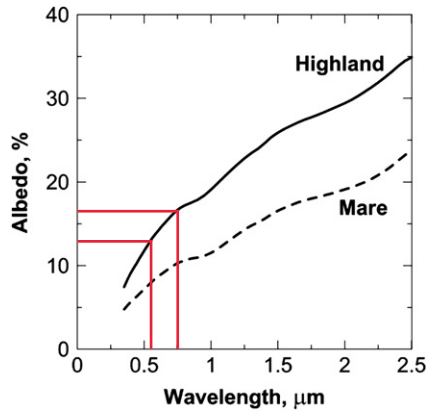


Fig. 4. Reflectance spectra typical of lunar maria and highlands.

features can be characterized with the parameters P_{min} , α_{min} and P_{max} , α_{max} . At pure backscattering the polarization equals zero. When α approaches 180° , the lunar polarization tends to zero, though laboratory studies of powdered glass samples (Shkuratov et al., 1994b) indicate the occurrence of an additional narrow maximum at 170° related to the ray interference at forward single scattering.

It is amazing that the measurements shown in Fig. 3b were carried out visually with a polariscope providing an accuracy of about 0.1%. The difference between the polarimetric curves at large α is caused by different mare/highland proportions for the illuminated eastern and western parts of the lunar nearside. The minimum and maximum depend on the equigonal albedo and structure of the lunar surface layer. The origin of the features is largely related to the single-particle scattering properties of the surface. Multiple incoherent and coherent scattering changes the position and amplitude of the features of the single-particle indicatrix.

Examples of polarimetric spectra $P_{max}(\lambda)$ are shown in Fig. 5 using measurements of Dollfus and Bowell (1971). These spectra

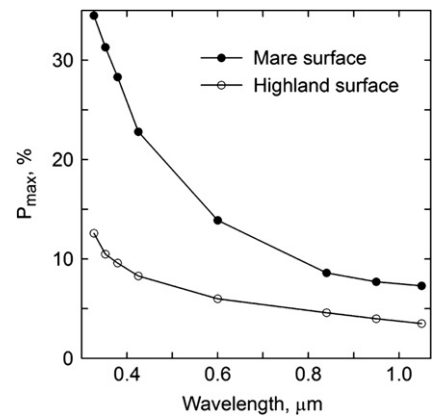


Fig. 5. Spectral dependence of polarization maximum P_{max} according to observations by Dollfus and Bowell (1971).

seem to be inverted when compared to the spectra of equigonal albedo. This is a manifestation of the Umov law, see also (Gehrels et al., 1964). In measuring 14 lunar sites in the spectral range 0.32–1.05 μm , Dollfus and Bowell (1971) found that $P_{max}(\lambda)=k/\lambda^{1.137}$, where k is a constant depending on the lunar site, and depends especially on the albedo. For the illuminated portion of the lunar disk it was found that $P_{max}(\lambda)=0.286A(\lambda)/\lambda^2$, λ being given in microns (Dollfus and Bowell, 1971). Examples of $P(\lambda)$ extended to UV range (180–310 nm) can be found in Fox et al. (1998).

All the dependencies shown in Figs. 3–5 can be parameterized. For example, we could approximate the spectrophotometric and spectropolarimetric curves by a number of respective color ratios $C=A(\lambda_1)/A(\lambda_2)$ or $C_P=P(\lambda_1)/P(\lambda_2)$. By analog, phase ratios can be introduced, $\xi=A(\alpha_1)/A(\alpha_2)$. The polarimetric phase curve is more complicated and its parameterization is more diverse. In addition to the parameters P_{min} , α_{min} , P_{max} , α_{max} , the values α_{inv} , and $h=(dP(\alpha)/d\alpha)|_{\alpha=\alpha_{inv}}$ are often used, where α_{inv} is the angle of change of polarization sign (for the Moon $\alpha_{inv}\approx 2\alpha_{min}$). The derivative is estimated in finite differences.

Sometimes, the experimental dependencies are approximated with a theoretical curve, then the model parameters are calculated using a best-fit procedure. For example, Hapke's (1993) theory is often used for such a fit using phase-photometry data. However, in this case one faces a problem of fitting ambiguity, since different combinations of model parameters may provide almost the same theoretical curves. A philosophical question immediately arises here: What is better, to use a simplified theory with a small number of parameters that can be estimated unambiguously, or to use a more rigorous and complicated theory with a larger number of parameters that cannot be found unambiguously? A solution of the dilemma could be a model with hierarchical parameters, when a few model parameters provide the unambiguous fit, but they are functions several other physical parameters. Anyway, the determination of the model parameters of the lunar regolith is considered as one of the main purposes of remote sensing of the Moon.

3. Phase photometry

Lunar phase photometry has been an important tool in lunar studies, since Galileo Galilei began his first telescope observations. Among the most remarkable photometric properties of the Moon is the unusually strong backscattering of its surface (when α approaches zero), and its appearance as a flat disk rather than a round shiny ball when α is close to zero.

In this section we discuss absolute lunar albedo determination (both apparent and equigonal) focusing on the most recent results. Then we consider the importance of choice of the disk function that describes the global brightness distribution over the lunar disk. Phase-function measurements of lunar brightness and color ratio are also discussed. Recently, lunar photometry has caught a second wind with phase-ratio imagery; we demonstrate this new and prospective tool using ground-based and spacecraft data. We consider also progress in photogrammetric and photoclinometric techniques to retrieve lunar surface topography data. The last part of this section is devoted to theoretical photometry. In particular, we discuss the Hapke model, presenting lunar maps of the model's parameters.

3.1. Albedo

Hereafter, where it is not important, we do not indicate the type of albedo, using barely the word "albedo". This characteristic suggests information about the content of chromophore elements, primarily ions of iron and titanium, in the lunar surface material; another important agent that affects the albedo and spectrum of the Moon is submicroscopic metallic iron in regolith particles. The chromophore elements (Fe and Ti) are transition metals that absorb light in regolith grains, decreasing their transparency. The higher the content of these chromophores, the lower the surface albedo is. Due to this fact lunar maria are darker than highlands. However, in the UV range, regolith particles are not transparent. Therefore, regolith albedo is formed by light reflections from the particle surface. The refractive index of mare material is higher than that of highlands. Hence, the external reflection coefficient of mare regolith particles is larger than in the case of highlands (Henry et al., 1976). Owing to this property the relative brightness of highlands and maria is reversed in the ultraviolet near 120 nm (the line L_α), i.e., the maria are brighter than the highlands. This has been shown using orbital Apollo-17 UV-spectrometer measurements (Henry et al., 1976). At wavelengths near 180 nm the mare/highland contrast is minimal, the apparent albedo values at small phase angles being about 3–4% (Henry et al., 1995).

Compared to other optical characteristics, the distribution of albedo in the visible range is easily accessible for investigation and use. Several apparent albedo maps of the visible lunar hemisphere at small phase angles have been published. For instance, there are the isophote maps by Pohn and Wildey (1970) and Evsyukov (1973a). Now all these maps are of historical interest, since modern albedo maps are presented in digital form; examples are Clementine UVVis albedo data (Eliason et al., 1999). Digital maps provide much higher resolution than those in isophote representation. Their using allows one to consider the terms imagery and mapping as synonyms.

The absolute values of albedo enable comparison of lunar data with laboratory measurements of regolith samples and their analogs, which, in turn, make it possible to develop methods of prognosis of chemical/mineral composition. Knowledge of absolute albedo allows the use of the Moon as a photometric standard for observations of planets and the Earth's surface from space (Kieffer and Wildey, 1996). Photometry of the Earth shine on the Moon is used for the Earth's spectral albedo determinations to improve climate models (e.g., Qiu et al., 2003).

There are few data of absolute lunar photometry. The old Sytinskaya–Sharonov photometric system ($\lambda_{\text{eff}}=548$ nm) uses visual photometry data and calibration with a white screen illuminated by the Sun (Sytinskaya and Sharonov, 1952; Sytinskaya, 1964). The Shorthill et al. (1969) catalog ($\lambda_{\text{eff}}=445$ nm) is based on the Sytinskaya–Sharonov system. The Wildey–Pohn photometric system ($\lambda_{\text{eff}}=548$ nm) uses photoelectric photometry and calibration by

stars (Wildey and Pohn, 1964), which reveals 10–15% higher albedos than those in the Sytinskaya–Sharonov determination. A photometric system (1956/57) of Gehrels et al. (1964) uses photoelectric photometry data ($\lambda_{\text{eff}}=548$ nm) and calibration by stars. This reveals almost the same difference from the Sytinskaya–Sharonov system. The Clementine UVVis reflectance at $\lambda_{\text{eff}}=415, 750, 900, 950$, and 1000 nm (Eliason et al., 1999) is almost two times greater than that of the Sytinskaya–Sharonov system (Hillier et al., 1999; Shkuratov et al., 2001). The Clementine reflectance was estimated using measurements of the spectral reflectance factor $R(\alpha, i, e, \lambda)$ of the representative Apollo-16 soil sample 62231 with the RELAB spectrometer at the following photometric conditions: $\alpha=i=30^\circ$, $e=0^\circ$ (McEwen et al., 1998; Pieters, 1999).

More recent data reveal better agreement with each other. For instance, there exists a database of Earth-based lunar CCD observations that have been calibrated using measurements of the star Vega (Kieffer and Stone, 2005). The RObotic Lunar Observatory (ROLO) of the U.S. Geological Survey observations are carried out for 32 wavelengths in a range from 0.35 to 2.50 μm at phase angles from 1.55° to 97° . Earth-based CCD photometry observations and calibration by the star Vega also were carried out by Saiki et al. (2008); to gain data on lunar reflectance, the authors acquired multi-band images (650, 750, 900, 950, and 1000 nm) using a liquid-crystal tunable filter telescope located on the peak of Mt. Haleakala (Hawaii, USA). A two-month series of quasi-simultaneous imaging photometric observations of the Moon and the Sun has been performed at the Maidanak Observatory (Uzbekistan) to obtain new absolute values of lunar albedo (Velikodsky et al., 2011; <http://astrodatab.univer.kharkov.ua/moon/albedo/>). A comparative analysis of the listed data of absolute photometry shows, e.g., that the observations of Saiki et al. (2008) and Velikodsky et al. (2011) carried out at $\alpha \approx 7^\circ$ are almost coincident. The data obtained by Kieffer and Stone (2005) and Velikodsky et al. (2011) reveal a systematic mutual shift: ROLO's apparent albedo is about 13% lower than that of Velikodsky et al. (2011) and Saiki et al. (2008). The average ratio of the Clementine to Velikodsky et al. (2011) albedo is 1.41. Results of the comparison are presented in Table 1. All data in the table were brought to $\lambda=603$ nm using the average lunar spectra (see Fig. 4). A more detailed comparison of the Kieffer and Stone (2005) and Velikodsky et al. (2011) data is shown in Fig. 6. This figure presents the phase curves of the disk-equivalent albedo that is the average apparent albedo of the lunar disk including the non-illuminated part where the apparent albedo is considered to be zero.

Overestimated albedo measured by Clementine can be explained by the difference of the lunar region used for calibration and the region where sample 62231 was actually collected by the Apollo-16 crew (Station 2). These locations are approximately 10 km apart and differ in albedo by approximately 20%, which may partially compensate for the photometric system difference (Pieters et al., 2009b). Moreover, the phase curve determined in the phase-angle range

Table 1
Comparison of apparent albedo in different photometric systems.

Photometric system	Ratio to Kharkov albedo	σ in relative %
Sytinskaya–Sharonov	0.73	18
Gehrels, 1956/57	0.81	6
Wildey–Pohn	0.86	10
ROLO	0.87	1.5
Saiki	1.00	1(4)
Kharkov	1	2
Clementine	1.41	3

Note: Kharkov corresponds to measurements by Velikodsky et al. (2011), <http://astrodatab.univer.kharkov.ua/moon/albedo>.

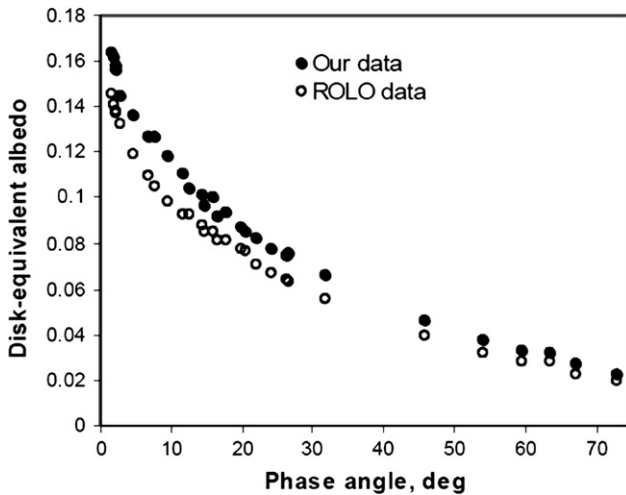


Fig. 6. Comparison of observations by Velikovsky et al. (2011) which are in excellent agreement with the Saiki et al. (2008) calibration with the ROLO (Kieffer and Stone, 2005) data.

0–30° can be somewhat different for the 3 mm laboratory sample in the RELAB measurements and the lunar regions, the brightness of which depends on the shadow effect from the much larger roughness. Another reason for the discrepancy is that reflectance is dependent on porosity (e.g., Hapke, 2008): the Apollo-16 sample measured in the laboratory could be more compacted than in its natural state on the lunar surface.

3.2. Disk function

The brightness distribution over the lunar disk at arbitrary phase angle depends on the intrinsic albedo pattern and global trend caused by the sphericity of the Moon. As a first approximation, disk functions described the trend are considered to be uniform. In fact, each site of the Moon has own disk function. There are two reasons for this. First, the lunar surface is not smooth; its resolvable topography should be taken into account using local angles i and e in the disk function. Second, the character of the disk function should depend on the physical characteristics of the surface, e.g., on its albedo and irresolvable micro roughness. The global brightness trend of the Moon has not been measured sufficiently, so theoretical functions are usually used, typically, the Lommel–Seeliger scattering law normalized to 1 at zero phase angle

$$D_{LS} = \frac{2\cos i}{\cos i + \cos e} = \frac{2\cos(\alpha-\gamma)}{\cos\gamma + \cos(\alpha-\gamma)}. \quad (13)$$

This law is simple and naturally appears in the single scattering approximation of radiative transfer theory in particulate media (e.g., Hapke, 1993). In fact, Lommel–Seeliger's disk function poorly describes the brightness distribution over the lunar disk at various α , e.g., it ignores the lunar surface darkening at the photometrical poles, which is caused by mesoscale topographical influences (Hapke, 1993; Akimov, 1988a). It also reveals a prominent surge at the lunar limb at large α ; however, this law does produce the flat disk effect at full Moon. This can be anticipated, as the law corresponds to single scattering that is independent of the position on the disk at $\alpha=0$.

Producing appreciable distortions of photometric results, the Lommel–Seeliger law, nevertheless, is widely used, e.g., by Hillier et al. (1999) for Clementine data; by Kramer et al. (2010) and Hicks et al. (2010, 2011) for calibration of Chandrayaan-1 M³ data and its comparison with Clementine and ROLO data; by Saiki et al. (2008) to bring apparent albedo distributions to the RELAB

scattering geometry, by Buratti et al. (2011) for future lunar missions, etc. Unfortunately, this law also was suggested for use in "New look at photometry of the Moon" by Goguen et al. (2010).

The best way is to exploit disk functions deduced from more rigorous theoretical models. The Hapke (1993) model is the most popular. However, to use the analytical disk function by Hapke (1993) is unpractical, as the function is cumbersome and not convenient for processing a large amount of data. Therefore, simpler empirical or semi-empirical functions are applied. For instance, the Minnaert disk function is often used

$$D_M = (\cos i)^k (\cos e)^{k-1} = (\cos\beta)^{2k-1} \frac{((\cos((\alpha/2)-\gamma))^2 - (\sin(\alpha/2))^2)^k}{\cos(\alpha/2)\cos\gamma} \quad (14)$$

where k is the Minnaert (1941) parameter. In fact, k is a function of albedo and phase angle. For the Moon the function is $k(\alpha) = (10^{-2}\alpha + 1)/2$ (α is expressed in degrees) (Helfenstein and Vercka, 1987). McEwen (1991, 1996) suggested an approximation in the form of a linear combination of the Lommel–Seeliger and Lambert scattering laws

$$D_{LZ+L}(\alpha, \beta, \gamma) = L(\alpha) \frac{2\cos(\alpha-\gamma)}{\cos(\alpha-\gamma) + \cos\gamma} + (1-L(\alpha))\cos\beta\cos(\alpha-\gamma). \quad (15)$$

Here the balancing factor $L(\alpha)$ decreases from 1 to 0, increasing the contribution of the latitude term with α . On the basis of Galileo images of the Moon, McEwen (1996) proposed the following polynomial approximation for $L(\alpha)$:

$$L(\alpha) = 1 + A_1\alpha + A_2\alpha^2 + A_3\alpha^3 \quad (16)$$

where A_1 , A_2 , and A_3 are constants: $A_1 = -1.9 \times 10^{-2}$, $A_2 = 2.42 \times 10^{-4}$, and $A_3 = -1.4 \times 10^{-6}$ (α is given in degrees). Akimov (1979a, 1988b), using his own photometric observations, proposed the following empirical expression to approximate the lunar disk function:

$$D_A(\alpha, \beta, \gamma) = \cos \frac{\alpha}{2} (\cos\beta)^{v\alpha} \frac{(\cos((\alpha/2)-\gamma))^{v\alpha+1} - (\sin(\alpha/2))^{v\alpha+1}}{(1 - (\sin(\alpha/2))^{v\alpha+1})\cos\gamma}, \quad (17)$$

the parameter $v=0.16$ and 0.31 for maria and highlands at $\alpha < 90^\circ$ (α is presented in radians). Expression (17) somewhat generalizes the Minnaert law (14); it is normalized to 1 at the mirror point ($i=e=\alpha/2$). Functions (15) and (17) predict uniform disk brightness at $\alpha=0$. Eq. (15) has the drawbacks of the Lommel–Seeliger law, e.g., it may produce the limb brightening at moderate α , which is not observed. Akimov's law (17) does not have this shortcoming. Function (17) contains only one free parameter v .

There is an interesting expression for the disk function, which does not contain free parameters, like Lambert and Lommel–Seeliger laws. This was derived from the formal condition that an extremely rough surface being slightly randomly undulated should have the same disk function as before undulations (Akimov, 1976, 1988a; Shkuratov et al., 1994a, 2003a):

$$D_{Theor}(\alpha, \beta, \gamma) = \cos \frac{\alpha}{2} \cos \left(\frac{\pi}{\pi-\alpha} \left(\gamma - \frac{\alpha}{2} \right) \right) \frac{(\cos\beta)^{\alpha/(\pi-\alpha)}}{\cos\gamma}. \quad (18)$$

Such utterly rough surfaces satisfying this condition hardly exist in nature, but they are a good abstraction that provides an excellent approximation of the lunar disk function. We note that Akimov's law produces the flat-disk effect at full Moon, as the law describes very rough surfaces for which at $\alpha=0$ there are enough facets oriented to the observer independently of site position on the disk. This is, in fact, the original explanation of the flat-disk effect at full Moon proposed by Galilei (1638).

Analysis of light scattering by different complex structures leads to the notion about equifinality of a scattering law (Shoshany, 1991), when a significant number of different complex

structures exhibit the same scattering law. For example, the Akimov function can be rigorously derived not only for the case of utterly rough surfaces (Akimov, 1976, 1988a; Shkuratov et al., 1994a), but also for fractal-like surfaces with the same Gaussian statistics of local slopes at each hierarchical level of roughness (Shkuratov et al., 2003a). Expression (18) corresponds to the limit when the number of hierarchical levels tends to infinity. Thus, the Akimov function seems to be as fundamental as the Lambert or Lommel–Seeliger laws. As noted by Akimov (1979a, 1988b), Eq. (18) describes the observed global brightness distributions over the lunar disk very well, though somewhat worse than the empirical Eq. (17). Another semi-empirical formula is based on the theoretical result (18) with a free parameter correcting the latitude trend:

$$D(\alpha, \beta, \gamma) = \cos \frac{\alpha}{2} \cos \left(\frac{\pi}{\pi - \alpha} \left(\gamma - \frac{\alpha}{2} \right) \right) \frac{(\cos \beta)^{\eta \alpha / (\pi - \alpha)}}{\cos \gamma}, \quad (19)$$

where η is a coefficient that is 0.34 for maria and 0.52 for highlands (Akimov et al., 1999, 2000). For simplicity we further use $\eta=1/2$.

Using Clementine images Kreslavsky et al. (2000) have shown that parameter v in (17) varies slightly over the lunar surface indicating that small spatial variations of the disk function occur. Meanwhile, the variations produce a chaotic pattern and look like noise. An exception was found for the Reiner- γ formation that displays systematically higher values of the parameter v . The prominent “limb darkening” for the Reiner- γ formation could imply a smoother surface on millimeter-decimeter scales than for typical regolith surface.

A quantitative comparison of the listed scattering laws (13)–(15), (19), and by Hapke (1993) is of great interest. Shown in Fig. 7a is a normalized equatorial profile of the ratio of apparent albedo images acquired by a telescope in red light at $\alpha=-16.2^\circ$ and $+16.2^\circ$ (Velikodsky et al., 2011; Korokhin et al., 2010). Such a ratio allows us to weaken the influence of albedo variations, making the global brightness trends more prominent. The images were corrected with disk functions by Hapke (1993), Hapke–Hillier (Hillier et al., 1999), Lommel–Seeliger (Eq. (13)), Minnaert (Eq. (14)), McEwen (Eq. (15)),

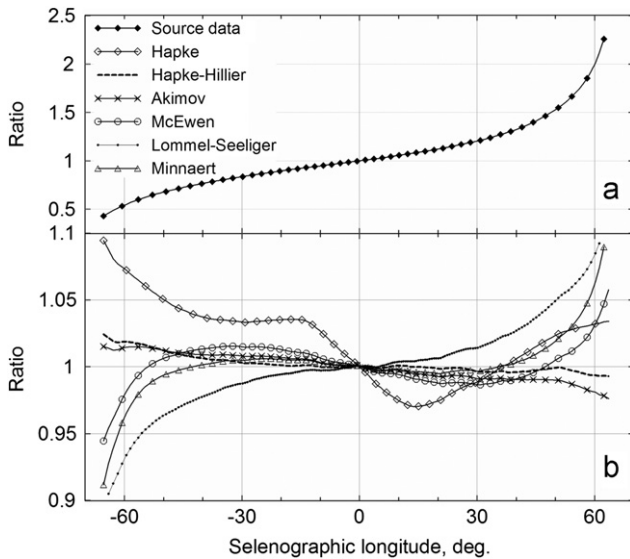


Fig. 7. (a) A measured equatorial profile of the ratio $A(-16.2^\circ)/A(16.2^\circ)$ and (b) equatorial profiles of the equigonal albedo ratio $A_{eq}(-16.2^\circ)/A_{eq}(16.2^\circ)$ calculated using different disk functions. All curves are normalized to their values at zero selenographic longitude. The Hapke (1993) parameters used for the correction are: $\omega=0.33$, $h=0.046$, $B_0=1.0$, and $\bar{\theta}=50.0^\circ$. For the Hillier et al. (1999) version of the Hapke model: $\omega=0.4$, $h=0.06$, $B_0=1$, $\bar{\theta}=25.5^\circ$, $f=0.45$, $g_1=-0.27$, and $g_2=0.65$.

and Akimov (Eq. (19)) to obtain equigonal albedo images; then, again the phase ratio was calculated. The equatorial trends of the ratio $A_{eq}(-16.2^\circ)/A_{eq}(16.2^\circ)$ are presented in Fig. 7b.

For calculations we used Hapke's (1993) model with a reduced number of the model parameters: ω is the single-scattering albedo, h and B_0 are the width and amplitude of the backscattering surge, and $\bar{\theta}$ is the angle of the characteristic slope of the lunar topography. It was used the single-scattering indicatrix $p(\alpha)=1+\cos \alpha$ and the values $\omega=0.33$, $h=0.046$, $B_0=1.0$, and $\bar{\theta}=50.0^\circ$ that were determined as the best-fitting of model phase curves to calibrated observational data obtained at the Maidanak Observatory (Uzbekistan) (Velikodsky et al., 2011; <http://astrodatal.univer.kharkov.ua/moon/albedo/>). These values were found for a circle area with the diameter of about 1/3 of the lunar disk size, which is located near the center of the disk (see inset in Fig. 22); we consider this area to be rather representative for the lunar nearside. We also used parameters for the Hillier et al. (1999) version of the Hapke model: $\omega=0.4$, $h=0.06$, $B_0=1$, $f=0.45$, $g_1=-0.27$, $g_2=0.65$, and $\bar{\theta}=25.5^\circ$, where the parameters f , g_1 , and g_2 characterize the single-scattering indicatrix. We used both the parameter sets attributing them to Hapke and Hapke–Hillier models.

As can be seen in Fig. 7b, the reduced model by Hapke produces 10% systematic trends to the limb and terminator. Akimov and Hapke–Hillier models describe the brightness longitude trend well, at least much better than the Lommel–Seeliger, Minnaert, and McEwen equations. It should be emphasized, however, that while the Akimov equation is amazingly simple and has no parameters, the Hapke equations are large enough and operates with at least four parameters. Fig. 8 shows normalized meridional profiles of the ratio $A(63.3^\circ)/A(2.7^\circ)$ of apparent albedo images described in Velikodsky et al. (2011); <http://astrodatal.univer.kharkov.ua/moon/albedo/> and that for equigonal albedo; i.e., the ratio $A_{eq}(63.3^\circ)/A_{eq}(2.7^\circ)$ calculated with the Lommel–Seeliger, Minnaert, Hapke, Hapke–Hillier, McEwen, and Akimov disk functions. The parameters as in Fig. 7b were used for the meridional profile calculations with Hapke's and Hapke–Hillier's models. Akimov's formula (19) provides the best compensation for the latitude brightness trend. The other disk functions are not able to describe both the longitudinal and latitudinal brightness trends of the lunar disk with high accuracy simultaneously. Fig. 8 reveals asymmetry relative to the photometric equator of the $A(63.3^\circ)$ image. This is because of the different orientations of the photometric equator of the apparent albedo images $A(63.3^\circ)$ and $A(2.7^\circ)$; in case of Fig. 8 we deal with a mixture of the latitude and

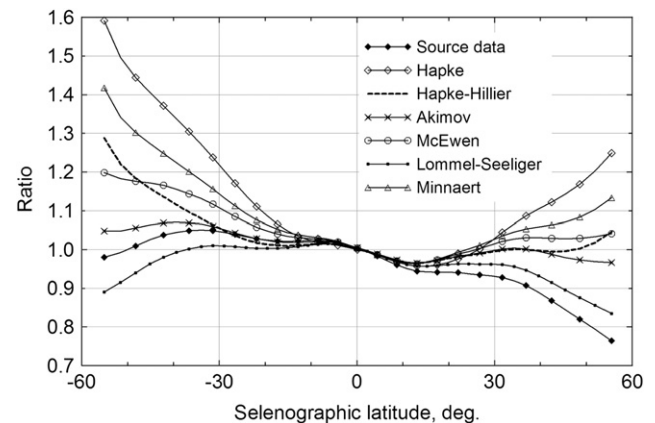


Fig. 8. A meridional profile of the ratio of apparent albedos $A(-63.3^\circ)/A(-2.7^\circ)$ and meridional profiles of the ratios of equigonal albedos $A_{eq}(-63.3^\circ)/A_{eq}(-2.7^\circ)$ calculated using different disk functions. All curves are normalized to their values at zero latitude. The same sets of the parameters as in Fig. 7 are used for the correction.

longitude trends. That is why the Lommel–Seeliger curve also is on the figure.

Thus, Figs. 7 and 8 unambiguously show that the Akimov function can provide a satisfactory description (compensation) of global brightness trends over the lunar surface. Simple formula (19) is known for long time (Akimov 1976), nevertheless, many workers continue to use the Lommel–Seeliger law or its analogs, though this effort might have been much better directed.

3.3. Phase function in a wide range of phase angles

The normalized phase function $f(\alpha)$ is a component of the photometric function $F(\alpha, \beta, \gamma) = f(\alpha)D(\alpha, \beta, \gamma)$ (Hapke, 1993). The phase function suggests information about the complexity of the structure of the light scattering surface. The Moon is far from being a Lambertian diffuser; a typical phase curve has the single sharp maximum at $\alpha=0$ (see Fig. 3).

There are integral and disk-resolved data on the lunar phase function. We note integral observations by Rougier (1933) ($\lambda_{\text{eff}}=440$ nm) and Lane and Irvine (1973) ($\lambda_{\text{eff}}=359.0, 361.5(U), 392.6, 415.5, 440.0(B), 457.3, 501.2, 548.0(V), 626.4, 729.7, 859.5$, and 1063.5 nm). Rougier's data were used to plot the curve in Fig. 3 that show the apparent albedo averaged over the illuminated portion of the lunar disk. There are several studies where the average lunar phase functions are constructed in wide phase-angle ranges using different observations. For example, such curves were built using Clementine UVVis data (Hillier et al., 1999; Kreslavsky et al., 2000), Smart-1 AMIE camera observations (Naranen et al., 2010), Kaguya (Yokota et al., 2009) and LRO WAC (Denevi et al., 2010) measurements.

Measured integral phase functions can be improved using *a posteriori* analysis. For instance, Korokhin et al. (2007) suggest a correcting procedure of the data by Lane and Irvine (1973), Rougier (1933). This procedure allows one to decrease regular errors of integral phase curves related to the libration variations; these errors are as high as 4%. A method of comparison of integral phase curves and photometric measurements of lunar samples or their structure analogs or small lunar sites was also proposed in Korokhin et al. (2007).

To approximate the phase curves of integral albedo in the range $6^\circ \leq \alpha \leq 120^\circ$, the following formula has been proposed:

$$A_{\text{eq}}(\alpha, \lambda) = A_{n1}(\lambda)e^{-\rho(\lambda)\alpha} + A_{n2}(\lambda)e^{-0.7\alpha}, \quad (20)$$

where $\rho(\lambda)$ is a coefficient that was called effective roughness (Korokhin et al., 2007) and $A_{n1}+A_{n2}$ is the normal albedo at $\alpha=0$. Table 2 shows the parameters of the function. The relation between A_{n1} and A_{n2} is almost constant along the spectrum (on average, $A_{n1}/A_{n2}=0.4 \pm 0.1$) and the parameter ρ increases considerably with λ . This means that the amplitude of the backscatter surge described by the first term in Eq. (20) is a constant, while the width of this peak decreases with increasing albedo (wavelength).

Lunar phase curves observed can be described with theoretical or empirical fitting curves. They are monotonic and, therefore, may be described with a small number of parameters. There is a variety of possibilities to develop this approach. In particular, one can use the empirical formula suggested by Akimov (1988b)

$$f(\alpha) = \frac{e^{-\mu_1\alpha} + me^{-\mu_2\alpha}}{1+m}, \quad (21)$$

which contains three parameters: μ_2 is the parameter associated with surface roughness, m and μ_1 are, respectively, a characteristic of the amplitude and the width of the opposition peak. Formula (21) can be obtained from a simplified theoretical consideration (Shkuratov, 1983). Recently, Velikodsky et al. (2011) suggested a more accurate expression for approximating

Table 2

The results of the approximation of the phase curves with formula (20).

λ , nm	A_{n1}	ρ	A_{n2}	σ
359.0	0.346	3.457	0.817	0.038
361.5(U)	0.358	3.169	0.800	0.041
392.6	0.299	3.974	0.864	0.037
415.5	0.354	3.821	0.821	0.032
440.0(B)	0.291	4.215	0.875	0.031
440.0(B) ^a	0.367	5.301	0.850	0.043
457.3	0.317	4.577	0.865	0.027
501.2	0.308	4.862	0.877	0.027
548.0(V)	0.264	6.036	0.925	0.028
626.4	0.543	9.104	0.851	0.038
729.7	0.379	8.277	0.905	0.036
859.5	0.291	9.263	0.957	0.030
1063.5	0.412	11.473	0.943	0.039

Note: σ is the relative root-mean-square error of the approximation; the measurements at 440.0(B).

^a Refer to the data by Rougier (1933).

the lunar phase function:

$$A_{\text{eq}}(\alpha) = A_1 e^{-\mu_1\alpha} + A_2 e^{-\mu_2\alpha} + A_3 e^{-\mu_3\alpha}, \quad (22)$$

where $A_1, A_2, A_3, \mu_1, \mu_2$, and μ_3 are coefficients of the approximation. At $\alpha=0$, $A_1+A_2+A_3=A_{\text{eq}}(0)=A_n$. The natural question arises: why do we use so many parameters to approximate so simple a monotonic phase-angle dependence obtained with measurements? There are two arguments that justify this approach. First, Eq. (22) used 6 parameters, but Kieffer and Stone (2005) applied approximation with 18 parameters. We note also that the Hillier et al. (1999) and modified Hapke (2002, 2008) models incorporates 8 fitting parameters; an empirical model by Buratti et al. (2011) uses 7 parameters. While formula (22) seems unnecessarily complicated, it is much simpler than other methods in use. Second, approximation (22) suggests not only a formal description of experimental data, but it could pretend to interpret them:

- The first term (A_1, μ_1), which has a maximal value of the exponent, approximately describes both the shadowing and non-shadowing opposition spike components. The first one may be caused by the effect of fractality (Shkuratov and Helfenstein, 2001), and the second one can be due to the coherent backscattering enhancement (Shkuratov, 1988; Hapke, 2002) and/or the lensing effect (Shkuratov, 1983; Trowbridge, 1984);
- The second term (A_2, μ_2) corresponds to the single particle scattering and shadow-hiding effect in the regolith medium. It also depends on albedo due to incoherent multiple scattering between regolith particles (Hapke, 1993);
- The third term (A_3, μ_3) describes the shadow-hiding effect on the lunar surface topography (Hapke, 1993) and the exponent has a minimal value.

Table 3 presents the selenographic coordinates of several lunar sites, for which the parameters of approximation (22) at $\lambda_{\text{eff}}=603$ nm were computed. Telescope observations described in Velikodsky et al. (2011); <http://astrodata.univer.kharkov.ua/moon/albedo/> were used.

Eq. (22) suggests a heuristic approach to describe observed lunar phase curves with high accuracy. More complicated equations by Hapke (1993, 2002) model allow almost the same accuracy. It is interesting to note that ray-tracing computer simulations for regolith-like media, which mimic light scattering in a real experiment (e.g., Stankevich and Shkuratov, 2000, 2002, 2004; Stankevich et al., 1999, 2000, 2003, 2007a,b), do not

Table 3

Selenographic coordinates of lunar sites and the parameters of approximation (22).

Sites	Latitude	Longitude	A_1	μ_1	A_2	μ_2	A_3	μ_3
M. Tranquillitatis 1	11°34'	39°10'	0.0275	64.0	0.0332	7.28	0.0676	0.772
M. Tranquillitatis 2	9°	29°	0.0297	62.9	0.0372	6.89	0.0691	0.696
M. Serenitatis	24°	23°	0.0311	50.1	0.0403	5.60	0.0706	0.603
M. Vaporum	14°50'	1°55'	0.0356	47.4	0.0418	5.27	0.0760	0.586
Sinus Medii	0°35'	-1°17'	0.0389	49.8	0.0430	5.37	0.0817	0.593
Gylden	-5°	0°	0.0627	49.7	0.0512	5.42	0.1278	0.580
Andel	-11°	12°	0.0657	44.7	0.0597	4.64	0.1331	0.542

improve cardinally the fit to lunar phase curves at realistic values of packing density.

3.4. Opposition effect

The brightness opposition effect manifests itself as a rapid increase of surface brightness when the phase angle approaches zero in a range of small phase angles. Compared to some atmosphereless celestial bodies, the Moon reveals a rather wide opposition surge. For instance, E-type asteroids have the point where the brightness sharply increases in the range 2–3° (Harris et al., 1989), for Kuiper belt objects this angle is even less (Belskaya et al., 2003); whereas, for the Moon it is near 7°. Usually one assumes a narrow spike to be due to the coherent backscattering, while a wide surge is a result of the shadow-hiding effect.

The coherent backscattering enhancement was discovered in laboratory measurements of bright MgO powders (Oetking, 1966). At the time this discovery was not appreciated; much later the significance of this new effect in planetology became clear (Kuga and Ishimaru, 1984; Shkuratov, 1985, 1988). The reason for the coherent backscatter spike is constructive interference of rays propagating in a particulate media along direct and time reversal trajectories (e.g., Shkuratov et al., 1999a). When $\alpha=0$, the lengths of the trajectories are the same and, therefore, the interference is always constructive. If $\alpha \neq 0$, an electromagnetic phase shift between the trajectory and its time-reversal occurs, which results in either constructive or destructive interference. Thus, at α close to zero the constructive interference is realized, and a backscattering spike should be observed, if single scattering albedo is high enough to produce multiple scattering.

To estimate the contributions of the shadowing and coherent enhancement effects to the backscattering peak at each phase angle is a difficult problem. In particular, Buratti et al. (1996) concluded that for the Moon at phase angles 0–5° the main cause of the lunar opposition surge is shadow-hiding effect; whereas, the coherent backscattering effect makes only a minor contribution. On the other hand, Hapke et al. (1993, 1998) have shown the contribution of coherent backscatter enhancement to be significant at small phase angles. Helfenstein et al. (1997) reached a similar conclusion analyzing telescopic lunar data, but Hillier et al. (1999) deduced that only for the brightest regions at 0.75–1.00 μm, a small coherent backscatter component of total amplitude ~1/6 to 1/4 that of the shadow-hiding surge is observed. There is an independent indication that the coherent component manifests itself in the NIR range where lunar albedo is higher (Kreslavsky et al. 2001). These contradictions make it possible to ponder over new (unknown) mechanisms of the opposition effect (Hapke et al., 2011).

During the Apollo missions, data on the opposition surge at smaller phase angles were obtained. It was found the brightness ratio $A(0)/A(8°)$ lie within the limits 1.3–1.4 (Pohn et al., 1969). No correlations with albedo or other surface characteristics were found.

Nozette et al. (1994) and Buratti et al. (1996) reported that Clementine discovered a narrow lunar opposition spike with amplitude 20% in the last 0.25°. However, such a spike cannot be observed in principle (Shkuratov et al., 1999a), because the Sun at 1 a.u. has an angular size of about 0.5°. Each point of the Sun's disk is an independent light source which has its own phase angle. This makes it impossible to observe any details of brightness phase curves with widths less than the angular radius of the Sun.

To retrieve phase functions near opposition using images with the spacecraft shadow point, different methods have been used. For instance, Buratti et al. (1996) suggested using a simple averaging over a number of images of different regions to diminish local albedo variations. However, if the averaging does not suppress the albedo patterns sufficiently, this may result in a noticeable influence on the final phase curve; in particular, the curve may reveal a dip or false narrow surge at $\alpha=0$; this is a probable reason for the "spike" found by Nozette et al. (1994) and Buratti et al. (1996).

Shkuratov et al. (1999a) have used another approach to retrieve the phase function from Clementine data. Due to spacecraft motion, the zero-phase-angle point moved on the surface between consecutive images. Thus, after mutual division of coregistered images taken in filters close to each other, the albedo pattern is almost eliminated, but the opposition spot is not quenched completely due to the shift of the spacecraft shadow point. Knowing the phase angle at each point of both images one may calculate the logarithmic derivative of the phase function at each point of the frame and, then, average the derivative over all points with the same α . Integration of the derivative produces a phase curve. Averaging and integrating procedures effectively suppress experimental noise and, therefore, obtained phase curves are sufficiently smooth. Fig. 9 shows near-opposition phase functions derived by the differential method for two sites with different albedo (Shkuratov et al., 1999a). These are compared with phase functions for "average" highland and mare regions by Buratti et al. (1996) that are also presented in Fig. 9. The differential method shows the opposition effect of the Moon at the phase angle 0.2–1.6° to be rather inert with flattening at small phase angles <0.25°. This flattening is due to the angular dimension of the Sun's disk. The Buratti et al. (1996) data show dissimilar behavior.

Although the Moon cannot be observed from the Earth at $\alpha < 1°$ out of eclipse, ground-based telescope observations still remain interesting to study the opposition effect. Velikodsky et al. (2011) have produced a series of lunar images near opposition (excluding the eclipse phase). The images were taken with a telescope at $\lambda_{eff}=603$ nm. During their acquisition the direction of the photometric equator continuously changed by 180°, and the direction of the phase angle trend over the lunar disk was also rotated. Thus, one may separate the phase trend from the albedo pattern and use it to study the phase function, if a corresponding phase ratio image is prepared. In particular, the global brightness trend seen on the phase ratio $A(1.6°)/A(2.7°)$ image (Fig. 10) has

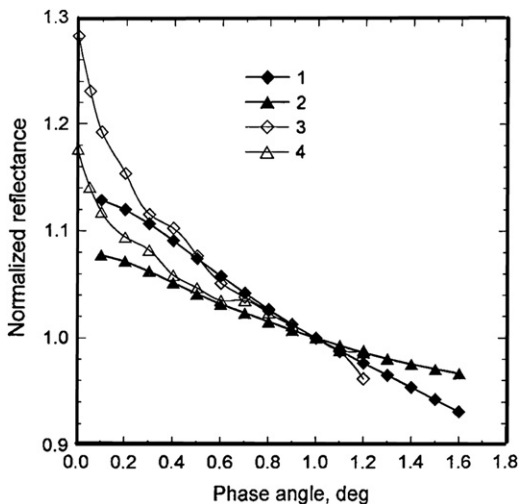


Fig. 9. Near-opposition phase functions found using the differential method for the sites 1.3°N, 3.9°E, Sinus Medii (curve 1), and 1.4°N, 48.7°E, Mare Fecunditatis (curve 2). The phase functions for averaged highland and mare regions (Buratti et al., 1996) are presented by curves 3 and 4, respectively.

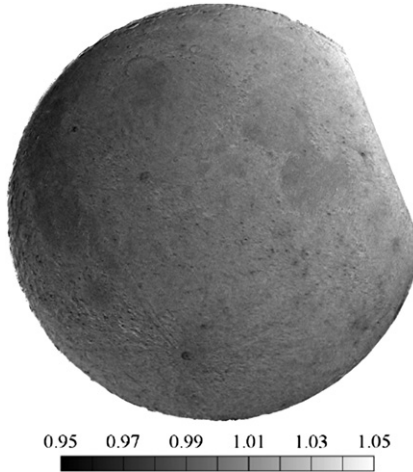


Fig. 10. Phase ratio 1.6°/2.7° of equigonal albedo in relative units ($\lambda_{\text{eff}}=603$ nm); central phase angles are indicated. The global brightness trend relates to the phase-angle variation over the lunar disk.

been used for the determination of $A_{eq}(\alpha)$ (Velikodsky et al., 2011); the phase angles 1.6° and 2.7° correspond to the center of the lunar disk. This method provides much more accurate results than ordinary measurements. Fig. 11 illustrates this, depicting $A_{eq}(\alpha)$ found with phase-ratio imaging (crosses) and usual photometry (Velikodsky et al., 2011).

Using phase-ratio imagery $A(1.6^\circ)/A(2.7^\circ)$, one may also estimated how much the phase function depends on the type of the lunar surface at so small phase angles. Fig. 10 shows the phase ratio to be almost the same for mare and highland regions; the difference is approximately 1%. More detailed study is impeded by the noise related to the surface relief and atmospheric distortions; i.e., in general, the lunar surface has almost equal slopes of phase curves at phase angles 1.5–3°. Exceptions are bright rayed craters (e.g., Tycho, Copernicus, and Aristarchus) clearly visible as dark spots; these areas have smaller phase-function slopes. Both mare and highland young craters have phase ratios approximately 5% lower than their neighboring regions. This is an unexpected result, as the craters are rather bright and we could anticipate a manifestation of the coherent backscattering enhancement resulting in the opposition spike increasing at so

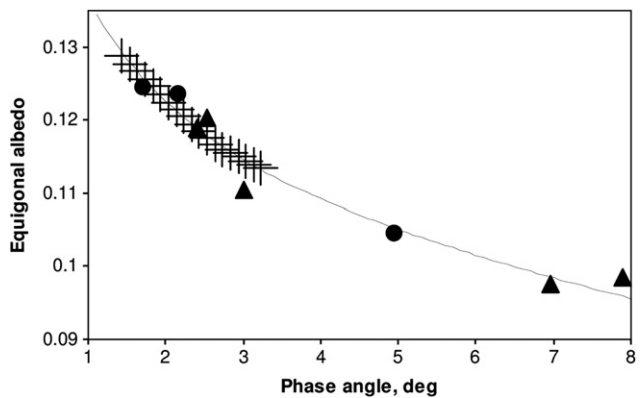


Fig. 11. Phase dependence of equigonal albedo of an area in Sinus Medii (selenographic latitude 0°35', longitude -1°17'). Observations are divided into groups: the observations after moonrise and before moonset (triangles) and night time observations near culmination (dots). Phase dependence determined with the image shown in Fig. 10 is presented by crosses; this trend was normalized with our absolute observations (Velikodsky et al., 2011).

small α . Thus, either the albedo is not high enough to provide the coherent spike or it is too narrow to be revealed in the phase-angle range of 1.6–2.7°. The first seems to be more probable, since our laboratory measurements of different powders with albedo less than 40% do not show brightness spikes at the phase angle range 0.008–1.5° (Psarev et al., 2007). This conclusion contradicts to the experiments by Hapke et al. (1993, 1998) with circular polarization ratio of lunar samples. However, the Hapke experiments may have an alternative treatment. For example, the same increase of the ratio can be found in DDA calculations of single scattering by differently shaped particles the size of which is compared to the wavelength (Zubko et al., 2008; Mishchenko et al., 2009a,b). This result is entirely confirmed with our computations for small particles with the so-called Sh-matrix method (e.g., Petrov et al., 2007, 2011). Since the particle size is small, the increase of the ratio cannot be treated as a manifestation of the coherent enhancement of multiple scattering in a single particle.

3.5. Phase ratio imagery

Mapping features in the phase functions can be a very effective tool to study lunar surface structure. The simplest approach is mapping the phase ratio $f(\alpha_1)/f(\alpha_2)$. Such imagery allows one to estimate variations of the complexity of unresolved surface roughness and microtopography.

Wildey (1978) produced an image of the phase ratio $A(2.0^\circ)/A(4.5^\circ)$ by averaging 25 telescope images. This image has a very low resolution, because of its uncompensated libration effect. Akimov and Shkuratov (1981) used the method of photographic subtraction of images with equal contrast, obtained at two different α , but similar parameters of lunar libration; it was found that bright craters (e.g., Tycho, Copernicus) exhibit small phase ratios $f(3.2^\circ)/f(14.5^\circ)$ at $\lambda=630$ nm; this is similar to the behavior of young craters shown in Fig. 10. Later distributions of several phase ratios of the lunar nearside were obtained using computer transformation of images to the same libration and scale (Shkuratov et al., 1994a; Korokhin and Akimov, 1997; Kaydash et al., 2009a). Then, this technique was extended to data acquired with space crafts (Kreslavsky et al., 2000; Kreslavsky and Shkuratov, 2003; Kaydash et al., 2009b, 2011).

Using phase-ratio imagery that exploited the ground-based telescope, new lunar surface formations (photometric anomalies) were recently found in the southern portion of Oceanus Procellarum (Shkuratov et al., 2010). These formations hypothetically

are weak swirls. Thus, the Moon is still an interesting object for telescopic researches. To some astronomers this seems annoyingly trivial, but to others it is defiantly controversial. One may encounter the question: Why do astronomers observe the Moon from the Earth, if men have already been there? The answer for skeptics distributing telescope time at observatories is rather obvious: Investigations *in situ* and with satellites sharply increase the number of unresolved problems related to the Moon, a large portion of which can be resolved with ground-based observations.

Fig. 12a shows an image of the southern portion of Oceanus Procellarum obtained with the almost amateur 50-cm telescopes of the Maidanak observatory (Uzbekistan) equipped with a Canon CMOS camera at $\lambda=0.53\text{ }\mu\text{m}$ and $\alpha=23^\circ$ (Velikodsky et al., 2011). The crater Euclides and Montes Riphaeus are seen near the center of the scene. Three outlined and numbered areas show the photometric anomalies. The largest one (numbered with 3 in **Fig. 12a**) is $\sim 70\text{ km}$ in size. The phase-ratio images $f(44^\circ)/f(96^\circ)$ are shown in **Fig. 12b**. The values of the phase-ratio parameter are normalized to the mean value over the image (see scale bar). The phase-function slope for the anomalous areas is $\sim 2\text{--}3\%$ higher than for the surrounding dark mare regions. The anomalies are also observed for other phase ratios (Shkuratov et al., 2010).

Fig. 12a,b demonstrate the inverse correlation between albedo and the phase ratio. Bright ejecta halos of young mare craters appear as features with a relatively lower phase curve slope. The inverse correlation can be easily explained. The brighter the surface, the higher the illumination of shadows caused by

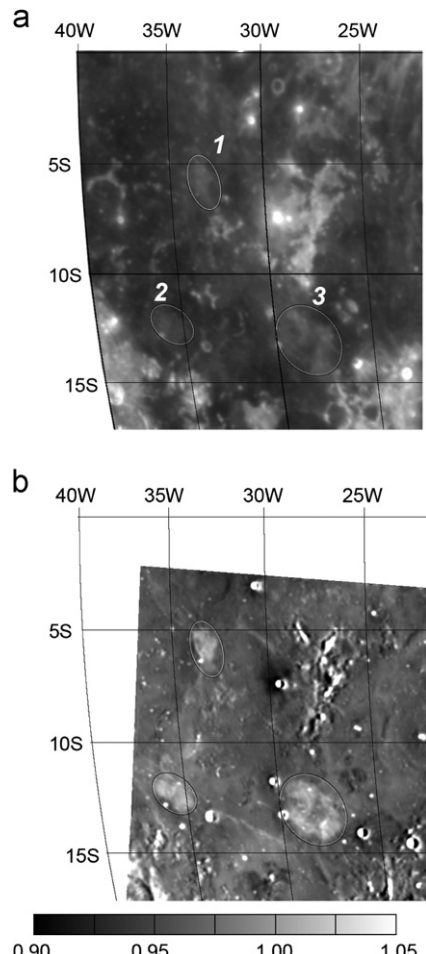


Fig. 12. (a) Brightness image of the southern portion of the Oceanus Procellarum; (b) phase-ratio image $f(44^\circ)/f(96^\circ)$ at $\lambda=0.53\text{ }\mu\text{m}$. Outlined and numbered areas are the photometric anomalies.

multiple light scattering. This secondary illumination decreases the slope of the phase curves. The fact that relatively dim details numbered in **Fig. 12** result in higher phase curve slopes means that the surface roughness is large enough not only to compensate for the albedo effect, but to produce the positive phase-ratio anomalies. Images acquired with *Lunar Orbiter IV* and *Apollo-16* cameras and *LRO NAC* data with much higher resolution reveal no anomalous mesoscale topography of the details. These areas do not have any thermal inertia, radar (70 and 3.8 cm), magnetic, or chemical/mineral peculiarities. However, they exhibit a polarimetric distinction that may relate to the presence of a porous regolith upper layer consisting of dust particles (Shkuratov et al., 2010). The anomalies can be regions of very fresh shallow regolith disturbances caused by impacts of meteoroid swarms consisting of rather small impactors. The scale of the disturbances (roughness) can be mm–cm, which may remotely be detected with the phase-ratio technique. This origin of the disturbances is similar to one of the hypotheses for the origin of lunar swirls like the Reiner- γ formation (Pinet et al., 2000; Starukhina and Shkuratov, 2004). The photometric difference between the shallow and pervasive (Reiner- γ class) swirls is that the latter appear to have a significant amount of immature soils in the upper surface layers. On the other hand, the origin of these classes of swirls can be different. Garrick-Bethell et al. (2011) have considered that swirl's spectral properties are plausibly explained by fine-grained dust sorting, which may result from the vertical electrostatic lofting of charged fine dust related to the formation of electrostatic potential anomalies formed at magnetic anomalies (like Reiner- γ formation) as solar wind protons penetrate more deeply into the magnetic field than electrons. The electrostatic potential anomaly can attract or repel charged dust. The finest fraction can be accumulated in some areas. The dust is bright and considerably contributes to albedo of the lunar surface. Rather intensive dust moving leads to surface smoothing in the areas and should produce negative photometric anomalies (unusually low slopes of phase curves).

The phase ratio technique also has been applied to an analysis of photometric data acquired with *Clementine* and *Smart-1* (Shkuratov et al., 1999a; Kreslavsky and Shkuratov, 2003; Kaydash et al., 2009b). However, the most impressive results recently have been obtained using *LRO NAC* data (Kaydash et al., 2011). The intensity of lunar resurfacing processes depends strongly on the scale of consideration. Obviously, the processes are more appreciable in small scales. Owing to the high resolution of the *LRO* cameras, interesting investigations of the surface processes are possible. We here studied structure anomalies using *LRO NAC* images of the *Apollo-14* landing site and a region on the wall of the crater Kepler.

The frames M114064206LC and M114071006LC including the *Apollo-14* landing site have almost the same resolution and the angles i and φ . The sameness of the angles allows one to avoid the influence of resolved topography. A fragment of the lower-phase-angle frame M114064206LC ($\alpha=41.16^\circ$) is presented in **Fig. 13a**. The image, taken at 0.53 m/pix resolution, reveals the landing spot of the lunar module *Antares* in the upper-left corner of the scene. The inset presents the landing spot in full resolution with the descent module indicated by white arrow and tracks of a modular equipment transporter indicated by short white arrows. The Apollo Lunar Surface Experiments Package (ALSEP) installation about 180 m from *Antares* is surrounded by multiple transporter tracks that show up as low-brightness features especially in the descent module vicinity. The phase ratio image $f(41^\circ)/f(79^\circ)$ is presented in **Fig. 13b**. This image was computed with a rubber-sheet geometric transformation accounting for the parallax effect (Kaydash et al., 2011). The landing site is shown with a full resolution image in the inset markedly stands out as dark spot

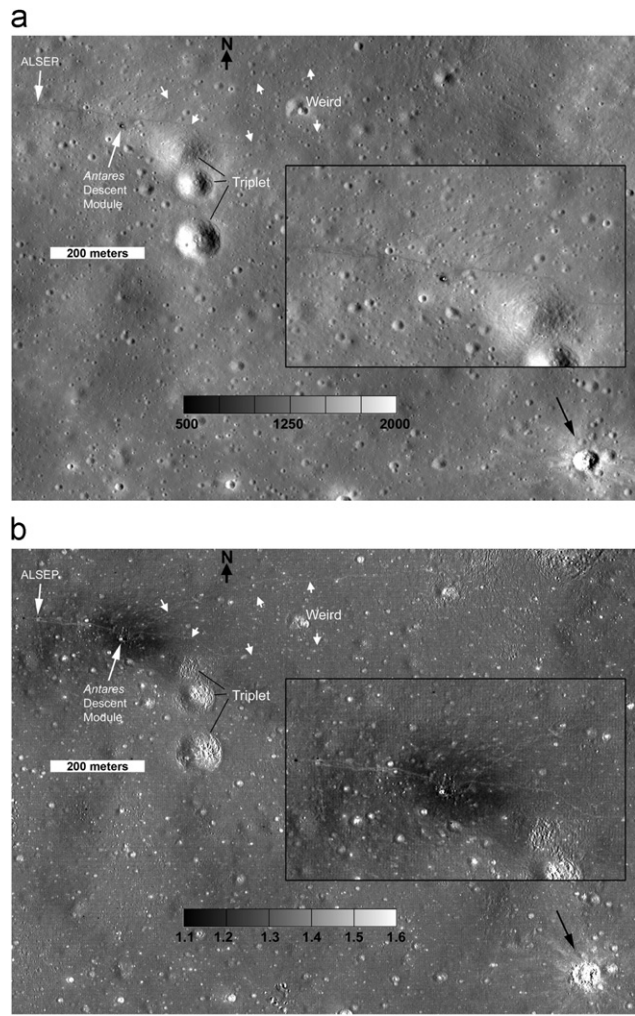


Fig. 13. The Apollo-14 landing site imaged by LRO NAC: (a) a fragment of calibrated LROC image M114064206LC at 0.525 m/pix spatial resolution and (b) a phase-ratio image $f(41^\circ)/f(79^\circ)$ of the same area. The proper dynamic range bar is shown in the bottom part of the figure. To convert pixel numbers to radiance factor I/F units $\mu\text{W}/(\text{cm}^2 \text{sr nm})$, one should multiply pixel counts to the scaling coefficient 3.05×10^{-5} .

against the gray-colored background. Thus, the landing area is an obvious photometric anomaly. The dark spot corresponds to anomalously smaller phase curve slope, which indicates smaller roughness in this area (Fig. 13b). The transporter tracks are seen as bright details in the Antares vicinity, i.e., as features with higher ratio $f(41^\circ)/f(79^\circ)$.

Two main effects have influenced the lunar regolith at the site: blowing of the soil by the gas jets from engines of the landers and disturbances by the soles of the lunar boots of walking astronauts and by the wheels of the modular equipment transporter. Blowing of the soil by the plume of the descent stage destroys the porous (“fairy castle”) structure of the uppermost regolith layers and sweeps away mainly the fine soil particles (Immer et al., 2011) which then fall down making the surface smoother (Kreslavsky and Shkuratov, 2003). The gas pumping into the regolith that is a powder may induce its pseudo-fluidization, which leads to surface smoothing and compacting. As a result, the brightness of such a destroyed area somewhat increases due to a weakening of the shadow-hiding effect and the presence of small particles; this also leads to a decreasing phase-function slope (negative anomaly). Owing to strong adhesion, the lunar soils behave mechanically as wet sand. When astronauts walk on the lunar surface, moving the modular equipment transporter, they

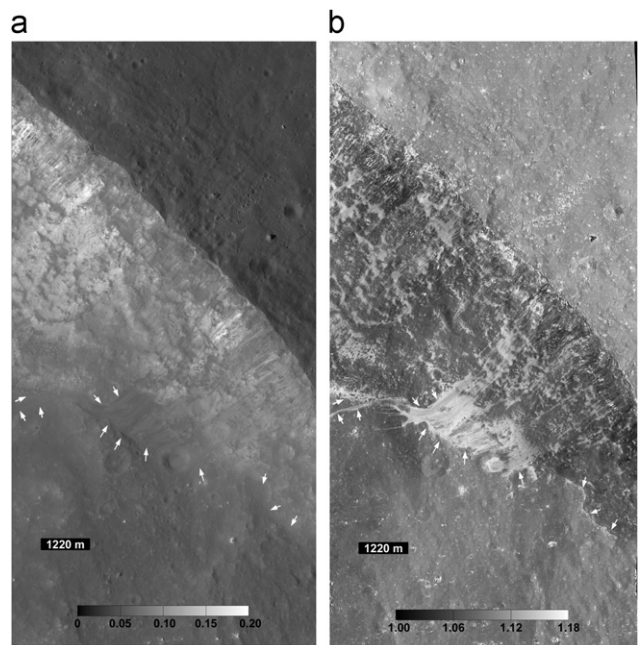


Fig. 14. (a) A fragment of the LROC image M104762819L presenting part of the eastern rim and floor of the crater Kepler. The scale bar shows a range of the image in radiance factor units at $\alpha=52^\circ$ and (b) a distribution of the phase ratio $f(52^\circ)/f(67^\circ)$ for the region is shown in (a).

disturb the surface, making it more cloudy and rough. The disturbed area produces more shadows that produce positive photometric anomalies, i.e., higher $f(41^\circ)/f(79^\circ)$. The biggest crater in the scene reveals itself as a positive anomaly; it is seen in the lower-right corner of Fig. 13b. Boulders, blocks, and rock fragments within the proximal ejecta of the crater may here produce the roughness anomaly.

The described technique reveals the same kind of structure anomalies in landing sites of the other *Apollo* missions (Kaydash et al., 2011).

Using the phase ratio technique we detected significant variations of surface roughness inside some of the large craters. Fig. 14a shows a fragment of the image M104762819L presenting the eastern portion of the rim and floor of the crater Kepler ($\alpha=52^\circ$). A distribution of phase ratio $f(52^\circ)/f(67^\circ)$ for this portion was calculated and presented in Fig. 14b. The phase ratio image is very impressive, as it suggests many new details; some of them are hardly seen in the albedo image. Overall, an inverse correlation between the phase ratio and surface albedo is observed, but significant deviations from this rule are seen, indicating anomalies in the lunar regolith structure. White arrows show debris streams (white color) on the crater slope and the border of the floor of the crater that are hardly seen on the albedo image. The dark areas in Fig. 14b are probably the result of regolith accumulations producing an even surface. Thus, the phase ratio approach is very useful to study resurfacing processes on the Moon, such as soil creeps, debris/rock streams, taluses, etc.

3.6. Phase dependence of color ratio

The dependence of color ratio of the lunar surface on phase angle α is poorly studied. It is believed that the color index, defined by the ratio $C(0.6/0.4 \mu\text{m}) = A(0.6 \mu\text{m})/A(0.4 \mu\text{m})$ increases monotonically with increasing α in the range $0-90^\circ$ by about 10–15% (McCord et al., 1969; Mikhail, 1970). Using data by Lane and Irvine (1973) and Korochkin et al. (2007) have shown that the phase dependence of the color ratio of the Moon has a

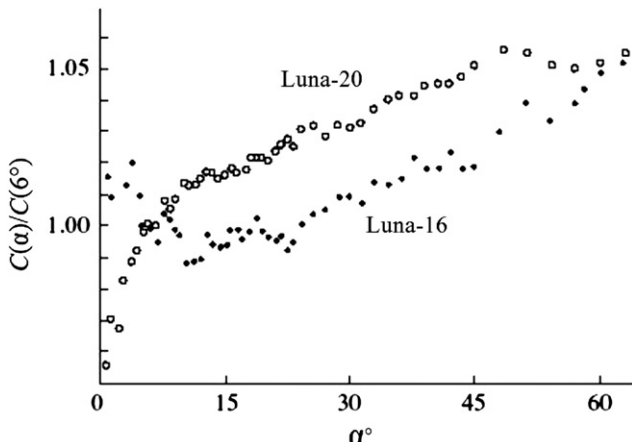


Fig. 15. Phase-angle curves of color ratio $C=A(0.6 \mu\text{m})/A(0.4 \mu\text{m})$ for lunar samples delivered by the space probes *Luna-20* and *Luna-24*.

maximum at α near 50° and, probably, a minimum near 10° ; the latter, however, is not determined reliably. Laboratory measurements of the lunar regolith, which are more accurate than telescope observations, showed that, in some cases, the minimum in the $C(\alpha)$ curve can be observed at phase angles of about $10\text{--}15^\circ$ (O'Leary and Briggs, 1973; Akimov et al., 1979b; Shkuratov et al., 1996). Hapke et al. (1998) have found this minimum for eight lunar samples at $\alpha \approx 4^\circ$. The increase of $C(\alpha)$ at small α is named sometimes a colorimetric opposition effect. Fig. 15 shows phase curves of color ratio for two lunar samples delivered by the Soviet probes *Luna-16* and *Luna-20*. The behavior of the samples is quite different. The *Luna-16* sample demonstrates the colorimetric opposition effect. Similar behavior can be seen in other lunar samples (O'Leary and Briggs, 1973; Akimov et al., 1979b; Shkuratov et al., 1996) and other materials (Shkuratov et al., 1996, 1999a).

Data processing the lunar surface survey performed by the *Clementine* spacecraft showed the monotonic increase of the function $C(\alpha)$ with decreasing α in the region of small phase angles (Buratti et al., 1996; Shkuratov et al., 1999a). The same has been shown recently with *Kaguya* (Yokota et al., 2009) and *LRO WAC* (Denevi et al., 2010) measurements. This contradiction between the laboratory and lunar measurements requires further consideration.

If the colorimetric opposition effect exists, this could be a manifestation of the coherent backscatter effect that predicts a more prominent opposition peak of the lunar regolith in red light where the regolith is brighter. If so, we could expect the opposition color ratio surge for the brighter (*Luna-20*) sample, but Fig. 15 reveals the opposite result. This serious contradiction may imply that this effect is not due to the coherent backscattering.

Kaydash et al. (2010) mapped phase ratios of the color ratio $C(600/470 \text{ nm})$ for the lunar nearside using the data of Earth-based colorimetry in the phase angle range $2\text{--}95^\circ$. It was found that for highland regions this color ratio increases with α faster than that for mare areas up to phase angles of $\sim 40^\circ\text{--}50^\circ$. At $\alpha > 50^\circ$ the opposite behavior is observed. Fig. 16a presents the images of the eastern part of the lunar disk; the *Apollo-11* landing site is marked by a star. Fig. 16b shows the color ratio $C(600/470 \text{ nm})$ distribution obtained as a quotient of the red and blue images at a phase angle of 21° . This image is normalized to the value measured in a small area of Mare Serenitatis; this area marked with a cross in Fig. 16b coincides with the spectrophotometric standard MS-2 (Pieters, 1978). The brighter tone in the color-ratio distribution corresponds to the redder regions of the lunar surface. The distribution of $C(6^\circ)/C(21^\circ)$ is presented in

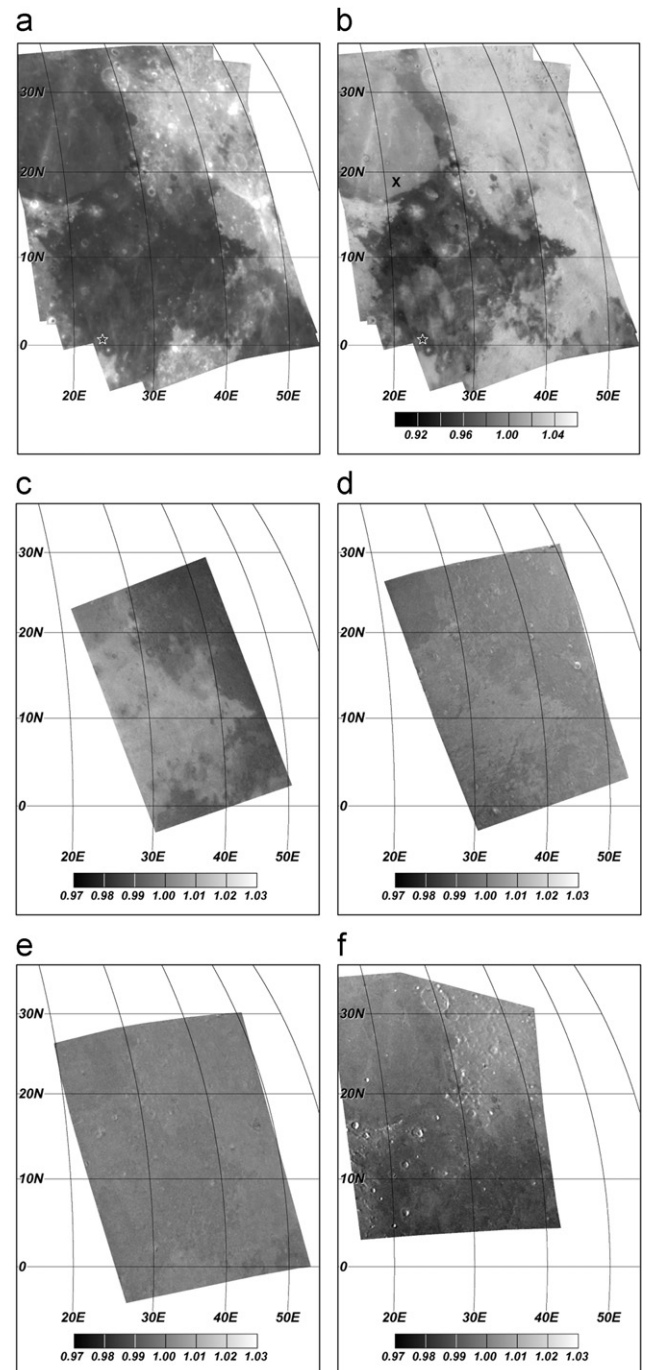


Fig. 16. Mapping of the phase ratios of the color-ratio mosaics $C(600/470 \text{ nm})$ for the eastern part of the lunar nearside. The *Apollo-11* landing site and the location of the maps normalization are shown, respectively, with the asterisk and cross: (a) albedo distribution at $\lambda=470 \text{ nm}$; (b) color ratio $C(600/470 \text{ nm})$ image; and (c)-(f) phase ratios $C(6^\circ)/C(21^\circ)$, $C(21^\circ)/C(48^\circ)$, $C(48^\circ)/C(62^\circ)$, and $C(75^\circ)/C(94^\circ)$, respectively.

Fig. 16c. This demonstrates higher values of the mentioned ratios for mare regions relative to those for the highlands by 3–4%; differences of 1–2% are also seen between $C(6^\circ)/C(21^\circ)$ values for Mare Serenitatis and Mare Tranquillitatis. In general, the presented distributions are inversely correlated with the albedo distribution. At larger phase angles, phase ratios of the color ratio have less contrast: see the $C(21^\circ)/C(48^\circ)$ and $C(48^\circ)/C(62^\circ)$ distributions in Fig. 16d,e; the contrast becomes inverted in $C(75^\circ)/C(94^\circ)$ shown in Fig. 16f. This inversion is not yet explained.

3.7. Photogrammetry

Brightness variations in images of the lunar surface at arbitrary phase angles depend generally on the spatial distributions of albedo, global illumination/observation geometry, and local topographic slopes (height gradients) that change the local incident i and emergent e angles. There are techniques allowing retrieval of the topography and albedo distributions directly from the photometric images. These are photogrammetry (stereo) and photoclinometry (shape-from-shading) methods or their combination.

The first method is based on the use of mutual parallaxes of surface details observed at two different viewing angles. This method has been widely used to retrieve the topographic information on planets from images obtained with space missions (e.g., Cook and Robinson, 2000; Herrick and Sharpton, 2000; Oberst et al., 2010). There have been attempts to recover the albedo distribution on a surface from images using the photometric stereo approach (e.g., Chen et al., 2002). We suggest below a specific example illustrating this approach in more detail.

Opanasenko et al. (2007) carried out a photogrammetric examination of the *Clementine* and *HST* images of the Apollo-17 landing area. Corresponding *Clementine* UVVis data (Nozette et al., 1994) and *HST* ACS/HRC images (Garvin et al., 2006) have almost the same resolution (about 100 m), rather close phase angles (approximately 30° and 39°), and effective wavelengths (700 and 680 nm); whereas, the viewing angles are different (nadir-looking and 25°), respectively. These images were reprojected into the simple cylindrical projection; then seamless mosaics of *Clementine* and *HST* images were made (Opanasenko et al., 2007). Examples of these source mosaics for the Apollo-17 landing site are shown in Fig. 17a,b. An automatic procedure to find the parallaxes was used: first, a hard co-registering of *Clementine* and *HST* mosaics fragments was made; the images also were brought to the same spatial resolution; then, the mutual shifts of the same lunar surface details were determined by finding the maximum of the cross-correlation function of small portions of both images in a circular running window; this algorithm is also known as a rubber-sheet geometric transformation (see Section 3.5).

The accuracy of *Clementine* and *HST* pointing is too low to obtain absolute elevation with respect to the lunar center of mass. To reach reasonable (tens of meters) vertical precision, the parallax shifts should be measured with subpixel accuracy, which demands appreciable size of the window for matching. On the other hand, the use of a large window decreases the spatial resolution of the elevation model. The balance of the vertical precision and spatial resolution dictates the choice of the running window size. In practice, however, another factor limits the window size: Some parts of the scenes are rather featureless. Because of this, maximizing correlation in a small window may give a false result due to matching the noise patterns rather than surface features. Such false parallax shifts can be easily filtered out, even, if their proportion is rather high; however, this would lead to non-uniform spatial resolution. Opanasenko et al. (2007) chose a window radius of 10 pixels, which gives a reasonable proportion of false matches and a step between neighboring windows of 5 pixels. They applied a heuristic algorithm to identify false matches, remove them, and fix the gaps in the elevation model. Fig. 17c presents the elevation map. Highland massifs rise about 2 km above the valley floor. Comparison of the map with the USGS 1:50000 one digitized in Robinson and Jolliff (2002) shows very good agreement (Opanasenko et al., 2007). Fig. 18 shows simulated oblique views of the shaded topography (the Lambertian scattering indicatrix was used to generate this image) and the same view draped with the brightness image. The viewing rays pass from the right bottom corner of the scene shown in Fig. 17. Note that new LROC data are very suitable to

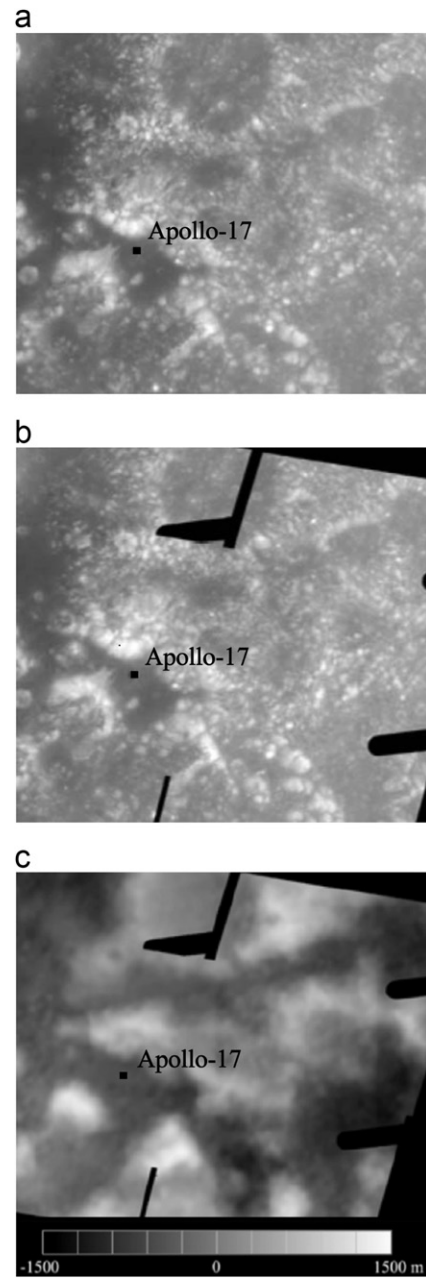


Fig. 17. (a) Clementine ($\lambda=750$ nm, $\alpha \approx 30^\circ$), (b) HST ($\lambda=658$ nm, $\alpha \approx 39^\circ$) mosaics of the region of the Apollo-17 landing site, and (c) a map of elevations; brighter shades denote higher elevations.

produce topographic maps of high resolution using photogrammetry method (Robinson et al., 2010).

3.8. Photoclinometry

Surface facets with orientations more nearly perpendicular to the illumination direction are brighter than those facets facing away. The photoclinometry technique exploits this fact. The simplest approach, using a single image, allows one to assemble a topographic profile by integrating slopes along a line parallel to the illumination direction, ignoring albedo variations. If there are many images of the same scenes at a fixed angle of view and different α , one may find albedo, topography, and the phase function for each point of the surface under study.

Recovering topography of the Moon with the photoclinometry method has been proposed by van Diggelen (1951). Later a series

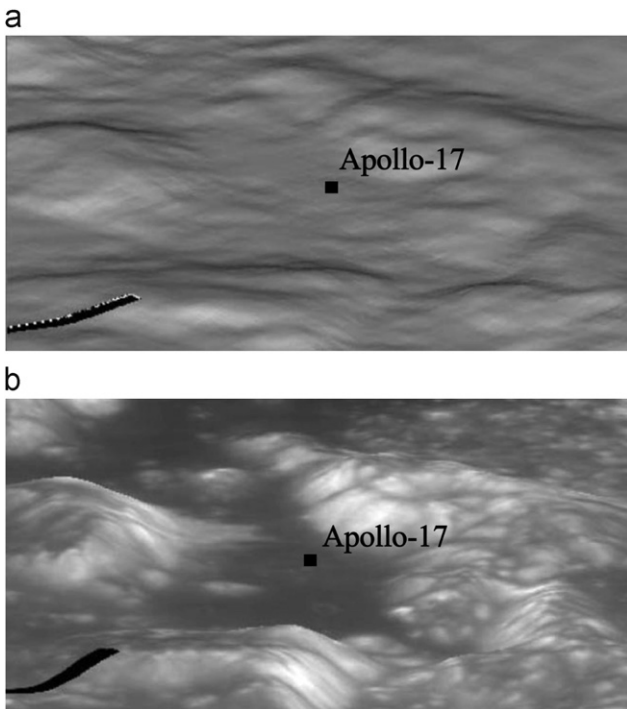


Fig. 18. (a) A perspective view of Taurus–Littrow valley (simulated shaded topography) and (b) a simulated perspective view of the Taurus–Littrow valley draped by the brightness image.

of many studies devoted to lunar and planetary surface photoclinometry using Earth-based and space mission observations was carried out (e.g., Korokhin et al., 2010 and references therein). Korokhin et al. (2010) also present results of a new photoclinometry technique that includes analysis of many absolutely calibrated images of the same scenes acquired at different phase angles. The authors demonstrate the capability of the method using high-quality absolute photometry imagery of the Moon (Velikodsky et al., 2011). This method is valid for any slopes when projection shadows are absent.

The local slopes of the surface affect the local illumination/observation geometry, i.e., the photometric coordinates γ and β . The relations between the disturbed photometric coordinates and the slope components (s_l, s_b), where l and b are, respectively, the selenographic longitude and latitude, can be found in Korokhin et al. (2010). The gist of the approach to retrieve information about the relief, albedo, and the parameters of phase-function slope from photometric images is to use a rather large set of calibrated images obtained for the same scene at different phase angles. Then, for each point of the lunar surface a phase curve of the equigonal albedo can be plotted. One may numerically minimize the standard deviation of the observed $A_{eq}(\alpha)$ from a model phase function varying simultaneously the values s_l, s_b, A_0 , and the parameters of the function (see, e.g., Eq. (21)). This automatically provides minimization of brightness variations caused by topographic slopes, allowing, thereby, the determination of the slopes (Korokhin et al., 2010).

To illustrate the algorithm we use Earth-based telescope observations of the Moon at $\lambda=603$ nm and phase angles when the solar rays come almost along lines of selenographic latitude (Velikodsky et al., 2011). Twelve maps of absolute equigonal albedo at phase angles varying from 12° to 22° were used. To obtain the maps from calibrated apparent albedo images, we applied Eqs. (19) and (21). The resolution element of the maps is approximately $3.2 \times 3.2 \text{ km}^2$ in the lunar disk center. This is the minimal base of roughness we deal with. Fig. 19a presents a map

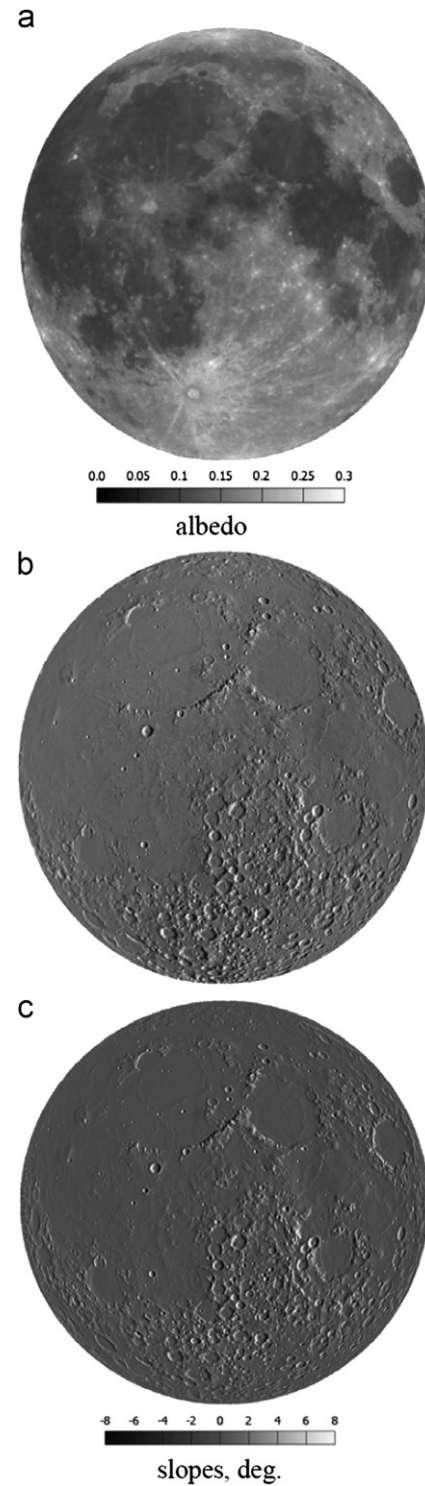


Fig. 19. (a) A map of A_n calculated in the range of phase angles 12 – 22° ; (b) a map of longitudinal topographic slopes determined on a 3.2 km base, which is calculated using the same images; and (c) a map of longitudinal topographic slopes determined on the 3.2 km base, retrieved from the LALT data.

of A_n , i.e., albedo distribution that is not influenced by topography (Korokhin et al., 2010). This map characterizes reflecting properties of the lunar surface materials; however, it does not present the real brightness distribution at $\alpha=0$, as it ignores the opposition effect that is beyond the phase angle range 12 – 22° . Fig. 19b shows a distribution of the longitudinal component s_l of topographic slope calculated on the 3.2 km base (Korokhin et al.,

2010). This map coincides well with previous results (Korokhin and Akimov, 1997).

Recent altimetric data have been obtained with the LALT (Laser Altimeter) aboard the spacecraft Kaguya (Araki et al., 2009). Korokhin et al. (2010) used the global LALT topography for comparison with photoclinometric data. The LALT data were brought to the conditions when the comparison was feasible (see Fig. 19c). Both the maps show a very similar distribution of the longitudinal slopes over the lunar disk. However, more detailed analysis also reveals differences. For instance, the photoclinometric map demonstrates a weak residual influence from albedo (see, e.g., the Copernicus ray system). The LALT map exhibits many small topographic artifacts.

Korokhin et al. (2010) also have demonstrated the use of topographically corrected phase-ratio images. This allows one to study phase dependence of the lunar surface brightness not only for flat mare regions, but for highlands and other areas with resolved topography, e.g., relatively small swirls in the region of the central nearside highlands (Blewett et al., 2007) are seen better on phase-ratio images, when the topographic effect is removed.

3.9. Interpreting photometry

To retrieve quantitative information on the lunar surface structure and composition from photometric measurements of the Moon, a theoretical model of light scattering by regolith-like surfaces should be applied. Such models generally are insufficient because of the great complexity of planetary surfaces. The lunar surface has multiscale structure, and each scale requires several parameters for its description. Moreover, the optical parameters of the particle material also have to be taken into account. These parameters, the real and imaginary parts of the complex refractive index, depend on the composition and can vary significantly, not only over a wide region, but even locally in a microscopic scale. Thus, an adequate theory inevitably has to operate with many physical parameters. Meanwhile, as has been seen, the lunar phase curves are very simple and similar to each other. Therefore, there is a problem of uniqueness of fitting, when many parameters are used. Any rigorous theory may become useless if it cannot fit reliably and unambiguously to experimental data. If a simplified theory operating with a small number of parameters is used, then the fitting can be satisfactory, but such a theory may be considered as inadequate (oversimplified) and can be a target for criticism. This is why many workers prefer to use simple empirical formulas with a small number of parameters, even if the parameters have no physical sense or this sense is very conditional; at least the formulas are able to provide fitting uniqueness.

Among different models, the most developed and popular one was suggested by Hapke (1971, 1993, 2002, 2008); it works within the framework of geometric optics. There are attempts to modify the model by others (e.g., Hillier et al., 1999; Helfenstein et al., 1997; Kennelly et al., 2010). There also is a similar model by Lumme and Bowell (1981). However, the Hapke model has been in the main stream of planetary photometry for a long time. Unlike more rigorous approaches that use the equations of radiative transfer theory (e.g., Mishchenko et al., 1999), the Hapke model takes the shadow-hiding effect into consideration more-or-less successfully. It is no exaggeration to say that this effect is principal in optical investigations of the Moon and atmosphereless celestial bodies. Therefore, in spite of a number of shortcomings, the Hapke model is widely used in the interpretation of lunar surface photometry data. We also note that the model is invertible for the optical constants of particle material (Hapke, 1993).

Can this model help one to learn more about the lunar surface?

To answer this question, again a series of absolutely calibrated lunar images that were characterized in Velikodsky et al. (2011); <http://astrodata.univer.kharkov.ua/moon/albedo/> were used to map the parameters of the Hapke model. This procedure requires fitting a theoretical curve to the observed phase dependence for each point of the lunar disk. The Hapke equations are rather cumbersome, therefore, the procedure is time consuming; it demands searching for the absolute minimum in the parametric space having a dimension equal to the number of these parameters. The larger the number of the parameters, the less stable the result becomes. The most stable result we obtained has been produced for a version of the model with four parameters ω , B_0 , h , and $\bar{\theta}$ (see Section 3.2) at the single-scattering indicatrix $p(\alpha) = 1 + \cos \alpha$.

Fig. 20 shows maps of these four parameters. The most perfect map corresponds to ω , as can be anticipated; this resembles equigonal albedo image. The amplitude B_0 is close to 1 and does not suggest information rich in content. The same is observed for the parameter h that slightly varies over the disk revealing a weak trend from the limb to terminator. The map of the parameter $\bar{\theta}$ shows more details corresponding to lunar morphological units, but it exhibits longitude and latitude trends. The trends of the latter three parameters reflect the drawbacks of the model. Poorly compensating for the longitude and latitude brightness trends (see also Figs. 7 and 8), the model, however, provides satisfactory fit of phase curves. We note that the average values of the parameter $\bar{\theta}$ are of about 50° that seems to be too high. The Hapke–Hillier model suggests more realistic values of $\bar{\theta}$ (~25°) (cf. Fig. 7), but this model as well as the version developed by Hapke (2002) later operate with greater number of parameters and, hence, not always may provide unambiguous fitting and mapping. We plan to study this problem in more detail.

Anyway, the examples shown in Fig. 20 permit us to conclude that the discussed model will hardly help to better understand the lunar surface nature. On the other hand, maps of the same kind with the same source data (Velikodsky et al., 2011) were computed for the parameters A_n, μ_1, μ_2 , and m (see Fig. 21) with

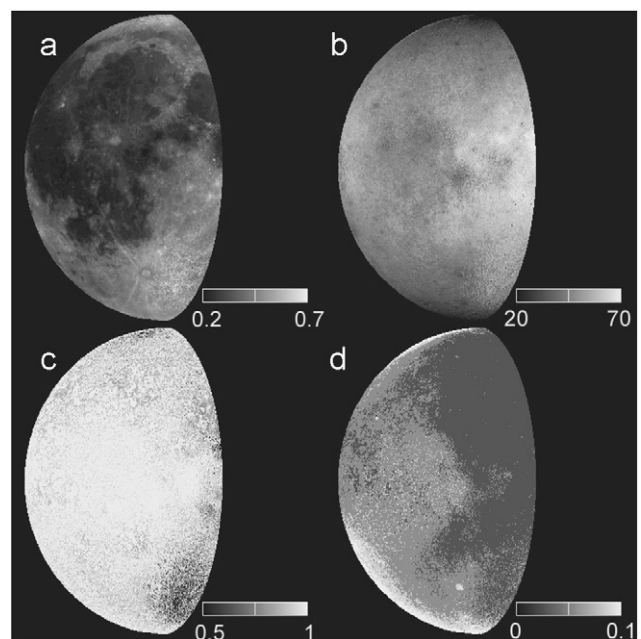


Fig. 20. Maps of Hapke's parameters found as the best fit to the source data: (a) ω ; (b) $\bar{\theta}$; (c) B_0s ; and (d) h .

the following empirical equation:

$$A(\alpha, \beta, \gamma, \lambda) = A_n \frac{e^{-\mu_1 \alpha} + m e^{-\mu_2 \alpha}}{1+m} \cos \frac{\alpha}{2} \cos \left(\frac{\pi}{\pi-\alpha} \left(\gamma - \frac{\alpha}{2} \right) \right) \frac{(\cos \beta)^{\alpha/2(\pi-\alpha)}}{\cos \gamma} \quad (23)$$

where $A_n = A_n(\lambda) = A_{eq}(0, \lambda)$, $m = m(\lambda)$, $\mu_1 = \mu_1(\lambda)$, and $\mu_2 = \mu_2(\lambda)$ (see Eqs. (12) and (21)); if it is necessary the angles α , γ , and β can be calculated through i , e , and φ with Eqs. (1) and (2). Formula (23) summarizes data presented in Sections 3.2 and 3.3. The maps shown in Fig. 21 have much more sense in relation to the lunar morphological units, than the distributions depicted in Fig. 20. Eq. (23) much better compensates for the longitude and latitude brightness trends on the lunar disk; the computing is more stable and computer time is incomparably shorter, though formula (23) exploits the same number of parameters as the used version of Hapke's model does. Formula (23) also provides an excellent fit of phase curves (see Fig. 22).

The question arises: Why do planetologists so readily use the Hapke model for interpretation of photometrical data? The answer is fairly obvious: any experimental data need to be somehow analyzed. While there are much simpler and more reliable

formulas, the Hapke model is a standard that people are all familiar with. This provides a feeling of comfort and satisfaction, like a well worn pair of slippers.

4. Spectrophotometry

Spectrophotometry is the most elaborate optical remote-sensing technique in lunar studies. Unlike photometry and especially polarimetry, many research groups contribute to these investigations. In fact, special large reviews are needed to overview lunar spectrophotometry results. However, we restrict the volume of this section and number references to keep a balance between this and the other optical techniques we considered.

4.1. Introduction

Spectral studies of the Moon have been carried out for many decades. The wavelength dependence of lunar light flux mimics the solar spectrum including all Fraunhofer lines. In the ratio of the lunar and solar spectra the Fraunhofer line structure should be well compensated. This became possible when solar spectral data reached high accuracy and rather precise facilities were produced. T. McCord, C. Pieters, P. Lucey, and others were pioneers of spectral measurements of the Moon (e.g., McCord et al., 1972; Pieters, 1978) and their interpretation (e.g., Adams, 1974; Adams and McCord, 1971; Lucey et al., 1995, 1998, 2000a,b). The spectral method is now a quantitative remote-sensing tool for the chemical/mineralogy examination of the lunar surface.

The reflectance spectra of the lunar soil in the visible, near-UV, and near-IR ranges (0.3–2.3 μm) are poor in details (Fig. 4). In the NUVVIS intervals one observes a reflectance decrease with a decrease in wavelengths, which can be associated with the effect of UV silicate absorption and absorption bands related to the charge transfer of the oxygen–metal and metal–metal types (Burns, 1993). Submicroscopic metallic iron in regolith particles is another important factor affecting the slope of lunar spectrum (Hapke, 2001). Near 1 and 2 μm, there are weak crystal field bands of the d–d type related to the Fe²⁺ ions in the minerals of the plagioclase, pyroxene, and olivine series (Burns, 1993).

The detection of “lunar water” was an extremely exciting finding (Pieters et al., 2009a; Clark, 2009; Sunshine et al., 2009). We here consider the spectral detection of superficial water that reveals itself in a 3 μm band that is due to the O–H stretching mode of OH/H₂O compounds. This band is observed for water ice as well as for crystal water and hydroxyl. To study the absorption feature near 3 μm for the Moon is not simple task. At λ > 2.2 μm

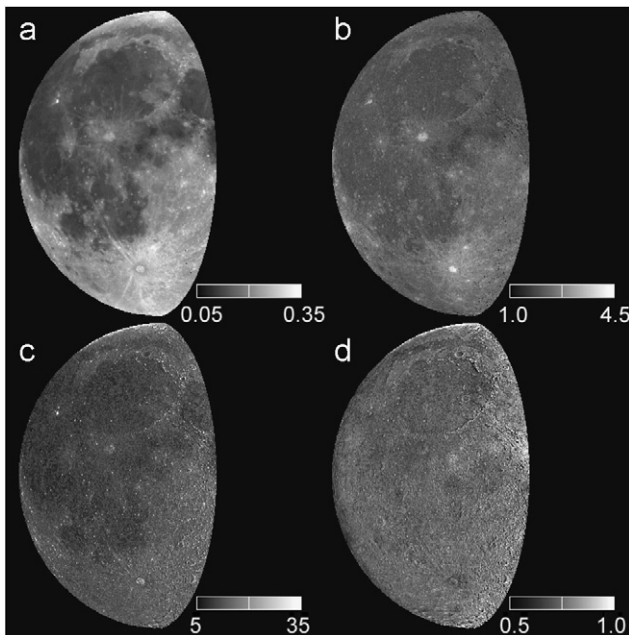


Fig. 21. Maps of the parameters of the empirical model (23) found as the best fit to the source data: (a)–(d): correspond to A_n , m , μ_1 , and μ_2 , respectively.

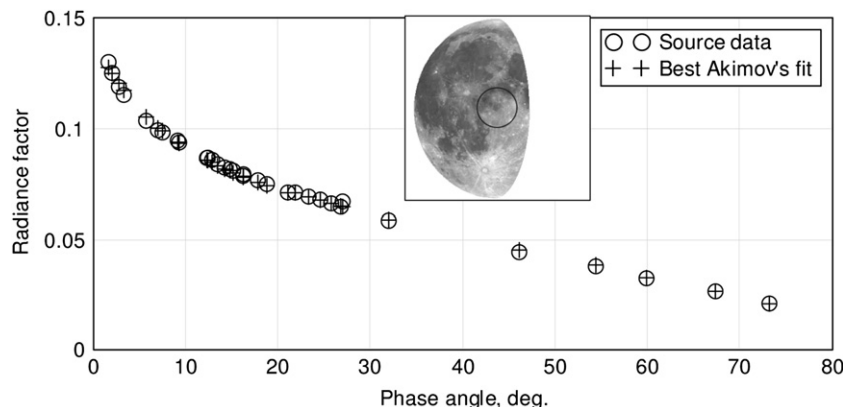


Fig. 22. A phase curve of the radiance factor for a large area located in the center of lunar nearside (see inset). Calculations were carried out with formula (23) ($A_n=0.14$, $m=2$, $\mu_1=10$, and $\mu_2=0.7$).

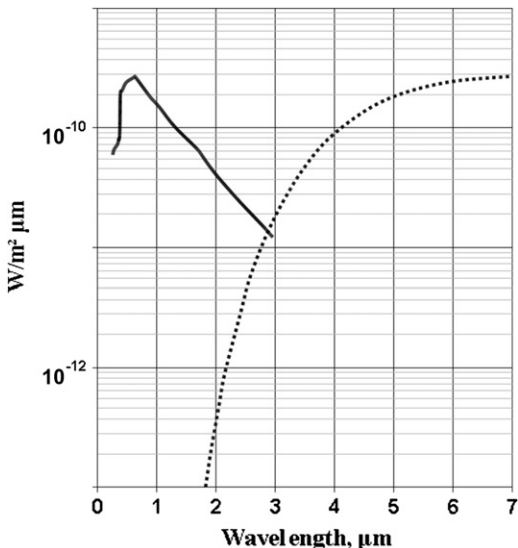


Fig. 23. Spectral distributions of energy received from 1 km² in the center of the lunar disk at $\alpha=0$ and $T_0=400$ K. The calculation of distributions was made with the Plank formula.

the lunar emission component begins to contribute significantly to the total flux departing from the Moon. Fig. 23 depicts spectral distributions of energy received from 1 km² in the center of the lunar disk at $\alpha=0$ and the temperature of subsolar point 400 K. Thus, measurements of the water signature near 3 μm require a thorough removal of the emission component whose contribution to the total flux increases very sharply with wavelength. This is a serious problem that may significantly influence the final results and their interpretation.

Due to the simplicity of the reflection spectra, which is a consequence of mineralogy simplicity, their representation in the form of several color ratios is often used. The color ratios $C(0.60/0.40 \mu\text{m})=A(0.60 \mu\text{m})/A(0.40 \mu\text{m})$ and $C(0.95/0.75 \mu\text{m})=A(0.95 \mu\text{m})/A(0.75 \mu\text{m})$ appear to be diagnostic (the wavelengths are indicated roughly). For example, the ratio $C(0.60/0.40 \mu\text{m})$ correlates with titanium content; whereas, $C(0.95/0.75 \mu\text{m})$ relates rather to Fe abundance (Johnson et al., 1991a,b; Lucey et al., 1995, 1998, 2000a,b; Blewett et al., 1997; Shkuratov et al., 2003b, 2005a; Korokhin et al., 2008). Estimates of iron and titanium allow one to distinguish among lunar surface materials. These elements are expressed as oxides, FeO and TiO₂, because they are chemically bonded to oxygen inside minerals.

Combinations of albedo at various wavelengths also allow the mapping of regolith maturity and mineral abundances (Lucey, 2004; Pieters et al., 2006; Shkuratov et al., 2005b). Estimates of FeO and TiO₂ content in combination with radar data appear to be useful in the first-approximation mapping of the thickness of the regolith layer (Shkuratov and Bondarenko, 2001) and even in prognoses of helium-3 abundance (Johnson et al., 1991a,b; Shkuratov et al., 2001). In the latter case, this is possible due to the close correlation of helium-3 abundance with content of TiO₂ that is a chromophore (Taylor, 1994).

The topics outlined above are the main subject of the following sections.

4.2. Spectral bands in visible and NIR range

Spectral albedo bands bear information about the ions producing the bands, their concentration, and the parameters of the crystal lattice. While the sort and coordination position (M1 or M2) of ions of transition elements, such as Fe, Ti, Cr, Mn, may be established from a quantum mechanical consideration (Burns,

1993), the concentration of the elements cannot, in general, be directly calculated with spectral albedo measurements of regolith-like media. The depth (intensity) of the bands depends not only on the concentration, but also on the sizes and shapes of particles in addition to the structure of a particulate surface. Retrieving the real and imagery parts of the refractive index, $m=n+ik$, of lunar soil material from spectral measurements of such a surface is a very difficult problem. Theories considering particles compared to the wavelength (e.g., Tishkovets and Mishchenko, 2009) are still impracticable. Meanwhile, models based on the geometrical optics approximation are considered to be too simplified, but appeared to be convenient solutions when tested with laboratory measurements. Two similar 1D models (Hapke, 1993; Shkuratov et al., 1999b) are widely used to retrieve the spectral dependence of the absorption coefficient $\tau=(4\pi\kappa/\lambda)l$, where l and λ are the characteristic length of light propagation in particles and wavelength, respectively. For a randomly shaped particle, the length l approximately equals $0.2D$, where D is the maximal size of the particle (Shkuratov and Grynko, 2005).

The model (Shkuratov et al., 1999b) enables the researcher to estimate reflectance A of a particulate surface as a function of λ . The parameters of the model are the complex refractive index of particles, the volume fraction q filled by the particles, and the characteristic length l . The following expressions have been derived (Shkuratov et al., 1999b):

$$A = \frac{1+(qr_b)^2-(qr_f+1-q)^2}{2qr_b} - \sqrt{\left(\frac{1+(qr_b)^2-(qr_f+1-q)^2}{2qr_b}\right)^2 - 1}, \quad (24)$$

where r_b and r_f are the backward and forward components of the 1D particle indicatrix

$$r_b = R_b + \frac{(1-(1-R_e)/n^2)(1-R_e)^2 \exp(-2\tau)}{2n^2(1-(1-R_e)/n^2)\exp(-\tau)}, \quad (25)$$

$$r_f = R_f + \frac{(1-R_e)^2}{n^2} \exp(-\tau) + \frac{(1-(1-R_e)/n^2)(1-R_e)^2 \exp(-2\tau)}{2n^2(1-(1-R_e)/n^2)\exp(-\tau)}, \quad (26)$$

where $R_e=R_b+R_f$, R_b and R_f are the over-angle-averaged backward and forward reflectance coefficients of single reflection from the particle interface; in the range of real n from 1.4 to 1.8, the following approximations are satisfactory:

$$R_b \approx (0.28n-0.20)R_e, \quad (27)$$

$$R_e \approx r_0 + 0.055, \quad (28)$$

where $r_0=(n-1)^2/(n+1)^2$ is the Fresnel reflection coefficient at normal incidence. The albedo expressed by formula (24) can be considered as A_n in Eq. (23). The physical meaning of albedo in Eq. (24) was analyzed in Shkuratov et al. (1999b) and Shkuratov and Grynko (2005). Expressions (23) and (24) are simple and can be implemented more easily than the Hapke equations for mixture modeling, e.g., to determine mineral content (Lucey, 2004; Cahill et al., 2009, 2010; Yan et al., 2010). The model also is invertible, i.e., starting from the surface albedo and supposing the values of n and l are known, one can solve Eq. (24) for the imaginary part κ of the refraction index of the particle material (Shkuratov et al. 1999b):

$$\kappa = t\lambda/4\pi l, \quad (29)$$

where

$$\tau = -\ln \left[\frac{b}{a} + \sqrt{\left(\frac{b}{a} \right)^2 - \frac{c}{a}} \right], \quad (30)$$

$$a = \frac{(1-R_e)^2}{n^2} \left(y \left(1 - \frac{1-R_e}{n^2} \right) + q(1-R_e) \right), \quad (31)$$

$$b = yR_b \left(1 - \frac{1-R_e}{n^2} \right) + \frac{q}{2}(1-R_e)^2 \left(1 + \frac{1-R_e}{n^2} \right) - (1-R_e)(1-qR_b), \quad (32)$$

$$c = 2yR_b - 2(1-R_e)(1-qR_b) + q(1-R_e)^2, \quad (33)$$

$$y = (1-A)^2/2A. \quad (34)$$

The model also allows estimates of the change in albedo of a particulate surface if particle size and/or composition are modified: the function $\kappa(\lambda)$ is calculated from $A(\lambda)$; then $\kappa(\lambda)$ or I can be changed and $A(\lambda)$ is recalculated for new $\kappa(\lambda)$ or I . For example, to take into account the presence of nanophase ($\ll \lambda$) inclusions of iron (npFe⁰), which were found in regolith particles, values of κ can be modified (Shkuratov et al. 1999b) as

$$\kappa_{\text{eff}}(\lambda) = \kappa(\lambda) + c_0 \kappa_{\text{Fe}}(\lambda), \quad (35)$$

where the contribution of npFe⁰ inclusions per unit volume fractions to absorption is

$$\kappa_{\text{Fe}}(\lambda) = \frac{3n}{2} \text{Im} \left(\frac{\tilde{\epsilon}(\lambda) - 1}{\tilde{\epsilon}(\lambda) + 1} \right), \quad (36)$$

$\tilde{\epsilon}(\lambda)$ being the ratio of the complex dielectric constant of Fe⁰ to that of a regolith particle at a given wavelength, c_0 being the volume fraction of such inclusions.

It has been demonstrated that the optical properties of bulk soils are dominated by the smaller size fractions with $D \sim 10 \mu\text{m}$ (Pieters et al., 1993); this is believed to be due to larger particles being covered by smaller particles in a natural soil. For particle sizes $\sim 10 \mu\text{m}$ the geometric optics approximation would be applied with caution for visible and especially NIR spectral ranges. Thus, the models by Hapke (1993) and Shkuratov et al. (1999b) may suggest only first-approximation estimates of $\kappa(\lambda)$. The models were compared with each other (Poulet et al., 2002; Merlin et al., 2010), revealing a small difference in the 1D indicatrix of the particles.

The models allow one to study spectra of various material mixtures (e.g., Shkuratov et al., 1999b; Lucey, 2004; Cahill et al., 2009, 2010; Yan et al., 2010). For this purpose a normalized mixture of single-particle albedo is produced: $r = k_1 r_1 + k_2 r_2$, where $r = r_b + r_f$, $k_1 + k_2 = 1$ (k_1 and k_2 are relative portions of the materials), the indexes 1 and 2 correspond to different materials: $r_1 = r_1(\tau_1, l_1, n_1)$ and $r_2 = r_2(\tau_2, l_2, n_2)$. Such a mixing is valid when grains of different minerals are homogeneously mixed. If a powdered surface consists of patches of different materials and patch sizes are much greater than the grain size, then surface albedo mixing is possible: $A = S_1 A_1 + S_2 A_2$, where S_1 and S_2 are relative areas occupied with the materials. The latter kind of mixing was used for a first-order mapping of the impact melt material within the crater Copernicus (Pinet et al., 1993). Owing to this analysis olivine was detected not only within the three central peaks but also along a portion of the crater rim.

One prospective way to develop the models from 1D to 3D is a Monte-Carlo ray-tracing method of light propagation in arbitrary shaped particles and particulate media thereof (Grundy et al., 2000; Gryko and Shkuratov, 2002, 2003; Shkuratov and Gryko, 2005).

It should be emphasized that, even if the function $\kappa(\lambda)$ is estimated, e.g., with Eq. (29), it does not mean that one may easily calculate the concentration c_0 of a chromophore element. In most cases the function $\kappa(c_0)$ is unknown, as it depends also on the intensity of the quantum transition characterized with the following volume integral $\int \psi_g \hat{M} \psi_e^* dV$ where ψ_g is the wave function of the ground state, ψ_e^* is the wave function of the excited state (* is the complex conjugation), and \hat{M} is the operator of

transition between these states. The integral is extremely complicated for computations in realistic cases.

The positions of absorption bands can be established more reliably, though they also depend slightly on particulate media properties (Shkuratov et al., 1999b). In the UV and visible ranges, lunar albedo decreases with a decrease of λ due to strong charge transfer bands: $O^{2-} \rightarrow Fe^{2+}$ and $O^{2-} \rightarrow Ti^{4+}$ centered near $0.2 \mu\text{m}$ (Burns, 1993). The term "charge transfer" is rather conditional; in fact, in the crystal lattice the hybrid (molecular) orbitals arise between anions and cations. These orbitals are excited with photon absorption. A photon with some probability may be re-emitted or its energy diffuses as heat.

Plagioclase feldspars, pyroxenes, olivines, and ilmenite—their ideal formulas are, respectively, $(Na,Ca)(Si,Al)_4O_8$, $(Mg,Fe^{2+},Ca)SiO_3$, $(Mg,Fe)_2SiO_4$, and $FeTiO_3$ —are the main minerals of the lunar surface. Plagioclases predominate in lunar highlands; whereas, the other minerals compose the maria. Different important impurities are possible in these minerals, e.g., Fe^{2+} in plagioclases. The minerals reveal crystal field bands formed by electron transitions of the d - d type between split levels of Fe^{2+} ions (Burns, 1993). Iron, being a transition element, has the unfilled external d -shell; hence, electrons placed on the five orbitals d_{xy} , d_{yz} , d_{zx} , $d_{x^2-y^2}$, and d_{z^2} are weakly bound with the nucleus. The wave functions of the electrons in the d -orbitals have different shapes, but are of the same energy (degenerate) if the atom is in a free space. When the atom (cation) is placed in a crystal lattice, the orbitals due to their different shapes are disturbed differently by neighboring anions. The disturbance removes the degeneracy and the energy levels split, which allows quantum transitions with photon absorption. For example, for orthopyroxene, where Fe occupies the positions of the second metal (M2) in the anion surroundings with octahedral symmetry, the splitting produces two bands centered near 0.90 and $1.85 \mu\text{m}$. For olivine the splitting produces three overlapping bands near $1 \mu\text{m}$. Fig. 24 shows laboratory spectra of the main minerals composing the lunar surface, which were obtained with the RELAB spectrometer at the standard illumination/observation geometry (Pieters, 1983). The data are adapted from Cloutis and Gaffey (1993), presenting plagioclase (band near $1.3 \mu\text{m}$), olivine (triple band near $1.05 \mu\text{m}$), orthopyroxene (bands near 0.93 and $1.95 \mu\text{m}$), clinopyroxene (bands near 1.03 and $2.32 \mu\text{m}$), and ilmenite (almost structureless).

Impurities in the crystal lattice significantly influence the splitting through a change of distances between ions. For instance, in pyroxenes the presence of Ca increases the distances, which shifts both the pyroxene bands to longer wavelengths. Thus, the positions of the band minima λ_{\min} near 1 and $2 \mu\text{m}$ can

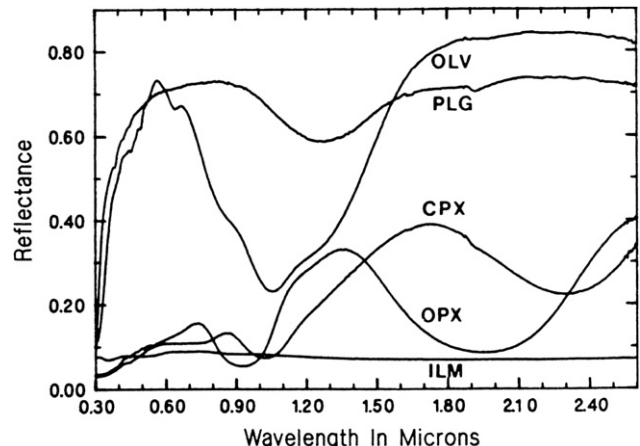


Fig. 24. Laboratory spectra of the main minerals composing the lunar surface (Cloutis and Gaffey (1993)): plagioclase (PLG), olivine (OLV), orthopyroxene (OPX), clinopyroxene (CPX), and ilmenite (ILM).

be very prognostic. These positions enable one to judge the type of pyroxenes present in the lunar soil. As has been shown by Adams (1974), orthopyroxenes have smaller values of λ_{min} for both the bands than clinopyroxenes do. The Adams (1974) diagram (see Fig. 25) was built for samples with different Ca content: the content increases from left to right.

The lunar absorption bands can be asymmetric because of mutual overlapping, e.g., the band asymmetry near 1 μm may be associated with the fact that the pyroxene and olivine bands are superposed on each other, the pyroxene band usually being more intense. Thus, measurements of the band asymmetry may in principle suggest information about the ratio of pyroxene and olivine. Nevertheless, to find this ratio is not a simple task, as olivine content is usually lower than pyroxene and the reliability of such a determination is low. Plagioclase feldspars often have a broad absorption band around 1.3 μm . However, one of three olivine bands occurs around 1.25 μm and Fe^{2+} in the M1 site of pyroxene may yield a 1.2 μm band (Klima et al., 2007; Noble et al., 2006), producing a false plagioclase feature. It is a complex task to distinguish the relative contribution of each when a 1.2–1.3 μm band is accompanied with deeper 1 μm absorption.

Sometimes, unequivocal olivine detection is possible. Carrying out telescopic observations of large craters, Pieters (1982) came to the conclusion that the Copernicus peak reveals olivine-rich

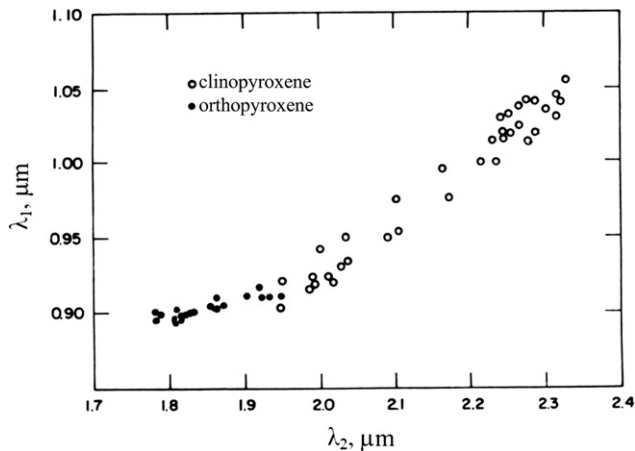


Fig. 25. The Adams diagram for pyroxenes. The vertical and horizontal axes correspond to the wavelengths of 1 and 2 μm band centers, respectively (Adams, 1974).

lithologies. Fig. 26 shows a spectral comparison of different details of the craters Tycho and Copernicus. Unlike the Tycho central peak, spectra of the Copernicus peak near 1 μm are noticeably broader and do not exhibit the 2 μm band. Later, using the Spectral Profiler onboard the lunar explorer Kaguya, many exposures of olivine on the Moon were found. These occur at locations in concentric regions around the South Pole-Aitken, Imbrium, and Moscovense impact basins where the crust is relatively thin. The exposures can be attributed to an excavation of the lunar mantle at the impacts that formed the basins (Yamamoto et al., 2010).

The lunar highland regolith layer is believed to consist of anorthosite composition material. Anorthosite is a plutonic rock composed largely of calcic plagioclase. In fact, lunar anorthosite was remotely identified only by high albedo, as this material shows lack of the absorption band near 1.3 μm . The fact that the spectral signature has been detected in laboratory measurements (Fig. 24), but is absent in telescope observations (e.g., Tompkins and Pieters, 1999; Hawke et al., 2003) is explained by shock metamorphism. Shock waves accompanying meteorite impacts of different scales disorder the crystal lattice of lunar plagioclase, forming diaplectic glasses (Adams et al., 1979). Plagioclase is the only mineral known to become sufficiently amorphized with shock-loading to lose its absorption bands. The Kaguya Spectral Profiler discovered crystalline plagioclase (1.3 μm band) in the central peaks of several highland craters, e.g., in a few parts of the crater Tycho peak (Matsunaga et al., 2008; Otake et al., 2009). Then, confirming Kaguya findings, Pieters et al. (2009c) have identified crystalline plagioclase in the Inner Rook Mountains of the Orientale Basin with the Chandrayaan-1 M³. To further investigate, if Fe-bearing plagioclase-rich rocks globally exist, is important, because this is the fundamental assumption for the magma-ocean hypothesis (Taylor et al., 2006).

The spectral variability of the lunar surface surprises more and more. Recently, small areas ($< 1 \text{ km}$) were discovered having presumably spinel-rich composition (Sunshine et al., 2010; Pieters et al., 2010, 2011). While spinel group minerals are rather common in lunar samples, they usually occur as accessory phases ($< 10\%$), and the finding of the locations with the spectral domination of spinel was unexpected. Lunar olivines usually contain small, but spectrally significant abundances of small inclusions of dark Cr-spinels (e.g., Papike et al., 1998) that have strong absorption at $\lambda > 1.6 \mu\text{m}$ (Cloutis et al., 2004; Isaacson and Pieters, 2010); typical terrestrial olivines do not have such a feature. Fig. 27 presents spectra obtained from three locations with spinel-rich composition in Sinus Aestuum.

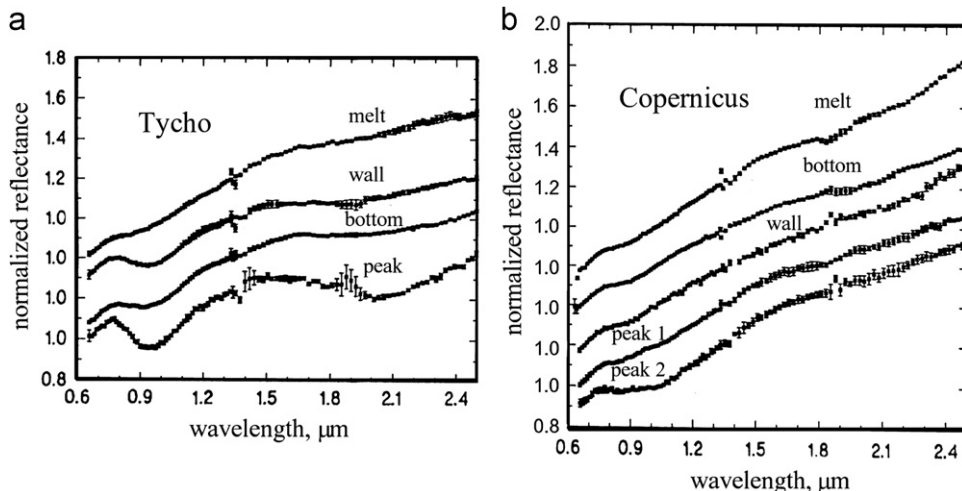


Fig. 26. Spectra of details in the craters (a) Tycho and (b) Copernicus measured by Pieters (1982).

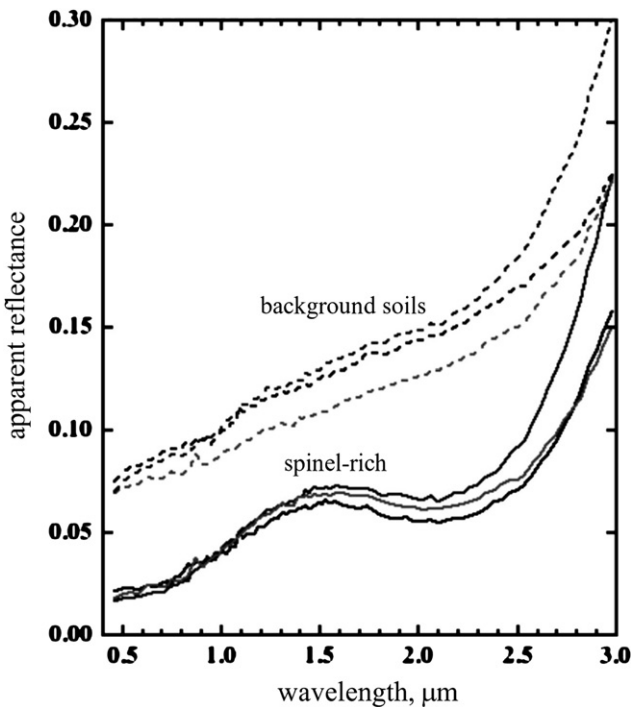


Fig. 27. Representative spectra of three locations with spinel-rich composition (solid lines) from Sinus Aestuum and nearby background soils (dashed lines) (Sunshine et al., 2010). Despite the thermal emission (see background soils), the deposits clearly have very strong 2 μm features and a weak or absent 1 μm band, as is characteristic of spinel.

This region includes dark pyroclastic mantle deposits (Weitz et al., 1998). For comparison, surrounding background soils (dashed lines) are shown too. Despite the thermal emission beginning approximately from 2.4 μm , the spinel-rich deposits have strong 2 μm features and a weak or absent 1 μm band, as is characteristic of spinel (Cloutis et al., 2004). The spinel composition (likely chromite) and their association with dark mantle deposits are consistent with a volcanic origin of the unusual locations (Sunshine et al., 2010). Additional small, isolated spinel deposits were found on the farside, but restricted to the inner ring of Moscovense (Pieters et al., 2010, 2011). Studies of the puzzling spinel-rich units could provide new insight into the lunar volcanic processes.

Pure mineral grains do not dominate the mature regolith. Its main component is agglutinates, the spectra of which significantly differ from the simple mixture of mineral grains of the same chemical composition. Agglutinates are regolith particles welded together into aggregates of very diverse morphologies; agglutinates include significant amounts of glasses generated by impact melting (Adams and McCord, 1971). Thus, the agglutinitic glasses are a quenched product of silicate melts. Fig. 28a illustrates the differences between mature and immature lunar material using the spectra of Apollo-11 samples of similar chemical composition. This figure also shows that combined studies of the 1 and 2 μm absorption bands may suggest important information on the agglutinate content. The spectrum of agglutinates has an absorption band near 1 μm and virtually no 2- μm band (Fig. 28a). The reason may be clarified with laboratory simulations by Moroz et al. (1993): pyroxenes are susceptible to melting to a greater extent than olivines during the impact re-working of lunar soils. This can conduce to the primary accumulation of olivines in agglutinates; olivines do not have the 2- μm band at all.

Space weathering phenomena include not only agglutinate formation. Another important process is the creation of nanophase iron (npFe^0) globules in superficial zones (rinds) and inside of the lunar

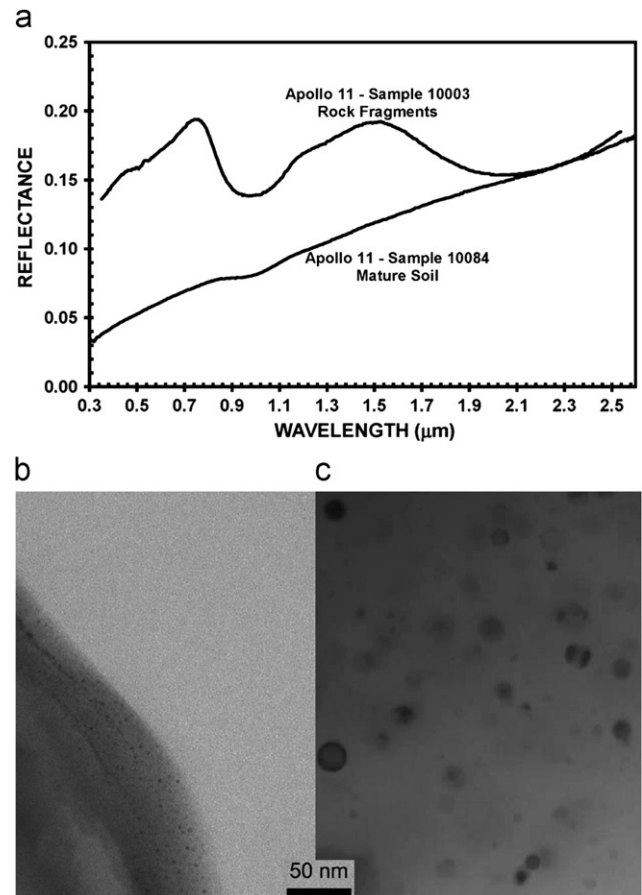


Fig. 28. Characteristics of Apollo-11 samples of different maturity degree: (a) spectrum of bedrock fragments and a mature soil composed of space weathered bedrock fragments (Gaffey, 2010); (b) transmission-electron-microscopy image of a typical npFe^0 -bearing rind surrounding a grain of lunar soil 10,084 and (c) compared to a typical region of agglutinitic glass (Noble et al., 2007). The npFe^0 in agglutinates on average is considerably larger than the sizes seen in the rinds.

regolith particles (Housley et al., 1973; Morris, 1980; Hapke et al., 1975; Hapke, 2001; Keller and McKay, 1993). The average size of npFe^0 globules in rinds observed with electron microscopes is only about 3 nm. Inside of agglutinate particles the globules are noticeably larger (5–20 nm) (James et al., 2002). Fig. 28b,c shows the transmission electron microscope images of a npFe^0 -bearing rind of a grain of lunar soil 10084 (b) and a typical internal region of agglutinitic glass (c) (Noble et al., 2007) at the same scale. The rinds of regolith particles are amorphous silicates that were deposited from vapors produced by hypervelocity micrometeorite impacts (e.g., Taylor et al., 2001; Hapke, 2001). The iron Fe^0 may have dissociated from Fe-compounds in a high temperature ($>3000^\circ$) vapor phase and then condensed as globules on particle surfaces. The Fe^0 deposits can be recurred and accumulated. These particle coats can be produced also by deposition of atoms sputtered off of soil grains by energetic solar wind particles (Hapke, 2001). Repeated impact heat and/or melt may stimulate the diffusion of the rind Fe^0 globules into the particle interior, their merging, and formation of larger globules. The presence of solar wind hydrogen in agglutinitic melts can promote the generation of immiscible Fe^0 droplets solidified as globules.

This nanophase iron modifies the spectral properties of the lunar surface and surfaces of bodies lacking atmospheres when exposed to the space environment (Hapke, 2001; Noble et al., 2007; Gaffey, 2010). The cumulative abundance of this weathering-derived npFe^0 substantially decreases the measured strength of all absorption

bands, especially for soils from the FeO-rich maria. Moreover, with increased weathering, the spectra of lunar soils exhibit systematically lower albedo and redder spectral slopes than the bedrock lithologies from which they were derived (Fig. 28a). The investigation by Noble et al. (2007) has provided persuasive experimental proofs for npFe⁰ altering the spectral properties of the lunar soils. The authors have prepared a suite of analog soils to explore the optical effects of npFe⁰. By varying the size and concentration of npFe⁰ they found significant systematic changes in the Vis/NIR spectra: smaller npFe⁰ (< 10 nm in diameter) dramatically reddens spectra in the visible wavelengths while leaving the infrared region largely unaffected. Larger npFe⁰ globules (> 40 nm) lowers the albedo across the Vis/NIR range with little change in the overall shape of the continuum.

4.3. Emission removal from reflectance spectra

The 3 μm water band occurs in the spectral range where the reflectance and emission components of lunar radiation overlap each other (Fig. 23). The thermal emission may distort the shape even of the 2-μm pyroxene, changing spectrally determined pyroxene composition. The emission contributes to water and hydroxyl absorptions, reducing them in strength, lowering apparent abundances. Thus, it is necessary to remove the emission component in order to adequately interpret the band. This is a difficult problem, as the emission contribution is a function of the surface temperature T that, in turn, depends on the surface topography. In the approximation of even surfaces the problem can be stated as follows.

We write the total (apparent) brightness $B(\alpha, i, e, \lambda, T)$ of a particulate surface accounting for all of the radiation leaving the surface in a given direction. This function presents the full balance of energy that enters and leaves the lunar surface

$$B(\alpha, i, e, \lambda, T_{\text{Moon}}) = \frac{E_0(\lambda)A_n(\lambda)}{\pi} \frac{F(\alpha, i, e, \lambda)}{\cos e} + \varepsilon(e, \lambda)B_0(\lambda, T_{\text{Moon}}), \quad (37)$$

where $E_0(\lambda)$ is the solar spectral irradiance that can be computed with a spectral distribution of solar energy (e.g., Neckel, 2000) or approximately as

$$E_0(\lambda) = \frac{\pi R_{\text{Sun}}^2}{L_{\text{Sun}}^2} B_0(\lambda, T_{\text{Sun}}) = \frac{\pi R_{\text{Sun}}^2 C_1}{L_{\text{Sun}}^2 \lambda^5} \left(\exp\left(\frac{C_2}{\lambda T_{\text{Sun}}}\right) - 1 \right)^{-1}, \quad (38)$$

where the radius of the Sun, the distance between the Sun and the Earth (Moon), and the temperature of the solar photosphere are taken as follows: $R_{\text{Sun}}=7 \times 10^5$ km, $L_{\text{Sun}}=1.5 \times 10^8$ km, and $T_{\text{Sun}}=5950$ K; $B_0(\lambda, T)$ is Planck's function, i.e., the spectral radiance from blackbody at a given temperature, $C_1=1.1911 \times 10^8$ [W μm⁴/m² sr] and $C_2=14,388$ [μm K].

The function $\varepsilon(e, \lambda)$ is the directional emissivity (emittance). For a surface in thermal equilibrium, the emittance equals the absorptance that can be expressed through reflectance; this is the gist of Kirchhoff's law allowing the following equation (Nicodemus, 1965):

$$\varepsilon(e, \lambda) = 1 - r_{hd}(e, \lambda), \quad (39)$$

where $r_{hd}(e, \lambda)$ is the hemispherical-directional reflectance

$$r_{hd}(e, \lambda) = A_n(\lambda)\zeta(e, \lambda) = \frac{A_n(\lambda)}{\pi \cos e} \int_0^{2\pi} d\varphi \int_0^{\pi/2} F(i, e, \varphi, \lambda) \sin i di, \quad (40)$$

Thus, the observed reflectance is

$$r(\alpha, i, e, \lambda, T_{\text{Moon}}) = A_n(\lambda) \frac{F(\alpha, i, e, \lambda)}{\cos e} + \frac{L_{\text{Sun}}^2 (1 - A_n(\lambda)\zeta(e, \lambda))}{R_{\text{Sun}}^2 E_0(\lambda)} \left(\exp\left(\frac{C_2}{\lambda T_{\text{Moon}}}\right) - 1 \right)^{-1}. \quad (41)$$

For the determination of the 3 μm band in the spectral measurements by Pieters et al. (2009a), Clark (2009), and Sunshine et al. (2009) the solar spectral irradiance function $E_0(\lambda)$ was taken from

<http://rredc.nrel.gov/solar/spectra/am0/modtran.html> (Clark and Sunshine, 2011, personal communication). The lunar temperature T_{Moon} in Eq. (41) can be used as a free parameter for a fitting procedure (e.g., Pieters et al., 2009a; Clark, 2009; Clark et al., 2011) or separately measured (e.g., Sunshine et al., 2009). If thermal equilibrium is assumed, the T_{Moon} may be estimated with the Stefan-Boltzmann law

$$T_{\text{Moon}} = T_0 \sqrt[4]{(1 - A_{dh}) \cos i}, \quad (42)$$

where T_0 is the temperature of the surface when $\varepsilon=1$, and solar radiance falls normally, i.e., $T_0 = \sqrt[4]{C/\sigma}$ and A_{dh} is the spectrally integrated directional-hemispherical albedo

$$A_{dh} = \frac{\int_0^\infty d\lambda \int_0^{2\pi} d\varphi \int_0^{\pi/2} E_0(\lambda) A_n(\lambda) F(i, e, \varphi, \lambda) \sin i de}{\pi \cos i \int_0^\infty E_0(\lambda) d\lambda} \\ = \frac{1}{C} \int_0^\infty E_0(\lambda) A_n(\lambda) \zeta(i, \lambda) d\lambda. \quad (43)$$

The value C is the solar constant, $C=1367$ [W/m²], and σ is the Stefan-Boltzmann coefficient, $\sigma=5.67 \times 10^{-8}$ [W/m² K⁴]; $T_0 \approx 394$ K. The function $F(i, e, \varphi, \lambda)$ depends on λ comparatively weakly, thus, using an approximation, $A_{dh} \approx \zeta(i) A_n(\lambda_m)$, where λ_m is a wavelength near the maximum of $E_0(\lambda)$ ($\lambda_m=0.53$ μm), one may obtain the following equation:

$$A_n(\lambda) = \frac{r(\alpha, i, e, \lambda, T) - \frac{L_{\text{Sun}}^2}{R_{\text{Sun}}^2} E_0(\lambda)}{\frac{F(\alpha, i, e)}{\cos e} - \frac{\zeta(e) L_{\text{Sun}}^2}{R_{\text{Sun}}^2 E_0(\lambda)}} \left(\exp\left(\frac{b_{\text{Moon}}/\lambda}{\sqrt[4]{(1 - \zeta(i) A_n(\lambda_m)) \cos i}}\right) - 1 \right)^{-1} \quad (44)$$

where $b_{\text{Moon}}=36.6$ μm.

If $F=\cos i \cos e$, then $\varepsilon(\lambda)=1-A_n(\lambda)$, as $\zeta(e, \lambda)=1$ in Eq. (40). Clark (2009) neglected the dependence of emissivity on surface albedo, considering $A_n(\lambda)=0$, and used the Lambertian photometric function F . This is a rather rough approximation. Indeed, Fig. 29 shows the lunar spectrum SP3 of a south polar region obtained with Cassini (Clark, 2009) (curve 1). After correction of this spectrum using the Clark approach at $T_{\text{Moon}}=387$ K, one may obtain curve 3. To show the importance of relationship (39), we plot the spectrum SP3 corrected with formula (44) using the photometric function (23) at $\alpha=70^\circ$, $e=60^\circ$, $i=70^\circ$, $m=0.55$, $\mu_1=0.8$, and $\mu_2=7$ (curve 2) and the same temperature. Curves 2 and 3 are noticeably different.

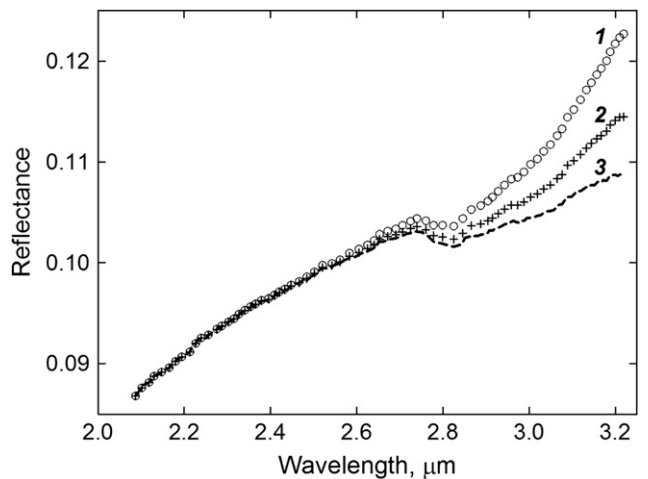


Fig. 29. Lunar spectrum SP3 (curve 1) corresponding to a south-polar region (Clark, 2009), the same spectrum corrected by the Clark method with the assumption that the emissivity equals 1 (curve 3), and similar result obtained with formula (44). For the two latter cases $T_{\text{Moon}}=387$ K. To compute curve 2, we used in Eq. (44) $\alpha=70^\circ$, $e=60^\circ$, and $i=70^\circ$ ($\zeta(i)=0.60$, $\zeta(e)=0.41$) and $m=0.55$, $\mu_1=0.8$, and $\mu_2=7$ in Eq. (23).

As has been noted, Eq. (41) is valid in a first approximation, when a surface under study is rather even. However, the lunar surface is rough in all scales. The surface distribution of the reflected and emitted components depends considerably on the topography (e.g., Clark et al., 2011; Bandfield et al., 2011). Additional important factor, which should be taken into account, is multiple scattering between elements of roughness (Clark et al., 2011). To take into account this, a computer ray-tracing model, e.g., like presented in Shkuratov et al. (2005c), would need to be constructed. Our calculations for random surfaces with Gaussian distributions of heights and slopes show that the multiple scattering can be noticeable at characteristic slopes of the lunar topography more than 30° (Shkuratov et al., 2005c).

Another restriction of the consideration is the thermal equilibrium. It is clear that near the lunar terminator, where illumination conditions change rather fast, this assumption does not hold, and Kirchhoff's law is violated. Eq. (42) also may not hold and, therefore, it is better to measure T_{Moon} separately, as has been done in Sunshine et al. (2009). Thus, the described technique of thermal emission removal must be applied with precaution. More sophisticated approach should be elaborated for future lunar missions that are planned to map the lunar water band with high spatial resolution.

4.4. Detecting superficial water

The presence of water ice in lunar poles was predicted many years ago (Watson et al., 1961). The term water ice is fairly conditional; in fact, an amount of hydrogen was detected; it can be in the form of molecules H_2O and/or radicals OH (e.g., Anand, 2010). The H signatures were found in the polar regions with the radar Clementine (Nozette et al., 1996) and neutron spectrometers of Lunar Prospector (Feldman et al., 2000, 2001; Elphic et al., 2007; Eke et al., 2009) and LRO (Mitrofanov et al., 2010). These measurements characterize the uppermost regolith layer $< 1 \text{ m}$.

On 9 October 2009 during the Lunar Crater Observation and Sensing Satellite (LCROSS) mission, a spent Centaur rocket struck the persistently shadowed area within the crater Cabeus, ejecting debris, dust, and vapor. This was observed by a spacecraft with cameras and optical spectrometers. Near-infrared absorbance and ultraviolet emissions supported the presence of water in the ejecta ($5.6 \pm 2.9\%$ by mass). However, in addition to water, spectral bands of a number of other compounds were observed, including light hydrocarbons, sulfur-bearing species, carbon dioxide (Colaprete et al., 2010), carbon monoxide, and even appreciable amount of mercury (Gladstone et al., 2010). The latter cannot be from the lunar surface; apparently, the source of mercury is the Centaur rocket. Then, the question about the reliability of the estimates of the water amount and other listed volatile compounds immediately arises; they at least partially can be from the rocket's materials. Nevertheless, the LCROSS mission results are considered to be direct evidence of the water presence in a thick layer of the lunar regolith of permanently shadowed areas.

Even after the *Lunar Prospector* findings (Feldman et al., 2000, 2001; Elphic et al., 2007) the discovery of the 3 μm absorption feature in lunar spectra was rather unexpected, since historically the Moon has been considered to be very dry. Traces of water in some lunar samples have been found in IR spectral measurements, but it was cautiously attributed to terrestrial contamination (e.g., Akhmanova et al., 1973; Taylor et al., 1973); perhaps, this was unjustified. The brilliant lunar-water attack undertaken by different research groups in *Science* (Pieters et al., 2009a; Sunshine et al., 2009; Clark, 2009) has significantly changed the attitude of the planetary community to the problem, generating a great number of studies. The IR-spectrometer data (Pieters et al., 2009a; Clark, 2009; Sunshine et al., 2009) correspond to radiation

scattering in the thickness of several hundreds of microns. Thus, it is necessary to distinguish between superficial and bulk lunar water.

While the *Chandrayaan-1* (Pieters et al., 2009a) mapped only the shortwave wing of the 3 μm band with high spatial resolution, the *Deep Impact* (Sunshine et al., 2009) and *Cassini* (Clark, 2009) IR spectrometers provided extended spectral coverage, but with very low resolution data. The OH/ H_2O absorption is strongest at the lunar poles. The H_2O amount at the North Pole of the Moon is estimated to be $< 0.5 \text{ wt\%}$ (Sunshine et al., 2009). Direct detection of H_2O molecules in the tenuous lunar environment at high latitudes with the neutral mass spectrometer (CHACE) onboard the Moon Impact Probe of *Chandrayaan-1* mission vindicates the presence of water on the lunar surface at higher latitudes on the sunlit side (Sridharan et al., 2010).

The OH/ H_2O feature observed by the *Deep Impact* spectrometer in the range 1.05–4.5 μm reveals a minimum at 2.8 μm (Sunshine et al., 2009), which is due to stretching vibrations of structural OH and H_2O . The 3 μm absorption is attributed to asymmetric and symmetric stretching modes of H_2O molecules. Fig. 30 shows laboratory measurements adapted from Dyar et al. (2010) demonstrating the contributions from H_2O as ice, liquid water, OH/ H_2O in anorthite, and internal water on the surface of basaltic glass. We immediately note the band of the anorthite and glass to be weaker and more asymmetric than for ice and water. In spite of the weakness of the 2.8 μm (OH) and 3.1 μm (H_2O) features in lunar spectra, they sometimes are distinctly resolved, e.g., SP3 in Clark (2009). The weak OH spectral signature detected even in equatorial regions is in accordance with the detection of hydrogen at low latitudes with the *Lunar Prospector* neutron spectrometer (Feldman et al., 2000).

Sunshine et al. (2009) found that the depth of the 3 μm band (hydration degree) varied with temperature and revealed a dynamic process with diurnal changes in hydration; these changes occur between local morning and evening, requiring a daytime source of water-group ions. Observations carried out by *Cassini* VIMS (Clark, 2009) confirm the detection of stronger water absorption near the lunar terminator. A constant source of hydrogen with the diurnal cycle could be the solar wind. Unfortunately, it is not so powerful source to provide these variations. The “extended source of water group ions in the inner heliosphere” (Sunshine et al., 2009) is much weaker than the solar proton flux; otherwise, they might produce the “water-group-ions” bands in the solar spectrum due to the

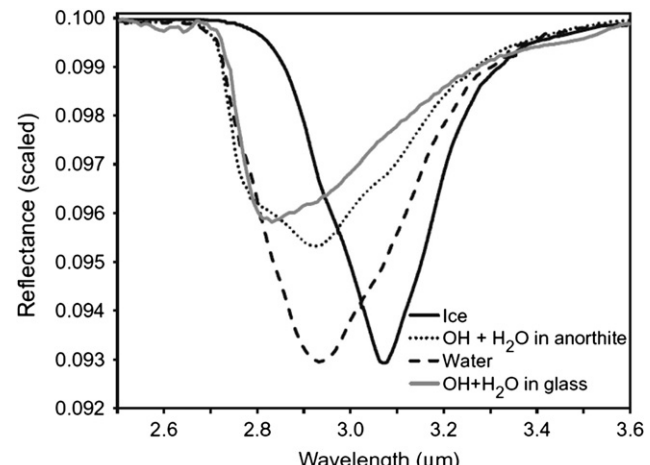


Fig. 30. Contributions from H_2O as ice and water as well as OH/ H_2O in anorthite and internal water on the surface of a basaltic lunar glass analog (Dyar et al., 2010).

absorption at propagation of light from the Sun to the Moon. Thus, the inverse correlation between the hydration and temperature is perhaps the most challenging result obtained for the last decade in lunar studies.

Fig. 31 presents measurements of a north polar region by the *Deep Impact* IR spectrometer on June 9, 2009 showing (a) the *Clementine* mosaic for the region under study, (b) the *Deep Impact* albedo image at $\lambda=1.2\text{ }\mu\text{m}$, (c) the *Deep Impact* temperature distribution, and (d) a map of the strength (relatively extrapolated continuum) of the $2.8\text{ }\mu\text{m}$ hydration feature (Sunshine et al., 2009). The maps (c) and (d) correlate well with each other and confirm that hydration is more strongly controlled by the instantaneous temperature than cumulative insulation (Sunshine et al., 2009). However, while the temperature map clearly shows terminator darkening (c), the apparent albedo image (b) surprisingly demonstrates a trend of terminator brightening, which is hardly possible for the Moon.

Sunshine et al. (2009) have shown that the highlands retain more water than do lunar maria. This is consistent with observation by Pieters et al. (2009a) who have found that the $3\text{ }\mu\text{m}$ feature appears strongest at several fresh feldspathic craters. The latter effect can be related to the correlation between the maturity degree and the depth of the absorption bands: in the neighborhood of fresh craters the regolith is immature (brighter) and the $3\text{ }\mu\text{m}$ band as well as others is conspicuous. Pieters et al. (2009a) have found an important example when an area reliably measured by both the *Chandrayaan-1 M³* and *Lunar Prospector* neutron spectrometers shows controversial results. This is the 113 km diameter crater Goldschmidt ($73.0^{\circ}\text{N}, 3.8^{\circ}\text{W}$). The *M³* data for this crater exhibit a prominent $3\text{ }\mu\text{m}$ band, whereas *Lunar Prospector* data show a distinctly low H abundance, suggesting the hydrated materials observed by *M³* do not occur at significant depths.

The superficial water may come from three sources. One of the sources is primordial (endogenic) water; i.e., it existed since the Moon formed and was trapped in the regolith from the lunar interior. The second source (exogenic) could be comets or H_2O -content meteoroids that struck the Moon. The OH/ H_2O groups could form when solar-wind protons interact with lunar oxygen in the minerals near the Moon's surface; this may perhaps be considered as an exogenic/endogenic source (H atoms come from outside; whereas, oxygen is local).

The availability of the first source has been confirmed recently by Saal et al. (2008) and Hauri et al. (2011). Using an ion microprobe to measure the abundance of OH[−] anions Saal et al. (2008) have detected 20–45 ppm OH in the interior of *Apollo-15* green and *Apollo-17* orange volcanic glasses mainly in the form of spherules; the measurements showed a higher concentration of

OH in the center of the spherules and a decrease toward the surface. Hauri et al. (2011) found H_2O inclusions that allowed the team to measure the pre-eruption concentration of water in the magma and to estimate the amount of water in the Moon's interior. The green and orange volcanic glasses are believed to be the most primitive materials from the lunar mantle in the *Apollo* and *Luna* sample collections. The compounds OH[−] and H_2O may occur within minerals due to primary crystallization (structural water). Unfortunately, we cannot consider this source as the primary, since the upper regolith layer, containing about 70% of agglutinate glasses, has been many times undergone melting and heating. This heating was noticeably more than from solar radiation ($T_0 \approx 394\text{ K}$). After such a tempering, the remaining primordial water should not be sensitive to the observed latitude trend of the $3\text{ }\mu\text{m}$ band. Careful infrared spectroscopic examinations of agglutinate glasses did not detect the presence of water at all (Taylor et al., 1995).

According to estimates by Arnold (1979), about 0.5 kg/m^2 of water has been delivered to the lunar surface by comets over the past 2 billion years (totaling $\sim 2 \times 10^{13}\text{ kg}$). Later this estimate increased to a value of 10^{15} kg (Ong et al., 2010). Actually, the values are unreliable, as even one rather large sized comet may considerably change these estimations. Such a comet source is believed to be applied to the formation of bulk (Arnold, 1979; Klumov and Berezhnoi, 2002; Ong et al., 2010) as well as superficial (Clark, 2009; Pieters et al., 2009a) water layers.

Bulk water ice may occur in permanently shadowed areas at the poles that are characterized by their low temperature, absence of direct solar wind and UV radiation. Local ice deposits into these areas can be formed at a small number of powerful cometary impacts randomly distributed nearly the lunar poles. By small secondary impacts the ice can be buried and mixed with the regolith. Because of impact vaporization, a small portion of the comet water (amounting to several % of the total) can be retained in the lunar surface; nevertheless, it may hypothetically be a source of hydrogen signals from the neutron spectrometers of *Lunar Prospector* and *LRO* in some permanently shadowed areas. The measurements carried out by the *LRO* neutron spectrometer LEND (Mitrofanov et al., 2010; Sanin et al., 2010) show that the intensity of the signal does not always correlate with the distribution of permanently shadowed areas. This is consistent with the random distribution of cometary impacts near the lunar poles. The *LRO* Diviner temperature map (Elphic et al., 2010) also shows a poor correlation with the hydrogen distribution, e.g., the crater Shackleton, being an excellent cold trap because it is situated near the south pole, shows a low hydrogen signal from the *LRO* LEND, see also Haruyama et al. (2008).

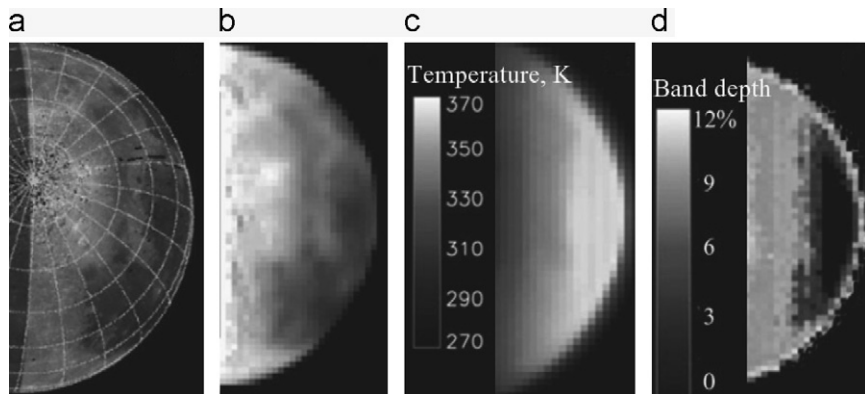


Fig. 31. Observations over the North pole by *Deep Impact* on 9 June, 2009 with resolution $\sim 60\text{ km/pixel}$: (a) *Clementine* basemap of the observed area shown for comparison, (b) $1.2\text{ }\mu\text{m}$ *Deep Impact* albedo image, (c) temperature map derived from measurements at $\lambda > 4\text{ }\mu\text{m}$, and (d) map of the strength of the continuum-removed $2.8\text{ }\mu\text{m}$ hydration feature.

Another hypothesis for the formation of water ice and volatile stores is the migration of OH⁻ and H₂O compounds toward the poles when comet impacts occurred beyond the permanently shadowed areas (Arnold, 1979; Klumov and Berezhnoi, 2002; Crider and Vondrak, 2002; Ong et al., 2010). Different estimates have shown that if the deposited compounds are not buried rapidly, then erosion caused by sputtering, Lyman- α radiation, and meteorite bombardment can quickly remove water ice deposits, even in permanently shadowed areas (Lanzerotti et al., 1981; Morgan and Shemansky, 1991; Killen et al., 1997). However, the invincibility of the mechanism is that one always may say the infalling comets were so large that any objections in Lanzerotti et al. (1981), Morgan and Shemansky (1991), and Killen et al. (1997) are weak to discredit the hypothesis.

For generation of superficial water on sunlit areas, the described migration-absorption mechanism seems to be not effective, though this is insistently studied (e.g., Farrell et al., 2011). Actually, physical absorption on the regolith particle surface, depending on surface micro-roughness and micro-porosity, is characterized by a rather low energy of activation of ~ 0.35 eV. This energy is even smaller than the interaction energy between water molecules, which results in molecular coalescence into clusters (Dyar et al., 2010). A monolayer of water/ion would not tend to migrate into the grains and, therefore, would remain weakly bound with the particle surface. Chemical absorption energy is higher than 0.35 eV depending on surface roughness on molecular scales. This type of absorption is discussed below, when we analyze the solar-wind mechanism of lunar water formation.

Owing to low activation energy, the concentration of H₂O and OH⁻ compounds depends dramatically on the surface temperature. At $T \approx 300$ K no OH/H₂O compounds retained on the lunar surface with van der Waals forces may survive. Moreover, Andersson and van Dishoeck (2008) computed the probability for H₂O desorption per absorbed UV photon to be up to 1% in the top three monolayers. This may theoretically desorb about 30 g of H₂O per square meter per year at a UV solar flux of 3×10^{11} photons/cm² s, giving no chance for the molecular migration mechanism with physical absorption to occur.

Thus we ought to consider a third mechanism, when protons of the solar wind (H atoms) striking the regolith, bind with atoms of oxygen, and give rise to H₂O and OH that are strongly connected with the bombarded surface. This is a very powerful and effective mechanism. At a flux of 3.8×10^8 protons/cm² s, the cumulative mass of solar protons on a square meter during the two last billions of years is approximately 400 kg. Of course, the lunar surface cannot accept such an amount of protons, because of the saturation effect.

The protons produce radiation damage in the superficial zones of regolith particles, resulting in defects that may be traps for other implanted solar-wind ions. The trapping by the radiation defects is much stronger than just physical trapping by a surface. This enables the implanted gases to accumulate considerably in the regolith. An important consequence of the induced traps is broken chemical bonds of oxygen atoms; the bonds tend to be saturated by the implanted hydrogen atoms (Starukhina and Shkuratov, 2000). The formation of the implantation-induced OH-bonds was observed in experiments with oxides and silicates (Roth, 1983; Zeller et al., 1966; Lord, 1968). Later experiments have confirmed the results concerning OH and shown the possibility of H₂O formation (e.g., McCord et al., 2011; Managadze et al., in press).

The saturating concentration of hydrogen trapped by the surface of a regolith particle is estimated (Starukhina and Shkuratov, 2000) to be $\sim 10^{17}$ cm⁻², the penetration depth being < 100 nm. Thus, the layer thickness of trapped hydrogen is much more than that of a water monolayer (~ 0.2 nm). The saturation time of the lunar

particle surface exposed to the solar protons is about 100 years, i.e., much shorter than the solar-wind exposure time for regolith particles. In permanently shaded polar areas, the implanted hydrogen may be supplied from the Earth magnetotail; in this case, the saturation time is 1000 years (Starukhina and Shkuratov, 2000). Even protons diffusively reflected from areas exposed directly to the solar wind to permanently shaded regions are a fairly powerful source of OH/H₂O compounds, as “proton albedo” of the lunar surface is about 0.1–1.0% (Saito et al., 2008). Depending on regolith particle roughness, the mass fraction of implanted hydrogen may vary considerably. In particular, if the specific surface area of lunar regolith is ~ 5000 cm²/g (Cadenhead et al., 1977) and lossless mixing of saturated particles in the upper layer of 10 cm thickness is possible, then the mass fraction observed with the *Lunar Prospector* neutron spectrometer at lunar poles of 200 ppm (Lawrence et al., 2005) can be easily achieved.

We also could suggest a new mechanism to deliver OH/H₂O compounds to cold traps in the polar permanently shadowed regions. This is related to the electrostatically levitated dust that moves as the terminator shifts because of lunar rotation. Observations of a lunar-horizon glow by Surveyors, Lunokhod-2, and Apollo crews and detection of dust-particle impacts by the Apollo-17 Lunar Ejecta and Meteoroid Experiment have been explained as the result of submicron/micron-sized charged particles lifting off the surface (e.g., Criswell, 1972; McCoy and Criswell, 1974; McCoy, 1976; Stubbs et al., 2006). The solar UV radiation causes electron photoemission from the surface of lunar particles, so it develops a surface charge (positive) and, hence, an electric field near the surface. Regolith dust particles surmounting the cohesion forces can be injected into space with these electrostatic forces. Depending on particle sizes they may move different distances along ballistic trajectories. They also may more-or-less stably levitate above the surface; however, they then deposit preferentially onto areas with opposite electric charge. During lunar nights, the dark surface of the Moon is charged negatively; permanently shadowed areas are always charged negatively. Thus, these areas may effectively accumulate the lunar dust.

Areas near the lunar poles always are at the terminator; hence, the process of dust transportation here is most intensive. Dust particles of submicron size should be saturated by implanted hydrogen. They may be considered as OH/H₂O “ice” introduced into the silicate matrix, as the quantity of the OH/H₂O compounds may reach 10 wt% for anorthosites particles ~ 0.1 μ m. The electrostatic churning rate is estimated to be 10^{-11} g/cm² s or 1 ton/km² per a year (Criswell, 1972; McCoy and Criswell, 1974; McCoy, 1976). Of course, not all churned dust will be transported to the permanently shadowed areas that can be located not necessarily near the poles. However, this transportation mechanism seems to be powerful. Depending on the surface topography in and around cold traps, this mechanism may enrich the upper ~ 10 cm of the regolith layers in the traps with dust particles.

The dust material enriched with OH/H₂O compounds may be accumulated in lunar surface holes that were found recently with Kaguya and LRO cameras (Haruyama et al., 2011) and in small permanently shadowed areas that may occur not only at the poles, but at intermediate latitudes; the hierarchical structure of the lunar mesoscale topography allows the existence of a huge amount of such areas (cold traps) with the characteristic size on the order of 1 m (Stankevich et al., 2001; Petrov et al., 2003).

Thus, the proton implantation mechanism can be effective not only for the production of superficial water, but probably for bulk water formation as well. A significant advantage of the mechanism is not only the powerful source of hydrogen, but that OH/H₂O compounds introduced into the particle material are fairly stable to the UV and solar-wind sputtering and may be kept in the regolith particles at temperature up to 600 K. Experiments have

shown the peak of hydrogen lose to be near 800 K (Gibson and Johnson, 1971). This might explain why the neutron and optical spectrometers detected hydrogen signatures at regions near the lunar equator, where “usual” water ice should not be at all.

The puzzling inverse correlation between the hydration of lunar regolith and insolation (Sunshine et al., 2009; Clark, 2009) may manifest unknown processes on the lunar surface. Heating and UV irradiation can theoretically be responsible for it. The heating increases nonharmonic vibrations of atoms. The increasing random motions of neighboring ions can impede stretching vibrations of structural OH and, hence, could weaken the band. The 3 μm band should be sensitive to heating as well as charge transfer and crystal field bands. However, this perhaps is too small to produce the Sunshine–Clark effect. The UV radiation also seems to be potentially important to break bonds of structural OH and H₂O. The penetration depth of ultraviolet photons with λ from the range of 100–200 nm is on the order of λ ; that is close to the thickness of the superficial layer where OH/H₂O compounds may be induced by the solar-wind. Unfortunately, quantitative estimations of this mechanism are not reliable, because of many influencing factors.

It is worth noting possible differences in the behavior of spectral bands caused by absorbers distributed in the particle volume and surface layer. For instance, at an increase of the particle size, the absorption coefficient (see Section 4.2) increases for the volume distribution, but remains the same if absorbers are distributed in the surface layer of a constant thickness. This effect can manifest itself for immature soils in intensifying the pyroxene bands and simultaneous decreasing the 3 μm signature.

How much H₂O and OH compounds should be in the regolith to reliably measure the 3 μm spectral feature? Fig. 32 shows two laboratory spectra of powdered basalt, which correspond to hydrated and dehydrated samples; the latter was obtained with dehydration of adsorbed water upon heating in a vacuum (Clark, 2009). Approximately 2500 ppm water was removed through dehydration in a vacuum at approximately 500 K for 16 h. At the dehydration, the 9% depth of the 3 μm band defined relative to a linearly extrapolated continuum (albedo near 18%) was significantly weakened.

4.5. Chemical prognoses

A colorimetric image of the Moon is the ratio of coregistered albedo images acquired at different wavelengths. Initially, a

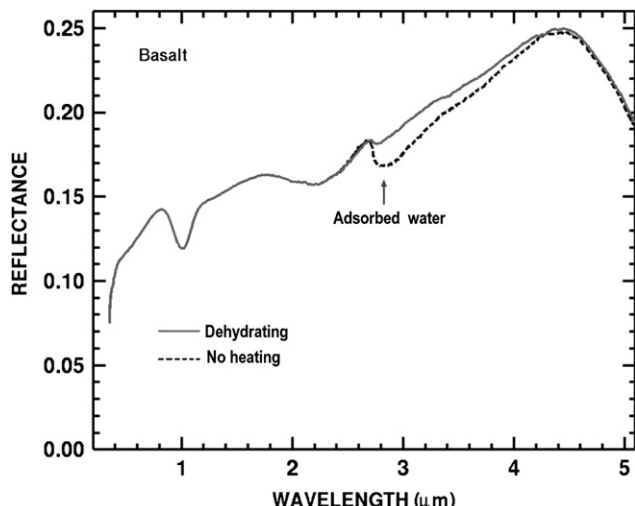


Fig. 32. Laboratory spectra of hydrated and dehydrated (heating in a vacuum at 500 K during 16 h) basalt samples.
Data are adapted from Clark (2009).

photographic summation of equicontrast positive and negative corresponding to different wavelengths (e.g., 0.6 and 0.4 μm) was produced (Whitaker, 1972). One of the first color maps of the lunar visible hemisphere was constructed with this method by Evsyukov (1973b). Later lunar colorimetry was carried out with electronic equipment (e.g., McCord et al., 1976; Davies et al., 1979; Johnson et al., 1991a,b; Hawke et al., 1990).

The main task of lunar color-ratio imaging is composition prognoses for the regolith layer. The possibility of such prognoses was proved convincingly by Charette et al. (1974), who found a correlation between the color ratio C(0.41/0.56 μm) and the TiO₂ content using laboratory measurements of mature mare soils. Later, similar dependencies were used to map the content over the lunar maria of the nearside (Pieters, 1978; Johnson et al., 1991b) and even the full disk (Shkuratov et al., 1999c). However, these algorithms are still very approximate. First, the influence of maturity degree should be taken into account, which is not a trivial problem. Second, it seems that the accurate determination of TiO₂ abundances through color ratios using only one regression is not possible at all. Different mare basalts may have different regression parameters; Gillis et al. (2003) have found at least two regressions: one fits the majority of Apollo data, and the second is a fit to the *Apollo 11*, *Luna 16*, and *Luna 24* data.

Recently noticeable progress has been achieved using data acquired by the *HST* (Robinson et al., 2007). The data indicate a strong correlation of C(0.502/0.250 μm) with TiO₂ content determined from returned samples at the *Apollo 17* landing site, and a little correlation with the maturity of lunar soils. This new finding implies that UV-vis observations may lead to an improved method of remotely mapping TiO₂-bearing materials (ilmenite) across the lunar surface and enable more refined studies of the lunar crust composition and surface volcanism (Robinson et al., 2007). Recently, the ratio C(320/415 nm) computed with *LRO* WAC images was used to map the TiO₂ content (Robinson et al., 2011). For calibration the measurements of the TiO₂ distribution with *Lunar Prospector* (Prettyman et al., 2006) and lunar sample data from the *Apollo* and *Luna* landing sites were used. The map, however, has drawbacks of previous maps. For instance, the optical estimations of TiO₂ content for Mare Crisium is much higher than measured with the *Lunar Prospector* gamma-ray spectrometer (Prettyman et al., 2006).

Lucey et al. (1995, 1998, 2000a,b) developed the chemical prognosis problem revealing some regularity in the position of the samples of different maturity and composition on the lunar diagram A(0.75 μm)–C(0.95/0.75 μm). It turned out that the samples with close iron content, but different maturity, form sequences that are oriented approximately in the direction of a certain singular point on the diagram, with the distance from this point characterizing the degree of maturity of the samples: the smaller the distance, the higher the maturity. Fig. 33 illustrates this and also shows an angular trend related to the FeO content. Lucey et al. (1995, 1998, 2000a) suggested a transformation to new polar coordinates with the center at the “overmature” point on the plane A(0.75 μm)–C(0.95/0.75 μm). In this case, the polar angle appears to be related to the iron content, while the radial coordinate correlates with the maturity of the soil samples. A similar approach for the determination of the regolith maturity and the content of titanium dioxide was performed by analyzing the diagram A(0.750 μm)–C(0.750/0.415 μm) (Blewett et al., 1997; Lucey et al., 2000a). It is interesting to note, however, that the distributions of the maturity degree obtained with the diagrams A(0.75 μm)–C(0.95/0.75 μm) and A(0.750 μm)–C(0.750/0.415 μm) are rather different; in the latter case the residual titanium component manifests itself more prominently than might be expected.

To estimate the distributions of FeO and TiO₂ content and the so-called parameter of optical maturity OMAT, the Clementine

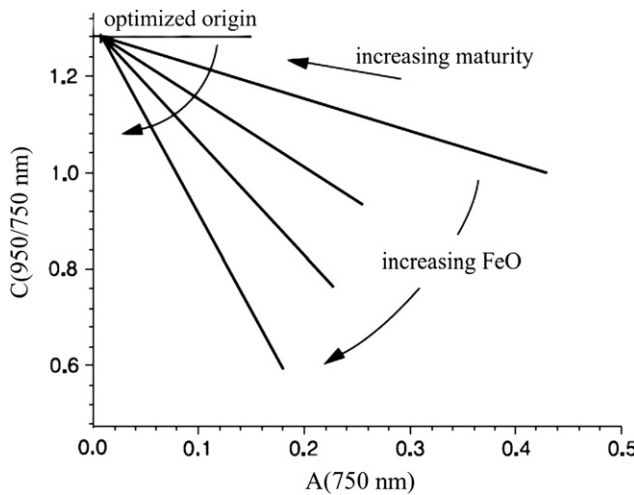


Fig. 33. Scheme explaining the Lucey method of determination of chemical composition.

mosaics are used. To produce calibration dependencies, *Apollo* samples were exploited. For these samples the chemical and maturity determinations were used, and their albedo values were found at the sampling sites with *Clementine* images of 100 m resolution. This allows the following equations:

$$\text{FeO}(\%) = -17.43 \left\{ \arctan \left[\frac{A(950\text{nm})/A(750\text{nm}) - y}{A(750\text{nm}) - x} \right] \right\} - 7.56, \quad (45)$$

$$\text{TiO}_2(\%) = 3.71 \left\{ \arctan \left[\frac{A(415\text{nm})/A(750\text{nm}) - z}{A(750\text{nm})} \right] \right\}^{5.98}, \quad (46)$$

where $A(\lambda)$ is albedo (%), $x=0.08$, $y=1.19$, and $z=0.42$. Formula for the parameter OMAT was obtained using the diagram $A(750\text{ nm}) - C(950/750\text{ nm})$

$$\text{OMAT} = \sqrt{(A(750\text{nm}) - x)^2 + \left(\frac{A(950\text{nm})}{A(750\text{nm})} - y \right)^2}, \quad (47)$$

It should be noted that theoretical modeling and laboratory measurements do not show the existence of the overmature point on the diagrams; rather there is a caustic where the sequences of the same content, FeO or TiO₂, accumulate (Starukhina and Shkuratov, 2001). Thus the Lucey approach allows estimates of FeO and TiO₂ only in a first approximation.

Fig. 34 presents maps of FeO and TiO₂ distributions obtained using *Clementine* mosaics and Eqs. (45) and (46), which are shown on panels (a) and (b), respectively. Distribution of the parameter OMAT is obtained with Eq. (47); it is shown in Fig. 38a and discussed below. The FeO map resembles an albedo distribution in negative, which is natural as iron is the main lunar surface chromophore. However, unlike the albedo distribution, the contrast of young highland craters is suppressed. This is considered as evidence of the algorithm accuracy, since the composition of crater-deposited material should be close to that of the undisturbed areas. The TiO₂ distribution looks like the color ratio $C(0.750/0.415\text{ }\mu\text{m})$ image, which is in agreement with earlier determinations (e.g., Johnson et al., 1991b). The distribution reveals values of TiO₂ content up to 18%, e.g., in Mare Tranquillitatis, which seems to be excessive. The OMAT map resembles the color ratio $C(0.95/0.75\text{ }\mu\text{m})$ images. Young craters and their ray systems show up on the map, which agrees with the low maturity degree of the regolith in these areas.

A development of the Lucey approach was suggested in Shkuratov et al. (1999b) to perform a self-consistent analysis of a 3D diagram incorporating FeO, TiO₂, and maturity degree.

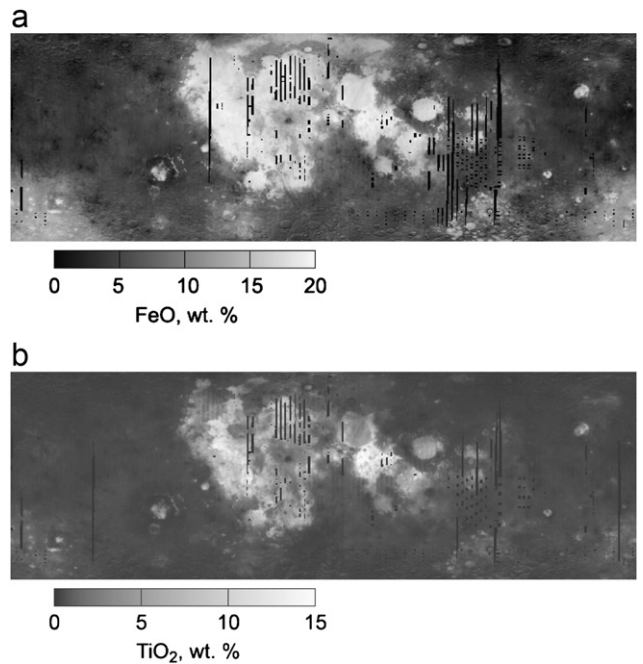


Fig. 34. Application of the Lucey method using *Clementine* mosaics: (a) FeO distribution obtained with Eq. (45) and (b) TiO₂ distribution, Eq. (46). Vertical strips in the image correspond to the regions that were not covered by the imaging. Projection is simple cylindrical; the latitude range is $\pm 77^\circ$.

Telescope albedo images acquired at wavelengths 0.42, 0.65, 0.75, and 0.95 μm were used for the determination of the absorption coefficients $\tau(\lambda)$ using the model by Shkuratov et al. (1999c). The absorption coefficients characterize the lunar surface material rather than the regolith (discrete) medium. The 3D diagram used the following axes: $\tau(0.75\text{ }\mu\text{m})$, $\tau(0.65\text{ }\mu\text{m})/\tau(0.42\text{ }\mu\text{m})$, and $\tau(0.95\text{ }\mu\text{m})/\tau(0.75\text{ }\mu\text{m})$. In the 3D space of the above-mentioned parameters a new basis was introduced in which one can reliably separate the influence of chemical composition and regolith maturity on optical characteristics. The new basis was chosen to minimize the dispersion of points in the optical-chemical dependencies constructed using the averaged data for the landing sites of the spacecraft of *Surveyor*, *Luna*, and *Apollo* series. Such a method provides an alternative to the two OMAT parameters determined from the $A(750\text{ nm}) - C(950/750\text{ nm})$ and $A(750\text{ nm}) - C(750/415\text{ nm})$ diagrams using the Lucey method. The line of investigation by means of lunar colorimetry described here is in the process of active development. An improvement of Lucey's technique has been made with the combination of *Clementine* UVVis and NIR data sets to better evaluate the spectral alteration effect (LeMouelic et al., 2000).

An alternative technique (Shkuratov et al., 2003b) was developed in connection with the lunar ESA *Smart-1* mission. One of the scientific objectives of the mission was lunar colorimetric imaging at 100 m resolution using the AMIE camera (Pinet et al., 2005). Because of calibration problems this imagery is very problematic, but the suggested technique is universal and may be applied to any lunar spectral data. Shkuratov et al. (2003b) have used *Clementine* UVVis mosaics and detailed laboratory compositional and spectral data on lunar soils. These data were produced by the Lunar Soil Characterization Consortium (LSCC) (Taylor et al., 1999, 2001); they include regolith samples selected to be representative of various lunar basalt compositions having different soil maturity. The coordinated compositional and spectral measurements of the soils were obtained for four subsamples with controlled particle size: <45, <10, 10–20, and 20–45 μm . Overall, nearly 50 subsamples were involved in the analysis.

The main purpose of the statistical approach is to find relationships that provide the highest correlation coefficients between different linear combinations of optical parameters, on one hand, and chemical/mineral composition, maturity degree, and size of regolith particles, on the other hand (Shkuratov et al., 2003b). A very important point is that *Clementine* and LSCC spectra are represented in the same photometric system. This means that all laboratory calibration dependencies can be automatically applied to the Moon. In this approach, first of all, direct and indirect links between the combined spectral parameters of soils and their compositional characteristics have been evaluated through a statistical analysis of the variance across each type of measurement using principal component analysis (Pieters et al., 2002). Then, it was shown that in a first approximation, the following equation is suitable for the analysis:

$$\log X = aA_R + bC_{BR} + cC_{IR1} + hC_{IR2} + fC_{IR3} + eK + g, \quad (48)$$

where X is a geochemical or physical parameter (e.g., FeO, TiO₂, in weight %, or particle size in μm), $A_R = A(750 \text{ nm})$, in %; $C_{BR} = C(415/750 \text{ nm})$, $C_{IR1} = C(900/750 \text{ nm})$, $C_{IR2} = C(950/750 \text{ nm})$, $C_{IR3} = C(1000/750 \text{ nm})$, $K = C(1000/900 \text{ nm})/C(900/750 \text{ nm})$, and the coefficients a , b , c , h , f , e , and g should provide the maximal correlation coefficients k in correlations with the LSCC ground-truth data. While the choice of the color indices C_{BR} , C_{IR1} , and C_{IR2} is quite rational, the choice of the parameter of spectral bend K is not so evident. In a first approximation it characterizes the depth of the first pyroxene band. Mapping this parameter with *Clementine* data shows that it is useful for geologic studies of the lunar surface, in particular, to find regions of nonmare volcanism on the Moon (Raitala et al., 1999). In order to avoid negative values of the predicted parameters, we used the logarithm of these parameters in Eq. (48).

Using this approach the abundance of TiO₂ and FeO, maturity degree (I_s/FeO), and a characteristic size parameter of particles were mapped (Shkuratov et al., 2003b). Comparison of the TiO₂ and FeO abundance maps with distributions obtained by Lucey et al. (2000a) shows high correlation. An interesting part of this analysis is the map of the particle size shown in Fig. 35b. Such a map is feasible as the LSCC data include spectra for particle size separates. Relatively coarse particles appear to be characteristic of rims and ejecta of fresh craters material, which is quite reasonable. Small particles are representative of highlands: plagioclase, which dominates the highland soil and rocks, can be crushed by micrometeorite impacts more efficiently than mafic minerals occurring in mare materials (e.g., Engelhardt et al., 1976). Fig. 35b shows almost no traces of the Reiner- γ formation that is excellently seen in albedo (Fig. 35a), suggesting that the characteristic particle size of the formation would be the same as for surrounding areas. This is a surprising result, as this formation has regolith of low maturity, which is normally characteristic of coarsely grained regolith (Morris, 1980). This result is in contrast with the studies suggesting the formation is a modification of the upper layer of the regolith with the removal of the finest fraction of the soil and its redistribution in the vicinity (e.g., Bell and Hawke, 1981); meanwhile this is consistent with the mechanism of a gentle modification by a meteoroid swarm considered in Shkuratov et al. (2010).

As a development of the statistical technique described, an additional method was proposed (Shkuratov et al., 2005a); the same approach later was suggested to map TiO₂ abundance (Robinson et al., 2011). The gist of the technique is a certain “interpolation” of available *Lunar Prospector* gamma-ray spectrometer (GRS) data of low spatial resolution, using *Clementine* UVVis (Shkuratov et al., 2005a) or *LRO* WAC (Robinson et al., 2011) spectral reflectance images of higher resolution. The main idea is to use low resolution GRS measurements as a ground truth to establish relationships linking optical data and geochemical information, thereby maximizing the respective correlation coefficients.

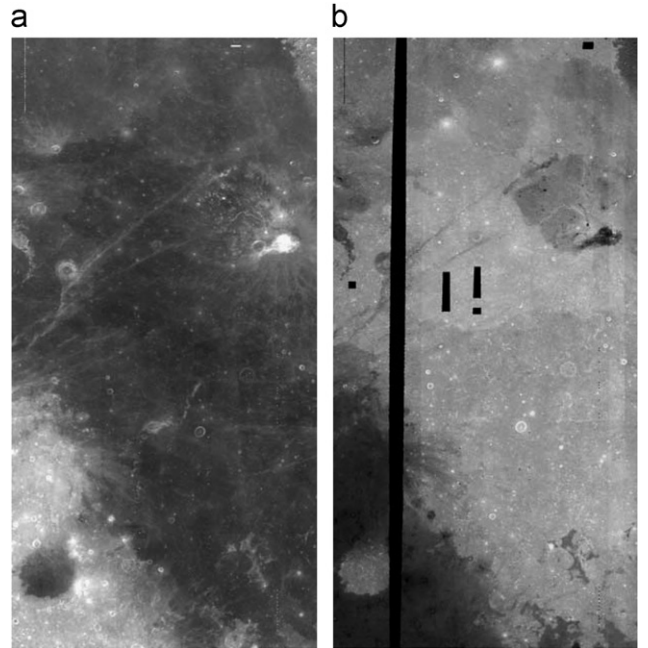


Fig. 35. (a) Albedo image and (b) distribution of the average particle size parameter for the northern portion of Oceanus Procellarum (Shkuratov et al., 2003b). Because of uncertainties in the determination of sample particle size and their granulometric difference from natural lunar soils, this map has no parameter scale. Dark tones correspond to smaller particles. Vertical strips in the image correspond to the regions that were not covered by the *Clementine* imaging. Projection is simple cylindrical.

The relationships obtained with Eq. (48) between *Clementine* UVVis and *Lunar Prospector* GRS data we used to derive elemental abundance maps with significantly improved spatial resolution corresponding to the resolution of *Clementine* data. The main limitation of the technique is its dependence on how well the abundance of the elements correlates with the *Clementine* UVVis data. The Fe and Ti distributions resemble qualitatively the maps obtained with the technique by Lucey et al. (2000a). As an illustration of the suggested technique, the initial map of oxygen and calculated map with higher resolution (pixel size $15 \times 15 \text{ km}^2$) are presented in Fig. 36 (Shkuratov et al., 2005a). Oxygen is not chromophore, but its abundance correlates with Fe and Ti, providing a rather high correlation coefficient 0.75 with optical data. The oxygen map appears to be informative, as it demonstrates composition anomalies, e.g., in the crater Tycho. To calculate the maps of the elements Fe, Ti, Ca, O, and Mg using *Clementine* UVVis data and the *Lunar Prospector* GRS data, the coefficients of Eq. (48) shown in Table 4 can be used. Note that there is an attempt to incorporate in this analysis both the UVVis and NIR data (Wöhler et al., 2009), but the resulting maps look very similar to those published in Shkuratov et al. (2005a).

It should be emphasized that the choice of the optical parameters and relationships connecting spectral and chemical parameters are not unique, and therefore the described technique also is non-unique. One may barely anticipate that different choices, if they are not too artificial and exotic, will give similar results (Shkuratov et al., 2003b). This is a general weakness of such formal empirical approaches. Nevertheless, there is a technique suggesting a maximally effective way to analyze relationships between bands-restricted spectral data and chemical/mineral composition. This is the technique of Artificial Neural Networks (ANNs) (Korokhin et al., 2008). A very useful feature of the technique is that it is not necessary to specify the formulae for finding the statistical relationships, examples of which are Eqs. (45)–(48). A TiO₂ map obtained with the ANNs method using

Clementine UVVis mosaics and LSCC data is presented in Korokhin et al. (2008). This resembles the map calculated with the Lucey technique (Fig. 34b), but its parameter scale is different: while the upper values of Lucey's map are near 18%, which seems excessive, the highest ANNs contents are about 10%, which seems more consistent with the chemical analyses of samples from the *Apollo* and *Luna* collections. In the development of the statistical approach to map the elements Fe and Ti, a prospective method seems to be using the partial least squares method (Li, 2008a,b; Li and Lucey, 2009).

4.6. Prognoses of mineral abundance and maturity degree

Plagioclase, pyroxene, and olivine are the main rock-forming minerals of the lunar surface; plagioclase prevails in highlands, while pyroxene and olivine predominate in mare regions. Mapping of the regional abundance of these minerals and characteristics of their composition is one of the most important objectives of the remote sensing of the Moon. Only the first steps have been made in the development of this approach. These steps have been based on Moon imagery and on the results of spectral and mineral studies of lunar soil samples.

There are several attempts of lunar mineral mapping. To map pyroxenes, olivine, and plagioclase, Lucey (2004) used the Hapke (1993) model that was applied to 400,000 *Clementine* UVVis spectra and laboratory spectra of different minerals. Lucey (2004) has found that plagioclase inversely correlates with iron, while clinopyroxene reveals a positive correlation. The distribution of olivine in the highlands is ubiquitous, but as low as a few

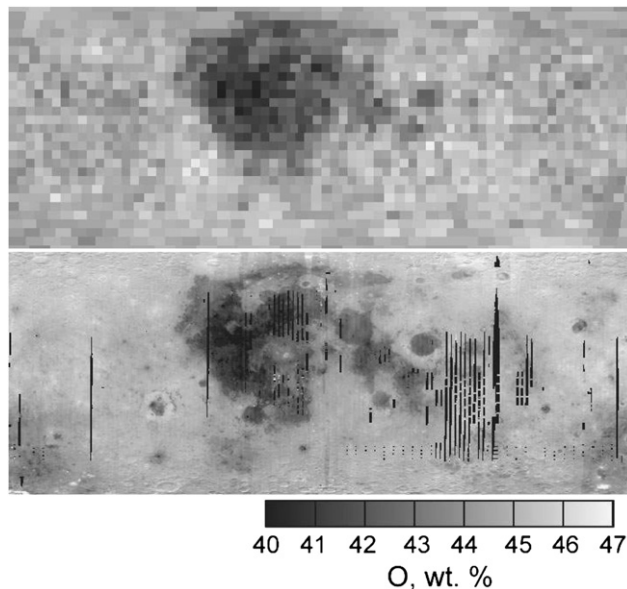


Fig. 36. Oxygen distribution measured with *Lunar Prospector* (upper panel) and the same map constructed using *Clementine* mosaics with Eq. (48) (lower panel) (Shkuratov et al., 2005a).

Table 4

Coefficients of Eq. (48) found with the technique using *Clementine* UVVIS and the *Lunar Prospector* GRS data; k is the correlation coefficient.

	a	b	c	d	e	f	g	k
Fe	-0.039	1.354	-38.321	0.314	16.251	-18.2	40.819	0.96
Ti	-0.090	8.303	-95.841	0.72	43.169	-44.783	93.31	0.86
O	0.0015	-0.069	7.910	0.148	-3.676	4.217	-6.966	0.75
Al	0.020	-1.029	34.5	-0.174	-15.217	17.34	-35.26	0.76
Ca	0.020	-1.581	32.747	-1.425	-14.613	14.369	-29.523	0.67
Mg	-0.031	1.217	-25.209	2.161	10.101	-5.940	19.47	0.73

percent. The abundance of orthopyroxene is generally low, excepting several regions, e.g., areas near and within the South Pole-Aitken basin. Mare samples with elevated abundances of orthopyroxene have been found in some mare and cryptomare deposits distant from the sample return sites. Yan et al. (2010) developed the approach using the UVVis as well as NIR data, suggesting an ilmenite map.

Pieters et al. (2006) and Shkuratov et al. (2005b) have used the mineral/spectral characterizations of the soil samples studied by LSCC (near 70 samples) to examine correlations between the regolith spectral parameters and the mineral contents. Such correlations can be used for calibrating in predicted mineral abundance throughout the lunar surface with the multispectral UVVis imagery from the *Clementine* spacecraft. Using a simple linear combination of the spectral albedo values in four wavelengths

$$\log X = a_m A(415 \text{ nm}) + b_m A(750 \text{ nm}) + c_m A(900 \text{ nm}) + d_m A(1000 \text{ nm}) + e_m, \quad (49)$$

the maximal correlation coefficients between the measured and predicted contents of the main minerals are found by varying the constants a_m , b_m , c_m , d_m , and e_m (albedo is expressed in %) (Shkuratov et al., 2005b). The correlation coefficients and values of a_m , b_m , c_m , d_m , and e_m are given in Table 5. This table shows that plagioclase and clinopyroxene contents can be predicted reliably. Fig. 37 shows that maps of plagioclase and clinopyroxene correlate inversely and directly, respectively, with iron, as was found by Lucey (2004). Abundance of the minerals relates to bright (young) craters and their ray systems, as the plagioclase and clinopyroxene are crystalline components of regolith, and their amount should closely correlate with the exposure age of the lunar surface. The South Pole-Aitken basin shows a high abundance of clinopyroxene and low abundance of plagioclase. Pieters et al. (2006) produced maps of different types of pyroxene, e.g., orthopyroxene, however, these determinations are less reliable.

The amount of minerals present in the crystalline component is strongly controlled by the maturity of lunar soils. There are different definitions of this characteristic (e.g., Lucey et al., 2000b). For instance, we have mentioned the OMAT parameter that may be calculated from Eq. (47) (see Fig. 38a). Another one is agglutinate content. Agglutinates are the most altered portion of lunar surface material. Agglutinate particles are debris of rocks and minerals consolidated by glasses produced by micrometeoritic impacts. Mature lunar soil contains of about 70% of agglutinates (McKay et al., 1991); this is several times higher than in

Table 5

Parameters in Eq. (49) and the correlation coefficients between the measured and predicted values; k is the correlation coefficient.

	a_m	b_m	c_m	d_m	e_m	k
CPx	-0.129	0.244	0.147	-0.321	1.270	0.93
PI	0.114	-0.126	-0.021	0.093	1.064	0.93
Agglutinates	-0.057	0.038	-0.078	0.065	1.782	0.85
I_s/FeO	0.006	-0.224	0.138	0.060	1.944	0.88

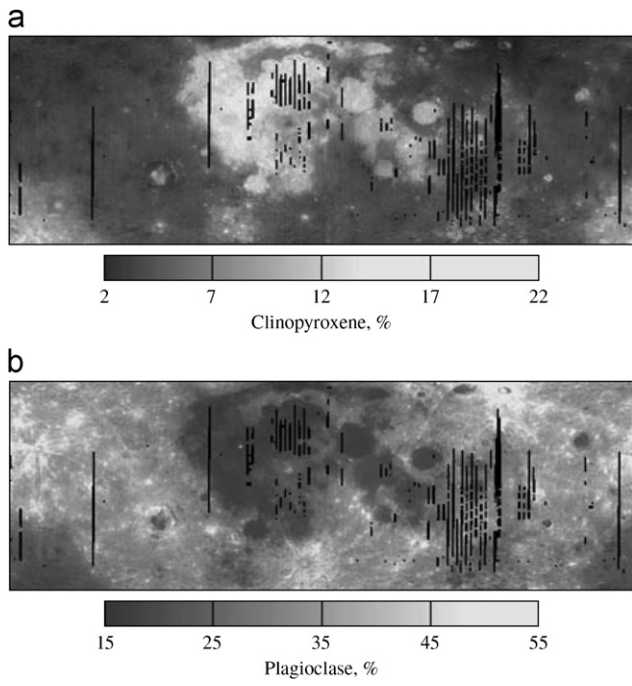


Fig. 37. (a) Pyroxene and (b) plagioclase distributions calculated with Eq. (49).

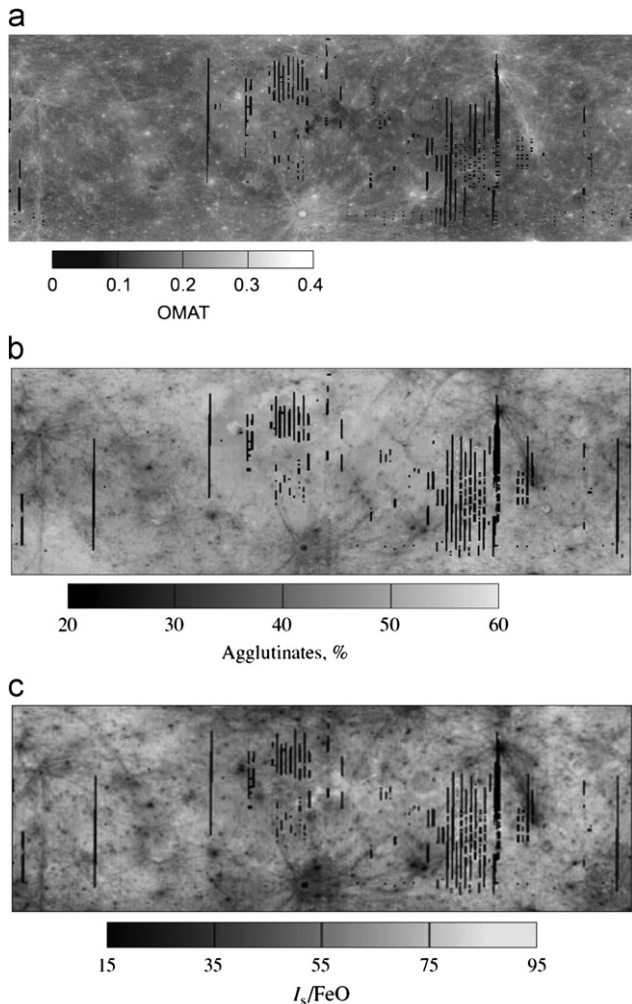


Fig. 38. Maps of the parameters related to maturity degree: (a) parameter OMAT calculated with Eq. (47); (b) agglutinate content, Eq. (49); and (c) parameter I_s/FeO , Eq. (49).

immature soil. Eq. (49) was exploited to map the content of lunar agglutinates (Shkuratov et al., 2007a). In Table 5 we give the constants a_m , b_m , c_m , d_m , e_m and the correlation coefficient for the predicted and measured agglutinate abundances. Although this coefficient is rather high ($k=0.85$), it is lower than that for the CPx and Pl content. Shown in Fig. 38b is an agglutinate abundance map. This inversely correlates with the OMAT parameter map presented in Fig. 38a. Weak variations of the agglutinate abundance are observed in the lunar maria. An exception is the Plateau Aristarchus that is a pyroclastic area.

Although the composition of agglutinate particles mostly corresponds to that of the local material, exceptions are frequently observed. It is important to study the causes of these exceptions because they can elucidate the evolution of the lunar surface and provide information about the efficiency of the global material transport on this surface (Pieters and Taylor, 2003). Analysis of lunar samples showed that relative to the crystalline fraction the mare agglutinates are enriched in Al and depleted of Fe, Ti, and Cr, while the highland agglutinates show the opposite characteristic, i.e., depleted Al and enriched Fe, Ti, and Cr (Pieters and Taylor, 2003). Shkuratov et al. (2007a) extended this mineral prognosis to the whole lunar surface using Eq. (49).

The most important characteristic of maturity degree of lunar soils is considered to be the parameter I_s/FeO (Housley et al., 1973; Morris, 1980). This characteristic is the ratio of npFe⁰ content (I_s) determined by measurements of ferromagnetic resonance to bulk abundance of iron oxide in a sample. As has been noted, npFe⁰ inclusions may be formed by a few processes such as in-melt reduction with hydrogen, selective sputtering, and selective condensation of vaporization products resulting from micro-impacts (Morris, 1980; Hapke, 2001). The latter mechanisms are very effective in porous media (Starukhina et al., 1999) and now considered as dominative. Ferromagnetic resonance measurements can be used to detect metallic iron inclusions with sizes greater than 4 nm but less than 30 nm (Morris, 1980). If the value I_s is related to surface condensation processes, it would correlate with the total area of surface particles. The FeO bulk abundance is a function of the total volume of particles. Thus the ratio I_s/FeO should be a function of the particle size D . If I_s is strictly proportional to the surface area, then the ratio I_s/FeO should be inversely proportional to average particle size of regolith samples. It was found that for mature soils the ratio I_s/FeO is actually proportional to $D^{-0.18}$, whereas, for immature regolith this is $D^{-0.75}$ (Morris, 1980).

Using the Clementine UVVis mosaics, LSCC data, and Eq. (49) the distribution of I_s/FeO was computed (Shkuratov et al., 2005b; Pieters et al., 2006). The coefficients a_m , b_m , c_m , d_m , and e_m for this case are given in Table 5 and the I_s/FeO map is represented in Fig. 38c. This map looks very much like the agglutinate distribution, as can be anticipated. The resemblance reflects the process of increasing the amount of nanophase iron relative to total iron in the volume of regolith particles during agglutination. The relation between I_s/FeO and agglutinate content appears to be bi-modal (Pieters et al., 2006), which corresponds to the maria/highlands division. One of the reasons for the discrepancy could be different melting temperatures of mare and highland materials. Moreover, the proportion of meteoritic metallic iron would be greater in the low-Fe highlands, thus skewing the I_s/FeO .

4.7. Mapping of helium-3 abundance

The isotope ³He is a highly desirable energy source. As a fusion reactor fuel, ³He offers a number of advantages over tritium ³H. First, tritium is radioactive and, consequently, dangerous; whereas, the reaction involving ³He mainly produces high-energy protons inducing no prolonged radioactivity (Wittenberg et al.,

1986). On the Earth, helium is abundant in the form of ^4He . The lunar regolith has an essential content of the ^3He isotope in addition to ^4He (Wittenberg et al., 1986; Taylor, 1994). The source of ^3He is the solar wind irradiating the Moon's surface for billions of years. Solar-wind helium is implanted into the surface (few hundred angstroms thick) of regolith particles and partially stored there. A store of ^3He in a 3-m-thick regolith layer of an area of 1.5 km^2 can keep a 500-MW power station working for a year (Taylor, 1994). The greater portion of total helium is contained in fines of lunar regolith (the average particles size symbol $\leq 50 \mu\text{m}$).

There is a method to map ^3He abundance using optical data. At first glance this appears strange, since helium does not influence optical properties at all. However, the content of ^3He is found to depend on the content of such chromophoric elements as titanium whose amount can be estimated optically. This indirect technique seems to be promising, owing to its simplicity and the possibility of a global optical mapping of the Moon. Results of such estimates from the *Clementine* data have been reported by Johnson et al. (1999) and Shkuratov et al. (1999d).

The helium concentration in the lunar soil depends on two factors: the incident solar-wind flux and processes of soil outgassing. If the first factor is dominant, the helium concentration should exhibit latitudinal and longitudinal variations over the lunar disk (Johnson et al., 1999). If the amount of helium is mainly governed by outgassing, its concentration in the lunar soil should depend on the surface temperature and solubility limit at the given temperature. To support the domination of the outgassing effect, we can bring forward the following argument (Shkuratov et al., 1999d). The concentration ratios of solar-wind-implanted elements were found to be different from those in the solar wind (Haskin and Warren, 1991). The relative content of high diffusivity elements (H, He) is 1–3 orders of magnitude smaller than the value expected from their fractions in the solar wind; Haskin and Warren (1991) ascribed this effect to the different rates of outgassing for various elements. This means that the major portion of helium escapes from the regolith particles, and the residual small amount is determined by the regolith ability to hold helium, rather than the amount of incoming He. The latitude temperature effect decreases the rate of outgassing and leads to an increase of the ^3He concentration near the lunar poles. This is consistent with recent estimations by Cocks (2010) who has evaluated that because of their cryogenic temperatures, permanently shadowed polar lunar craters may have substantially higher levels of ^3He than sunlit lunar surfaces and are conservatively estimated to contain as much as 50 ppb or more. To avoid debates about the latitude trend, we here restrict our prognosis maps with latitudes $\pm 50^\circ$ (see below).

In accordance with the structure accommodation, helium implanted into solids can be divided into two fractions: strongly and weakly trapped helium atoms. Strongly trapped helium should have a high value of the activation energy of diffusion in a solid. This takes place if helium atoms are captured in some efficient traps of crystal lattice, for example, in vacancies. Atoms of weakly trapped helium take interstitial positions and can readily diffuse through the material. Predominantly, helium found in the lunar samples is strongly trapped (Haskin and Warren, 1991). Its concentration should be primarily dependent on the volume fraction of these phases in the regolith and on the degree of damage of the crystal lattice (soil maturity). Minerals with a relatively high conductivity, e.g., ilmenite, serve as efficient helium traps.

The high helium trapping efficiency of ilmenite was examined experimentally (Eberhardt et al., 1970; Taylor, 1994). In particular, a correlation between the TiO_2 and the ^3He contents of the lunar samples was found. This correlation is not close, as it is

affected by the variations in the soil maturity I_s/FeO . To describe the dependence of the ^3He concentration on the TiO_2 content and the soil maturity, Taylor (1994) used the parameter $[\text{TiO}_2 \cdot I_s/\text{FeO}]$, derived from a laboratory study of about 40 lunar samples taken from various Apollo landing sites (the correlation coefficient is about 0.91). The regression equation of this correlation dependence has the form

$${}^3\text{He}[\text{ppb}] = 0.2043[\text{TiO}_2 \cdot I_s/\text{FeO}]^{0.645}, \quad (50)$$

where the TiO_2 content is expressed in %. The parameters TiO_2 and I_s/FeO can be estimated from measurements of albedo and color ratios. For this purpose Earth-based observations were used (Shkuratov et al., 1999c). This allows a ^3He concentration map of the lunar visible hemisphere (Shkuratov et al., 1999d), which is shown in Fig. 39. The highest concentration of ^3He is observed in the western regions of Mare Tranquillitatis, especially its western part. Low concentrations of ^3He are characteristic of highlands. The lowest concentrations of ^3He are estimated for young craters and their ejecta formed by immature coarse-grained soil (e.g., see crater Tycho). Similar maps of higher resolution can be computed using *Clementine* UVVis data.

To estimate the store of ^3He at a given area of the lunar surface, one should know the thickness of the regolith layer and depth distribution of ^3He . The average thickness of the regolith layer is about 4–5 m for maria and 10–15 m for highlands (McKay et al., 1991). There is an approximate technique allowing maps of regolith layer thickness for large areas, e.g., for the lunar nearside (Shkuratov and Bondarenko, 2001). To map the regolith thickness, the Earth-based radar measurements by Thompson (1987) at 70 cm wavelength were used. The surface resolution of the radar data is about 2–5 km that is close to the resolution of the Earth-based chemical composition determinations retrieved from optical characteristics (e.g., Shkuratov et al., 1999c). Radiowave scattering in the regolith was modeled with the geometric optics approximation. For this purpose the 1D model (Shkuratov et al., 1999b) was somewhat generalized (Shkuratov and Bondarenko, 2001). The uppermost regolith interface is considered as a slightly undulated surface on the 1 m scale; whereas, the bottom interface (regolith–solid rock) consisting of rock fragments is assumed to be rather rough with a wide distribution of facet normals. The model deals with a small number of physical parameters, which yields single-valued results and can be easily applied to map the

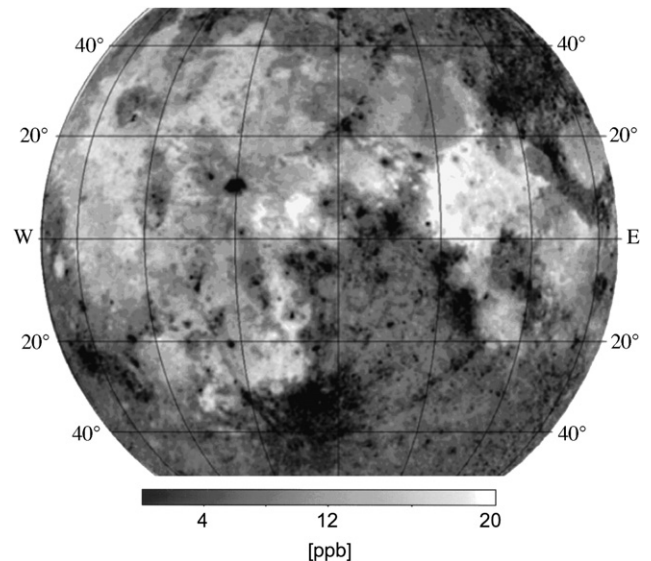


Fig. 39. Map of the visible hemisphere representing ^3He concentrations (the amount of ^3He per unit volume of the lunar regolith) (Shkuratov et al., 1999d).

regolith layer thickness. The model produces reasonable values of regolith thickness that are confirmed by comparisons with measurements made *in situ* (Nakamura et al., 1975). The regolith thickness map (Shkuratov and Bondarenko, 2001) is presented in Fig. 40. This map can be used for the determination of the total amount of ${}^3\text{He}$ in the 1 m^2 column of the regolith layer.

The second important factor is the depth distribution of ${}^3\text{He}$. The intensity of lunar regolith mixing was high in the past. According to an estimate by Melosh (1989), during the lifetime of the surface at the Apollo 11 landing site, the soil was mixed 2000, 100, and 10 times to a depth of 10 cm, 1 m, and 3–4 m, respectively. Such a mixing rate led Taylor (1994) to assume that the depth distribution of ${}^3\text{He}$ can be considered to be roughly

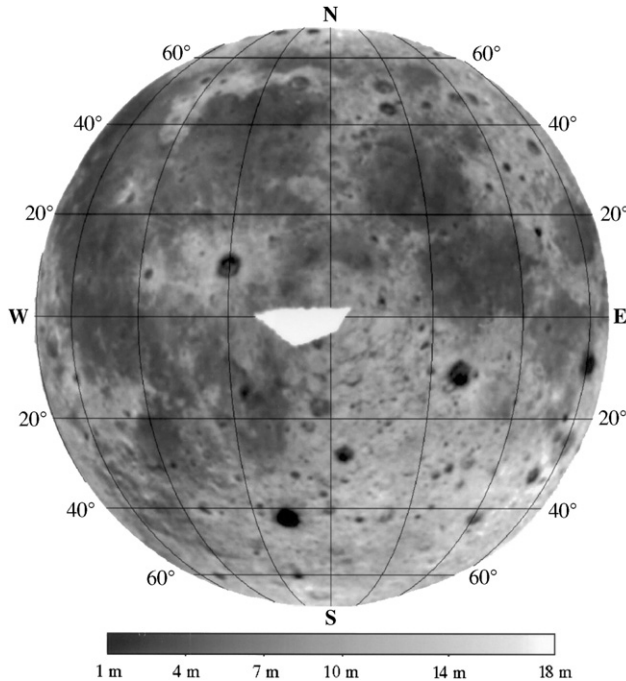


Fig. 40. Map of regolith layer thickness determined with radar (Thompson, 1987) and chemical content (Shkuratov et al., 1999b) data. The white area in the center of the lunar disk corresponds to lack of radar data.

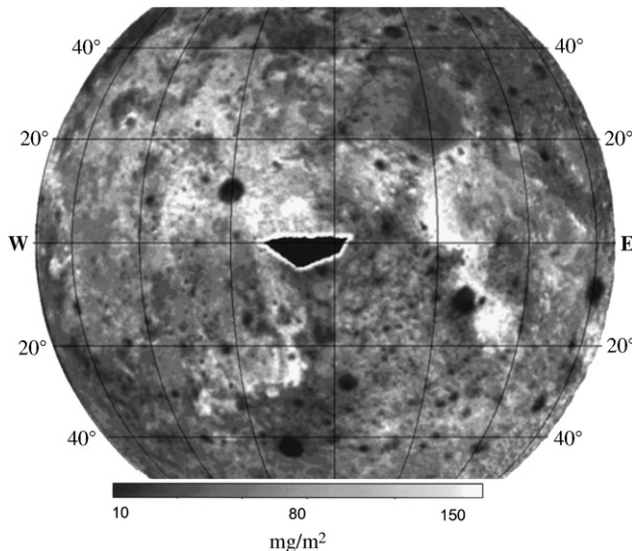


Fig. 41. Map of the visible hemisphere representing the total amount of ${}^3\text{He}$ per 1 m^2 of the regolith. The dark area in the center of the lunar disk corresponds to lack of radar data.

uniform. In support of this assumption, note that, although the regolith mixing took place mainly at the early stages of the regolith-cover formation when the intensity of the meteoritic bombardment was high, this time was long enough to saturate the particles appearing at the exposed surface with helium.

Fig. 41 shows the map that is the product of the ${}^3\text{He}$ concentration by the regolith thickness. This product characterizes the total amount of ${}^3\text{He}$ in the regolith layer, i.e., the amount that can be extracted from 1 m^2 of the lunar surface. Correlation between the thickness of the regolith layer and the concentration of ${}^3\text{He}$ was studied (Shkuratov et al., 1999d). The correlation is inverse and nonlinear. Therefore, at the determination of the total ${}^3\text{He}$ amount per 1 m^2 , the low concentration of ${}^3\text{He}$ can be partially compensated by the high thickness of the regolith layer. This is typical of, e.g., Mare Nectaris.

Another map of the total amount of ${}^3\text{He}$ has been suggested using data from a multi-channel microwave radiometer on the Chang-E1 lunar satellite (Zhe and Qiu, 2010); the global inventory of helium-3 was evaluated as being 6.6×10^8 , 3.7×10^8 kg for the lunar nearside and 2.9×10^8 kg for the lunar farside.

5. Polarimetry

The polarimetric method in astrophysics was used for the first time in the studies of the Moon early in the 19th century. However, the studies gave relatively little diagnostic information. It was only in recent decades when the data appeared that indicated what sort of quantitative information on the lunar surface can be derived from polarimetric measurements.

Among the papers that contain a large number of lunar polarimetric measurements, we note those by Lyot (1929), Dollfus and Bowell (1971), Kvaratskheliya (1988), Shkuratov et al. (1992), Shkuratov and Opanasenko (1992), Opanasenko and Shkuratov (1994a), and Dollfus (1998). The features of the phase curve of the lunar linear polarization are seen in Fig. 3b. There is a minimum of polarization that is negative and equals about -1% at 11° . A maximum (about $+7\%$) occurs at $\alpha_{max} \approx 105^\circ$ for $\lambda \approx 600$ nm. The phase angle at which the negative polarization transforms to the positive one is called the inversion angle α_{inv} and is approximately 23° .

5.1. Positive polarization and deviation from the Umov law

At $\alpha > 23^\circ$, the Moon exhibits a positive polarization. The positive branch extends in the direction of larger phase angles at least up to about 165° (Lyot, 1929). The polarization degree P near the maximum closely correlates with the albedo of the surface. This inverse correlation is called the Umov law. The correlation relates to the definition of the polarization degree (see Introduction): $P(\lambda) \sim 1/A(\lambda)$, if the numerator $Q = (I_\perp - I_\parallel)$ depends insignificantly on A (Dollfus and Bowell, 1971; Shkuratov and Opanasenko, 1992). In a log-log scale the dependence is close to linear. This is especially true for P_{max} . In this case, the correlation is so strong that investigation of the parameter P_{max} itself can lose significance. Dollfus and Bowell (1971) have found that the regression line of the correlation can be described as follows:

$$\log A + a \log P_{max} = b, \quad (51)$$

where a and b are constants that were determined in Dollfus and Bowell (1971): $a = 0.724$ and $b = -1.81$ at $\lambda = 0.6 \mu\text{m}$, if P and A are presented in natural units, A being determined at $\alpha = 5^\circ$. Later, Shkuratov and Opanasenko (1992) found somewhat different values: $a_1 = 0.845$ and $b_1 = -1.801$ for $\lambda = 0.63 \mu\text{m}$; $a_2 = 0.795$ and $b_2 = -1.871$ for $0.43 \mu\text{m}$, A being determined at $\alpha = 6^\circ$.

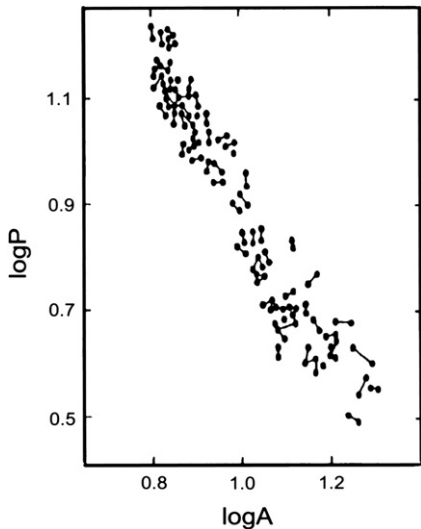


Fig. 42. Correlation of polarization degree measured at $\alpha=96^\circ$ with albedo (Shkuratov and Opanasenko, 1992). Segment joints point to corresponding measurements of the same sites at different lunations.

(Sytinskaya-Sharonov absolute calibration) and P_{max} was considered equal to $P(90^\circ)$.

Fig. 42 depicts a correlation diagram $\log P - \log A$ constructed on the base of discrete photopolarimetric observations described in Shkuratov and Opanasenko (1992) and Opanasenko and Shkuratov (1994a); all values of polarization degree are measured at a phase angles near 90° . Segments join points corresponding to observations of the same sites at different lunations, but close phase angles. The dispersion of the segment lengths is noticeably less than the overall point scatter of the diagram. It means the deviations from the regression line contain information. It is convenient to study these deviations considering b in Eq. (51), as a parameter, not as a constant.

Such a study started in Kharkov observatory (Shkuratov, 1981; Shkuratov and Basilevsky, 1981). Later on, other authors (Shevchenko and Skobeleva, 1995; Dollfus, 1998) began to develop this approach. The parameter b appears to be closely related to the characteristic size of the particles D of a light-scattering surface. Using the data of laboratory photopolarimetric measurements of lunar soil samples of the spaceprobe *Luna-24*, the following dependence was obtained (Shkuratov and Opanasenko, 1992):

$$D = 0.03 \exp(2.9b), \quad (52)$$

where A and P (Eq. (51)) are presented in % and %, respectively, and D is given in μm . Similar calibration dependencies are also reported by Shevchenko and Skobeleva (1995) and Dollfus (1998). We should note that the term “characteristic particle size” is very conditional, since a significant part of the lunar soil particles is in the form of aggregates of fragments. The $D(b)$ dependence should be applied gingerly, as it perhaps is not universal and may depend on λ .

Fig. 43 displays the following: (a) equigonal albedo, (b) polarization degree, and (c) parameter b (distribution of the characteristic size of particles) for the western part of the visible lunar hemisphere. In the latter case, darker tones correspond to smaller particles. Rough estimates of the D variations by the images and Eq. (52) have shown that the typical range of particle size is $50\text{--}100\,\mu\text{m}$. The highland surface, on average, is more finely grained. This is in accordance with laboratory investigations of lunar samples (Engelhardt et al., 1976) and the map shown in Fig. 35b. The bright (young) craters have soil with

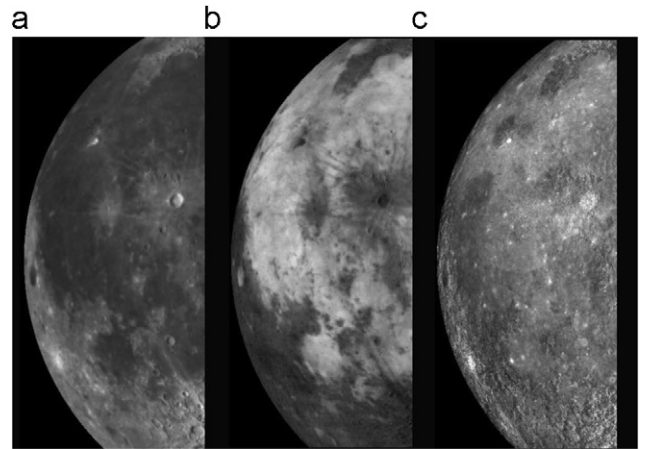


Fig. 43. Earth-based telescope photopolarimetric images of the western part of the lunar nearside: (a) an equigonal albedo image (after compensation of the brightness trend from limb to terminator), (b) an image of polarization degree, and (c) an image of deviation from Umov's law, the parameter $(P_{max})^a A$ (Shkuratov and Opanasenko, 1992; Shkuratov et al., 2007b).

relatively larger particles, which correlates with the fact that this soil is immature. For example, rayed craters, including the crater Aristarchus, produce a large value of b corresponding to $D \approx 100\,\mu\text{m}$. Several large areas within the region under study have lower b values. These are the areas comprising the Harbinger Mounts and Aristarchus Plateau (the Wood spot), the Marius Hills area, Rumker Mons. An interpretation of their peculiarities has been presented by Shkuratov and Basilevsky (1981). A common characteristic of these three areas is probably volcanism that occurred on relatively great topographic heights. Therefore, the magma should have the property of increased elevation. This requires increased volatile content in the magma and raises the probability of fountaining and formation of mantles similar to the well-known pyroclastic deposits of orange-and-black glass spherules at the Apollo-17 landing site. The average size of the spherules is rather small, about $40\,\mu\text{m}$, in agreement with the prediction of formula (52).

A phase angle, at which polarization maximum is achieved, also has been mapped at two wavelengths (Korokhin and Velikovsky, 2005). Fig. 44 presents these distributions obtained at $\lambda=669\,\text{nm}$ (a) and $445\,\text{nm}$ (b) using photopolarimetric images acquired at 10 phase angles. As can be seen, this parameter correlates with albedo (or P_{max}): the larger the albedo, the lesser the α_{max} . Earlier this was found by Dollfus and Bowell (1971) with discrete photopolarimetric measurements:

$$\alpha_{max} = 97^\circ + 0.517 P_{max}, \quad (53)$$

P_{max} being given in %. Korokhin and Velikovsky (2005) have also shown that the parameters α_{max} and P_{max} depend on wavelength only through albedo. Except for noise, no spatial variations were found for the ratio $\alpha_{max}(0.67\,\mu\text{m})/\alpha_{max}(0.46\,\mu\text{m})$ (Korokhin and Velikovsky, 2005).

The physics governing Umov's law is quite clear: in a bright powder-like surface, multiple scattering is highly pronounced; i.e., light interacts with many particles before being completely absorbed or leaving the discrete medium. This multiple scattering happens between particles that are not located in one plane, which means that the scattering plane changes at every scattering event. In terms of Stokes parameters describing the scattered light (Bohren and Huffman, 2004), this leads to a redistribution of polarization states between the three Stokes parameters Q , U , and V . Thus, the lesser the absorption, the lesser the polarization degree, the higher the multiple scatter contribution to albedo. The first theoretical description of the Umov law was suggested by



Fig. 44. A map of α_{max} of the eastern portion of the lunar disk in red and blue light. The values of α_{max} (degrees) were determined with polarimetric images obtained at 10 different phase angles (Korokhin and Velikodsky, 2005). The parameter scale is common for both images.

Rosenberg (1956). He derived from the radiative transfer equation a formula for polarization

$$P = \left(P_0 + P_\infty \frac{\zeta - \zeta_0}{(1 + \zeta_0)q} \right) \left(1 + \frac{\zeta - \zeta_0}{(1 + \zeta_0)q} \right)^{-1}, \quad (54)$$

where $\zeta = \tau/\sigma$ is the absorption coefficient divided by the scattering coefficient, P_0 is the polarization degree at $\zeta = \zeta_0$ ($\zeta_0 \ll 1$), $P_\infty = \lim_{\zeta \rightarrow \infty} P(\zeta)$, and q is the sum of the relative contributions of scattering orders presented in portions of single scattering.

A model of the formation of $P(\alpha)$ has been suggested by Hapke (1993). It considers that the polarization of regolith-like surfaces is produced only by single scattering; although $P(\alpha)$ is a function of the multiple scattering components, they are considered to be unpolarized. This is an approximation, since the polarization of low scattering orders may noticeably contribute to the branch of negative polarization at small α and shift α_{max} to smaller values (Shkuratov et al., 2002; Stankevich et al., 2007b). Nevertheless, the model qualitatively correctly treats the Umov law. In this approximation Hapke (1993) uses the Fresnel reflection polarization produced by the surface of regolith particles. This model predicts α_{max} at phase angles much larger than those observed for the lunar areas. Laboratory measurements show that large α_{max} can be really observed for bright powdered surfaces consisting of rather big particles (Shkuratov and Opanasenko, 1992). To obtain realistic α_{max} for the Moon, it is more suitable to use polarization indicatrixes of randomly shaped or aggregated particles whose size compared to the wavelength. This can be considered theoretically (Zubko et al., 2006, 2008, 2009) or experimentally (e.g., Munoz et al., 2000, 2006) for particles with different optical parameters.

The influence of multiple scattering on positive polarization also has been studied with the help of ray-tracing simulations of semitransparent (dielectric) particles; in particular, the inverse correlation between P_{max} and albedo was reproduced (Wolff, 1980; Shkuratov and Grynko, 2005). It was also shown that parameters of the correlation depend on particle shape (Shkuratov and Grynko, 2005). Polarization degree depends on albedo and absorption, not only in the case of interparticle scattering, but also for a single semitransparent particle (Grynko

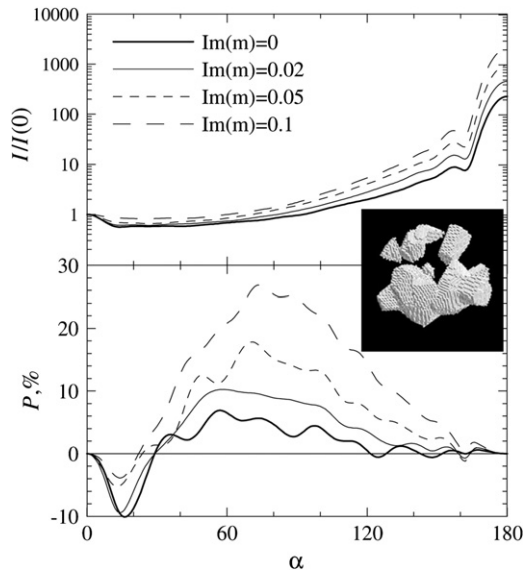


Fig. 45. Phase curves of normalized intensity and linear polarization degree of the agglomerated debris particles at different imaginary parts of refractive index. Size parameter and real part of refractive index are equal to $X=14$ and $n=1.5$ (Zubko et al., 2009).

and Shkuratov, 2002, 2003). These calculations were carried out in the geometric optics approximation, but the lunar surface contains a significant amount of particles whose size is compared to the wavelength. The Umov effect for single irregularly shaped particles of small sizes compared to wavelength has been studied in Zubko et al. (2006, 2009, 2011). This effect is observed in this case as well. Fig. 45 depicts several plots corresponding to an agglomerated particle with different absorption coefficients. The parameter P_{max} sharply decreases with decreasing imagery part of refractive index $Im(m)$. Thus an analog of the Umov law also is valid for small particles of different shapes (Zubko et al., 2011).

5.2. Spectropolarimetry

Along with the studies of absorption bands in a region of 1 and 2 μm , attempts have long been made to find weak absorption bands for the Moon. Such bands have been detected more-or-less reliably for asteroids (e.g., Shestopalov et al., 2008; Cloutis et al., 2010), while there are no reliable data for the Moon. The difficulty in the detection is the necessity to divide the initial spectral data by the spectra of the Sun. Due to the discrepancy between the Fraunhofer lines in the measured spectrum and the reference spectrum, the calculated lunar spectrum may exhibit irregularities of several percents. There were even attempts to interpret these as weak absorption/emission bands. When the solar data became more reliable, the reports on the weak lunar bands stopped; however, this does not close the problem at all.

According to laboratory measurements, the weak bands in the vicinity of 0.490, 0.505, and 0.550 μm can actually be observed for pyroxenes (gedenbergite and ferrogedenbergite). These are forbidden bands that are attributed to the Fe^{2+} ion that occupies the octahedral M1 and M2 positions in the pyroxene lattice structure. Note also that there is some hope in detecting the weak band of the Cr^{3+} ion ($\lambda=0.625 \mu\text{m}$) for the Moon. In the reflection spectra of some samples of lunar soil with a high content of chromium, this band is clearly seen (Burns, 1993).

Spectropolarimetry is a promising method to search for weak bands in the visible range of lunar spectrum. Spectral dependences of the polarization degree are more precise than albedo measurements, since the dependencies are always relative; there

is no need to divide the measured spectral intensity by the solar spectrum. The spectropolarimetric method is based on the inverse correlation between the albedo and the polarization degree measured at large enough α (the Umov effect). Due to this effect, all features of the spectral albedo show up in the corresponding spectral behavior of the polarization degree. Opanasenko and Shkuratov (1994) made an attempt to detect weak absorption bands polarimetrically for several regions of the lunar surface at $\alpha \approx 50^\circ$ (positive polarization) in the range 0.48–0.57 μm with spectral resolution of 2 nm. At a level of sensitivity of several tenths of %, no irregularities were found in the polarization spectrum. But this has been obtained only for five sites; thus the measurements do not settle the question of the existence of weak absorption bands in the lunar soil spectrum.

If one performs the polarimetry of the Moon in two spectral bands, it appears to be possible to study the so-called polarimetric color ratio (spectropolarimetric index) $C_p(\lambda_1/\lambda_2)$, which is determined by analogy with the color ratio as $C_p(\lambda_1/\lambda_2)=P(\lambda_1)/P(\lambda_2)$, where $P(\lambda)$ is the polarization degree at wavelength λ . The parameter $C_p(\lambda_1/\lambda_2)$ can be studied for phase angles at which the quantities $P(\lambda_1)$ and $P(\lambda_2)$ differ significantly from zero. In practice, this could be done for phase angles near α_{max} . There are few data on the relation between the index $C_p(\lambda_1/\lambda_2)$ and other physical characteristics of the surface. Using the telescope data of discrete measurements made by Kvaratskheliya (1988) for landing sites of several spacecrafts, Shevchenko et al. (1993) found a correlation between the spectropolarimetric index $P_{max}(0.42 \mu\text{m})/P_{max}(0.70 \mu\text{m})$ and the maturity degree of the lunar regolith. This correlation was not confirmed by a more complete data analysis that produced an image of the parameter at low spatial resolution of the lunar disk (Korokhin and Velikodsky, 2005).

Fig. 46 presents images of the northern portion of Oceanus Procellarum at $\alpha=96^\circ$: (a) brightness distribution obtained at $\lambda=0.63 \mu\text{m}$; (b) polarization degree distribution ($\lambda=0.48 \mu\text{m}$);

(c) color ratio $C(630/480 \text{ nm})$; (d) spectropolarimetric ratio $C_p(480/630 \text{ nm})$; and (e) color ratio of the second Stokes parameters $C_Q(480/630 \text{ nm})=Q(480 \text{ nm})/Q(630 \text{ nm})$ that also equals $C_p(480/630 \text{ nm})/C(630/480 \text{ nm})$. The parameters $C(630/480 \text{ nm})$ and $C_p(480/630 \text{ nm})$ are closely correlated with each other; this may be considered as a consequence of the Umov law. The image $C_p(480/630 \text{ nm})$ does not resemble maps of maturity degree (cf. Fig. 38). This agrees with results by Korokhin and Velikodsky (2005). To study the correlation of the parameters $C(630/480 \text{ nm})$ and $C_p(480/630 \text{ nm})$ in more detail we show in Fig. 46e the ratio $C_p(480/630 \text{ nm})/C(630/480 \text{ nm})$ that is just the color ratio of the second Stokes parameters $Q(\lambda_1)/Q(\lambda_2)$. This ratio reveals differences between mare and highland regions: the ray system of the crater Kepler shows up, but overall this image has few details.

5.3. Negative polarization

The investigation of the parameters of the negative polarization branch at small phase angles is complicated, since this is a relatively weak effect (see Fig. 3). The nature of this polarization is not completely understood; therefore, this line of lunar measurements was not adequately developed. The negative polarization of the light scattered by powdered surfaces may arise probably due to several reasons (Shkuratov et al., 1994b). For the Moon the main reason seems to be the negative polarization from single-particle scattering. As has been shown experimentally (e.g., Munoz et al., 2000; Shkuratov et al., 2004, 2006) and theoretically (e.g., Zubko et al., 2006, 2009) this polarization is an intrinsic characteristic of irregularly shaped particles having sizes comparable to the wavelength. There is no simple explanation of this polarization, though attempts to propose it exist (e.g., Tyynelä et al., 2007). Light-scattering calculations made for irregularly shaped particles (Zubko et al., 2006, 2009) indicate conspicuous dependence of the parameter P_{min} on the absorption coefficient of the particle (Fig. 45); there is an inverse correlation between parameters $|P_{min}|$ and P_{max} .

Fig. 47a,b shows data of laboratory measurements of single particles in air and powdered surfaces thereof; phase curves of normalized intensity (a) and degree of linear polarization (b) for samples of Pinatubo volcanic ash in red and blue light are depicted. These studies were carried out with the Kharkov photometer/polarimeter for particulate surfaces (Shkuratov et al., 2004, 2006) and the equipment developed at the University of Amsterdam for single particles (e.g., Munoz et al., 2000). Large symbols in Fig. 47a,b correspond to scattering measurements of single particles, while small symbols correspond to particulate-surface data (Shkuratov et al., 2004). We see the depth of the negative polarization branch of small single particles may achieve 5%; if such particles form a powdered surface, the depth considerably decreases due to incoherent multiple scattering (Shkuratov et al., 2004, 2006).

The second reason for the negative polarization may be an interference effect that occurs in multiple scattering light traverses along the so-called direct and time-reversed trajectories; for bright lunar areas this may also be a reason for the occurrence of the brightness opposition effect (see Section 3.4). The interference mechanism was suggested in Shkuratov (1985, 1988) and Muinonen (1989) and then developed in many papers (e.g., Mishchenko and Dlugach, 1993; Muinonen, 2004; Shkuratov et al., 1994b; Videen et al., 2006). Although initially this was proposed as a universal approach to explain all observed negative polarization branches including that of the Moon (Fig. 3), later, the understanding came that too small characteristic distances between scatterers are necessary to generate wide negative polarization branches observed. Therefore, the interference (coherent backscattering enhancement) mechanism is applied to describing narrow negative polarization branches inherent for bright finely grained surfaces like deposits of MgO smoke

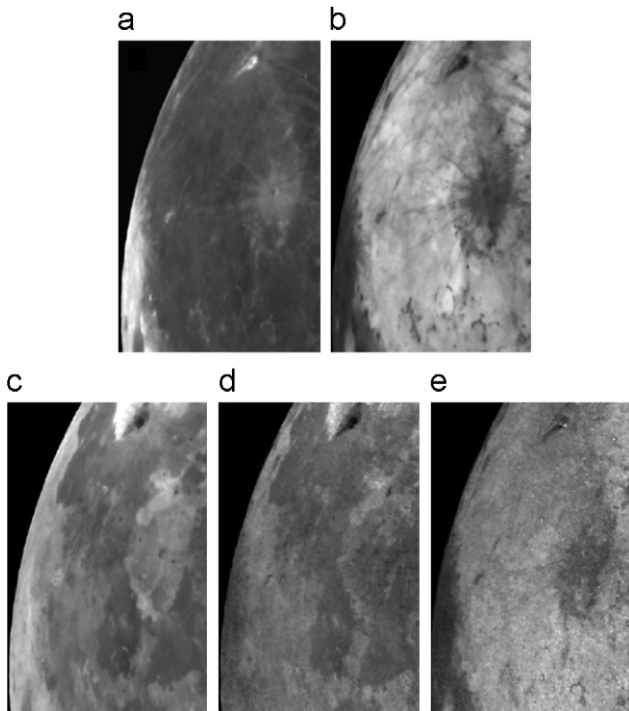


Fig. 46. Photopolarimetric parameters of the northern portion of Oceanus Procellarum at $\alpha=96^\circ$: (a) albedo distribution ($\lambda=0.63 \mu\text{m}$); (b) polarization degree distribution ($\lambda=0.48 \mu\text{m}$); (c) color ratio $C(630/480 \text{ nm})$; (d) spectropolarimetric color ratio $C_p(480/630 \text{ nm})$; and (e) color ratio for the second Stokes parameter $C_Q(480/630 \text{ nm})=Q(480 \text{ nm})/Q(630 \text{ nm})$.

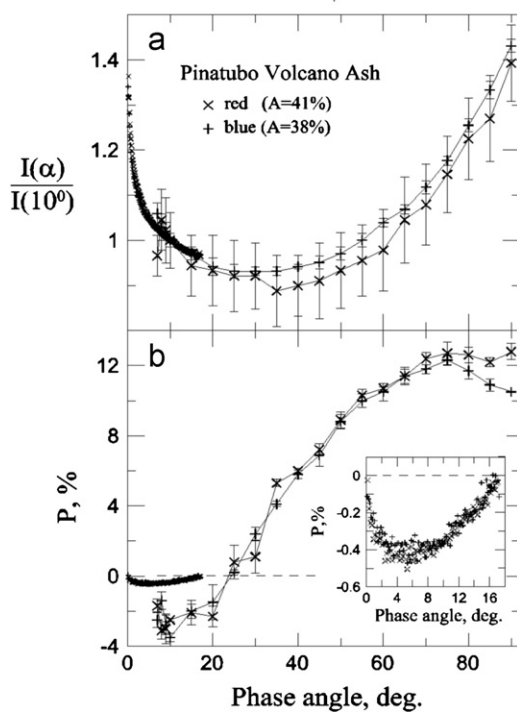


Fig. 47. Phase curves of (a) normalized intensity and (b) degree of linear polarization for samples of Pinatubo volcanic ash in red and blue light. Large symbols correspond to single-scattering measurements of single particles, small symbols present particulate surface data (Shkuratov et al., 2004, 2006). The inserted plot placed in the bottom right corner is a magnified portion of polarimetric data for the particulate surface. The albedo values correspond to measurements of the particulate surface.

(Lyot, 1929). Such branches are even called the “polarimetric opposition effect” (Mishchenko et al., 2006). On the other hand, it was recently demonstrated with the rigorous solution of Maxwell equations for a cluster of many scatterers that the coherent backscattering enhancement effect is valid even if the characteristic interference base is smaller than the wavelength (Zubko et al., 2008; Mishchenko et al., 2009a,b). Thus, the interference mechanism may contribute to negative polarization at fairly large α overlapping with the mechanism originating from single particle scattering. Another mechanism related to the so-called near-field effects also has been considered (e.g., Petrova et al. 2007). However, its consideration appears fairly opaque and is difficult to implement in practice (Shkuratov and Zubko, 2008).

At present, there appear to be few practical applications for a quantitative modeling analysis of the negative polarization origin of the lunar surface. We could suggest using laboratory polarimetric measurements (Shkuratov et al., 2002) within an analysis of lunar observations. The negative polarization parameters closely relate to the size of the particles composing the surface and to the degree of its heterogeneity at the scales on the order of the light wavelength (e.g., Shkuratov, 1987; Shkuratov et al., 1992, 1994b). According to laboratory measurements of finely disperse mixtures of materials with different albedo, of which the lunar regolith is an example, the depth and width of the negative branch significantly increase with the degree of optical heterogeneity of the mixture (Shkuratov, 1987; Shkuratov et al., 1994b).

Fig. 48 represents polarimetric measurements of MgO and Fe_2O_3 powders and their mixtures illuminated by red and blue light (Shkuratov, 1987). These samples were prepared by drying alcohol suspensions of particles. The MgO sample is spectrally

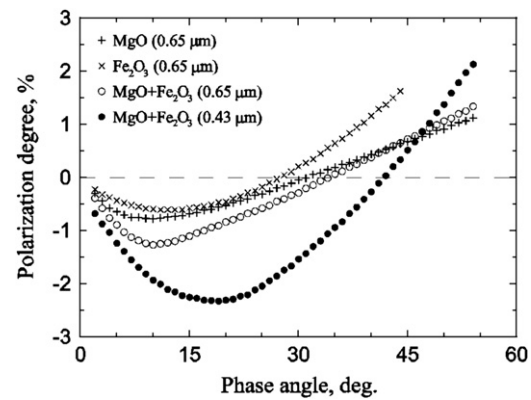


Fig. 48. Polarimetric measurements of MgO and Fe_2O_3 powders and their mixtures at red and blue light (Shkuratov, 1987). At different spectral ranges the negative polarization branches of the MgO sample are the same. For Fe_2O_3 powder both the branches are also shallow; though in blue light its inversion angle is smaller, near 16°.

neutral; whereas, the Fe_2O_3 powder is very red, having albedo about 4% and 35% in blue and red light, respectively. One can see the negative polarization is very strong in blue light when the $\text{MgO}+\text{Fe}_2\text{O}_3$ mixture (1:1) is maximally contrasting optically. This effect can be explained as follows. The particles of MgO have almost zero absorption and produce a deep negative polarization branch (see Fig. 45), while dark Fe_2O_3 particles effectively suppress multiple scattering; this suppressing increases the relative contribution of polarization from MgO particles. Thus, polarimetric measurements at small phase angles potentially enable one to estimate the concentration and albedo-contrast degree of light- and dark-colored components of the lunar soil. We mentioned above that MgO may produce a narrow negative branch that is deep and asymmetric (Lyot, 1929); at first glance it is inconsistent with Fig. 48 that shows a relatively shallow and wide branch. The reason of the difference is that the curves in Fig. 48 correspond to MgO smoke deposits compressed by drying alcohol suspensions of particles (Shkuratov et al., 1994b, 2002).

We show below several examples of mapping the negative polarization parameters (Opanasenko et al., 2009; Shkuratov et al., 2008). Fig. 49 displays the southwestern part of Oceanus Procellarum: (a) equigonal albedo (for comparison); (b) the depth of polarimetric phase curve at minimum polarization P_{min} ; (c) the inversion angle α_{inv} obtained at a wavelength $\lambda_{eff}=0.52 \mu\text{m}$; and (d) the slope h of the polarimetric phase curve in α_{inv} .

The magnitude of the minimum of the negative polarization, being as low as about 1%, varies over the lunar surface in the range of about 0.5–1.5%. The largest values of the parameter $|P_{min}|$ appear to be typical of surface regions with medium albedo. For the mare regions, the lowest values of $|P_{min}|$ are in the upper-left portion, to the northeast of the crater Flamsteed, and close to the image center, to the east of the formation Helmet, located at 16.7°S, 31.3°W. These areas are weakly distinguishable in albedo. The mare/highland boundary is weakly contrasting; however, it can be traced practically everywhere. Many bright craters also are seen in Fig. 49b; the typical values of $|P_{min}|$ here are 0.8–0.9%. It is worth noting that not all bright craters are distinguished by the parameter P_{min} . This can be caused by the different ratio of the fine and coarse fractions in the lunar regolith. The high values of $|P_{min}|$ are typical of some highland areas and small bright formations located in the maria. Examples are the formation Helmet or the formation seen to the left of the crater Euclides. The $|P_{min}|$ –albedo correlation diagram has a complex, horseshoe-shaped appearance (Shkuratov and Opanasenko, 1992; Shkuratov et al., 2008; Opanasenko et al., 2009): for low-albedo regions a

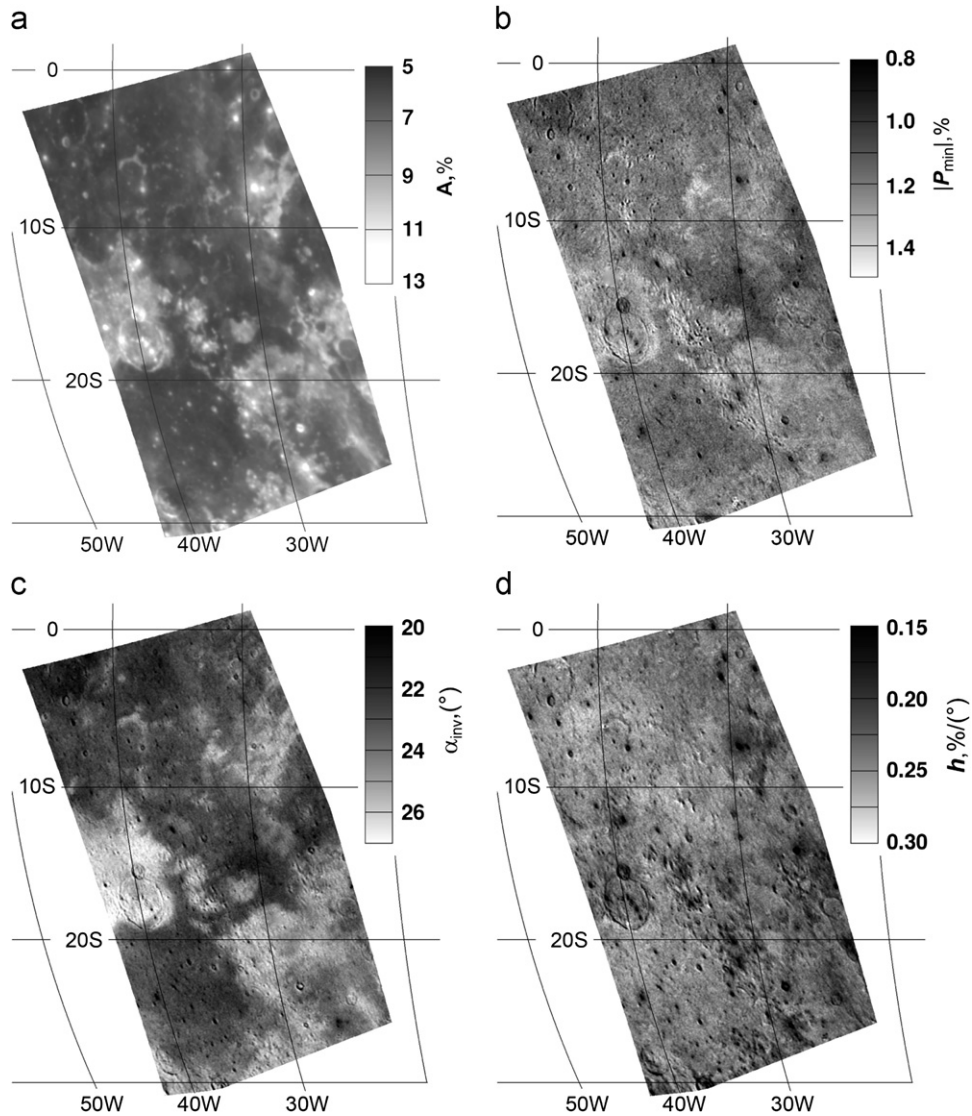


Fig. 49. Polarimetric images of the southwestern portion of Oceanus Procellarum: (a) equigonal albedo (for comparison); (b) the depth of the polarimetric phase curve at minimum polarization P_{min} ; (c) the inversion angle α_{inv} ; and (d) the slope h of polarimetric phase curve at the inversion angle α_{inv} .

direct correlation is observed, while for the high-albedo areas an inverse correlation exists.

An example showing the α_{inv} distribution is given in Fig. 49c where the mare/highland contrast is sharp. For the highlands and maria the typical values of α_{inv} are $25\text{--}26.5^\circ$ and $20\text{--}24^\circ$, respectively. Young craters show α_{inv} lower than the surrounding mare and highland regions by $1\text{--}2^\circ$. The largest values of $\alpha_{inv}\sim 27^\circ$ are seen in the highland area in the southern part of the crater Gassendi. The parameter α_{inv} depends strongly on albedo. Fig. 49d shows an image of the distribution of the polarimetric slope h . Typical values of this parameter are between 0.23% and 0.30% per degree. This image is relatively noisier than those considered above, as this parameter is calculated through differentiation. The lowest values of the parameter, $h\sim 0.15\%$ per degree, are observed near the bright mare and highland craters. An example of an area with high values of polarimetric slope is the area southward of the crater Gassendi and the region southeastward of the crater Flamsteed. The correlation obtained between h and albedo is not strong, which is somewhat different from the dependence observed in asteroids (Zellner et al., 1977). This can be related to the fact that the albedo and parameter h variations in lunar formations are much larger than those in asteroidal formations.

5.4. Other polarimetric parameters

The state of the linear polarization of scattered light is characterized not only by the polarization degree, i.e., the second Stokes parameter Q , but the orientation of the polarization plane characterized by the third Stokes parameter U or the angle ϑ (see the section “Introduction”). The observations carried out by Lyot (1929) showed that at large phase angles this plane almost coincides with the scattering plane (within the limits of $\pm 0.5^\circ$), i.e., with the plane of the lunar photometric equator. Physically, this is quite explicable. The deviation of the polarization plane from the scattering plane will take place if the surface under study exhibits a certain physically distinguished direction. For example, the surface may have an anisotropic structure or be inclined in such a way that the average normal lies beyond the scattering plane. For the Moon the surface normals on scales comparable to interparticle light scattering are distributed more-or-less isotropically in any point of the lunar disk. Owing to that the angle ϑ characterizing the polarization plane variations should be very small.

We verified the Lyot (1929) observations by computing an image of ϑ variations at α near 90° . Data described in Shkuratov et al. (2007b, 2008) and Opanasenko et al. (2009) were used.

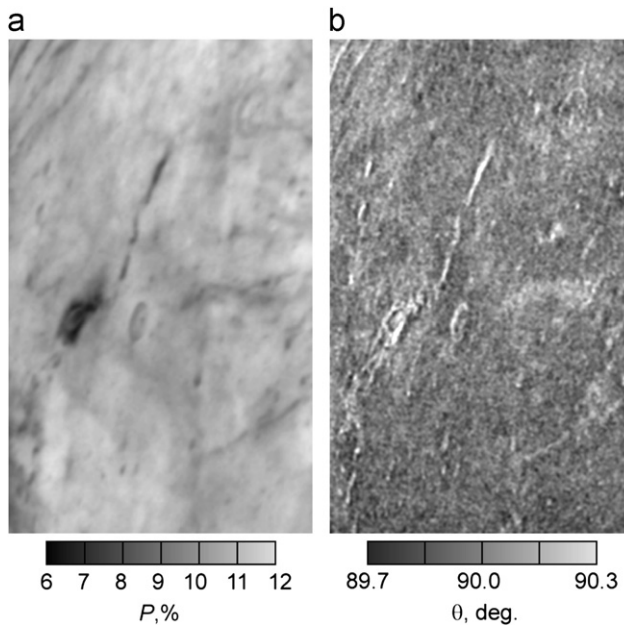


Fig. 50. Images of the central portion of Oceanus Procellarum: (a) the polarization degree and (b) the angle ϑ that characterizes the polarization plane orientation.

Fig. 50 shows maps of the polarization degree (a) and ϑ variations (b) for the central part of Oceanus Procellarum. The amplitude of these variations is somewhat less than that measured by Lyot. The map of ϑ is very noisy. There are several instances when ϑ variations correlate with albedo and morphological units; this relates to the influence of local topography and drawbacks of image coregistering. At polarimetric imagery with a high resolution from lunar orbit, systematic local inclinations of micro- and meso-topography normals can be large enough to influence the position of the polarization plane in the lunar highlands.

At small phase angles, where the negative polarization branch begins, the measurements of the variations of the polarization plane are also interesting. For example, at phase angles of about 1–2°, Lyot (1929) discovered a weak radial component of the polarization of the light flux scattered by the Moon in the vicinity of the limb. This effect was confirmed by Shkuratov and Opanasenko (1990). The reasons why this polarization occurs are not yet clear; however, this is undoubtedly a geometric effect.

The problem associated with a change of the polarization sign in passing through the point of inversion has intrigued observers studying the Moon over many years. How does the inversion occur, in the form of a jump, or a gradual rotation of the polarization plane? It follows from general considerations that a gradual rotation of the polarization plane can be observed only when the structure of the light-scattering surface has a distinguished direction and/or when this surface has an inclination which violates the symmetry with respect to the scattering plane. High-precision polarimetric measurements by Opanasenko and Shkuratov (1994) of various regions of the lunar surface did not reveal reliable signatures of a gradual rotation of the polarization plane in passing through the inversion point. However, the measurements of this kind could be repeated in the limb zones of the Moon near the poles, where the deviation of the surface average normal from the scattering plane may be significant. The north and south poles must give different directions of rotation of the polarization plane. The strong dependence of the results of measuring this effect on the precision, with which the vector of instrumental polarization is taken into account, should be particularly emphasized. Thus, such measurements must be carried out with particular care.

The first reliable measurements of circularly polarized light from the Moon were self-denying conducted by M. Pospergelis in 1964

(Lipsky and Pospergelis, 1967). These measurements were confirmed after some time (Kemp et al., 1971). The polar effect of circular polarization (see definition in Introduction) discovered at $\alpha < 30^\circ$ is: $V_N < 0$ and $V_S > 0$ in the northern and southern hemispheres, respectively. At $\alpha > 30^\circ$ the situation is opposite, $V_S < 0$ and $V_N > 0$; the sign is defined according to Kemp et al. (1971). The polar effect is observed for the Moon and Mercury as well as for planets with atmospheres. However, at phase angles $< 30^\circ$, signs of circular polarization for atmosphere and atmosphereless planets are opposite. The circular polarization degree is found for the Moon to be $< 0.001\%$ at $\alpha \approx 36^\circ$ (Lipsky and Pospergelis, 1967). At $\alpha = 90^\circ$ the polarization near the poles is $V_N = 0.004\%$ and $V_S = 0.003\%$. The following relationships are valid for the circular polarization: $V(\alpha, \gamma, \beta) = -V(\alpha, \gamma, -\beta)$, $V(\alpha, \gamma, \beta) = -V(\alpha, -\gamma, \beta)$, and $V(\alpha, \gamma, \beta) = -V(-\alpha, \gamma, \beta)$. Laboratory measurements have confirmed these regularities, including the existence of an inversion phase angle of the parameter V for different samples (e.g., Degtyarev and Kolokolova, 1992). This angle widely varies and hardly relates to the inversion angle of linear negative polarization.

All these properties can be explained if we have significant anisotropic double (multiple) scattering (Bandermann et al., 1972). Indeed, for single scattering of unpolarized light from a large ensemble of randomly oriented particles, induced circular polarization is not feasible (Bohren and Huffman, 2004); this is just the lunar regolith case. In the first scattering event of initially unpolarized light, partial linear polarization may arise; at a second scattering event partial circular polarization may appear at some observation/illumination geometries, which does not vanish because of particle orientation averaging. The anisotropy in double scattering occurs when the surface normal is beyond the main plane of scattering. The greatest inclinations of the normal occur at the lunar poles.

An interesting characteristic of the lunar surface is the coefficient of light depolarization. The distribution of this quantity can be obtained by investigating the Earthshine on the Moon. At a lunar phase angle near 90°, the light from the Earth illuminating the Moon is polarized. The degree of polarization depends on the state of the Earth's atmosphere and may be as large as several tens of %. The light from the Earth, scattered by the lunar surface, is depolarized differently depending on the region. As indicated with the investigation made by Dollfus (1962), lighter regions of the surface depolarize the light stronger than darker ones. Note that the measurements made by Dollfus have been carried out almost 50 years ago, nevertheless, they are still unique. The correlation between depolarization and albedo, as well as the correlation between the positive polarization degree and albedo are manifestations of the Umov effect. Therefore, we may expect that the parameter characterizing the deviation of the depolarization-albedo correlation from the regression line will appear to be diagnostically suitable for determining the structural features of the light scattering surface, e.g., for estimates of the average size of particles. It should be stressed that the observations of the Moon's ashen glow, if they are made from the Earth, always correspond to the near-zero lunar phase angle (a strictly zero phase angle is not achieved, because the Earth has an angular diameter of about 2° when viewed from the Moon). Thus, even ordinary images of lunar regions in ashen glow are of great interest, since they depict the albedo distribution close to the normal one. Such data can potentially give information about the variations of the amplitude of the opposition effect over the lunar surface.

6. Conclusion

Thus, optical measurements of the Moon are an effective tool to study its surface, as they allow one to identify the physical and chemical/mineral properties of the material of the lunar surface.

We have reviewed many optical studies of the Moon and modern results, emphasizing their diagnostic aspects. We summarize the main points of the overview:

1. Absolute lunar photometry aims to refine the albedo scale. The absolute calibration is essential when comparing the results of ground-based, space-born investigations with data obtained from laboratory measurements of lunar soils. Currently there is noticeable discrepancy between the ROLO (Kieffer and Stone, 2005) and Kharkov (Velikodsky et al., 2011; <http://astrodatal.univer.kharkov.ua/moon/albedo/>) independent systems, though they produce similar normalized phase curves. Meanwhile, the Kharkov data are in excellent agreement with Saiki et al. (2008) absolute measurements.
2. A very promising new tool to study the lunar surface is phase-ratio imagery that allows the determination of regolith structure variations. For instance, disturbances of regolith structure were found at the landing sites of the *Apollo* expeditions using the *LRO* NAC images (Kaydash et al., 2011). The phase-ratio approach is potentially very useful to study resurfacing processes on the Moon, such as soil creeps, debris/rock streams, taluses, etc.
3. It was possible to perform simultaneous mapping of several parameters of the lunar photometric function with a large series of calibrated observations of the Moon, which correspond to different phase angles. Unfortunately, our attempt to map the Hapke parameters of the lunar nearside is not encouraging. We recommend the use of the simple model presented by Eq. (23), which provides a good fit for experimental data, excluding very small phase angles, where a more complicated phase function is needed like that presented by formula (22).
4. Our analysis of opposition-effect data (see, e.g., Fig. 10) shows that, excepting the brightest lunar areas measured in NIR, the coherent-backscattering effect hardly influences the lunar opposition spike, because of the low albedo of the lunar surface. This conclusion somewhat contradicts to the extensive experiments of B. Hapke and R. Nelson (Hapke et al., 1993, 1998) with the circular polarization ratio that increases for *Apollo* lunar samples as the phase angle decreases at $\alpha < 10^\circ$. However, we note that the same increase can be found in calculations of single scattering by rather small particles of irregular shapes (Zubko et al., 2008; Mishchenko et al., 2009a,b). These results are entirely confirmed with our Sh-matrix calculations that soon will be published for particles of random shapes (e.g., Petrov et al., 2006, 2007, 2011).
5. It is necessary to understand the reasons for the contradiction between laboratory (see Fig. 15) and telescopic measurements of the phase dependence of color ratio: a minimum is observed in the phase curves of some samples near 10° . This has not yet been reliably detected in the data of either ground-based or space-borne colorimetric observations of the Moon. While some mare samples reveal this minimum, the highland (i.e., brighter) regolith from the *Luna-20* landing site has no it. This contradicts to the coherent backscattering origin of the effect.
6. Recently, there was proposed a new promising photoclinometry technique (Korokhin et al., 2010) that is based on the analysis of many calibrated images of the same scenes acquired at different phase angles: for each point of the lunar surface, a phase curve of the equigonal albedo can be plotted. Then the standard deviation of the observed $A_{eq}(\alpha)$ from a model phase function (see, e.g., Eq. (22)) are numerically minimized varying simultaneously surface slopes, albedo A_n , and the parameters of the model phase function. Korokhin et al. (2010) have successfully used the obtained telescopic photoclinometric data to search for artifacts in the *Kaguya* LALT map of the same resolution.
7. Optical spectrophotometry remains a principal method in remote sensing of the Moon. In particular, spacecraft and Earth-based spectral measurements of rather high spectral resolution, combined with laboratory spectral studies of analogs of lunar surface minerals allow a determination of unusual mineral composition. For instance, a high abundance of crystalline olivine (Pieters, 1982) and plagioclase (Matsunaga et al., 2008) is found in the peaks of several large craters; moreover, a small area was found with spinel-rich composition (Pieters et al., 2010, 2011; Sunshine et al., 2010).
8. Recently, compounds of OH/H₂O were discovered in superficial zones of lunar regolith grains using spectral measurements with different space crafts (Pieters et al., 2009a; Sunshine et al., 2009; Clark, 2009). This can be a result of the implantation of solar-wind hydrogen (Starukhina and Shkuratov, 2000). A significant problem in understanding the origin and evolution of detected OH/H₂O compounds is the correlation of the depth of the 3 μm band with surface insolation. An obvious prospect of these studies is global imagery with high spatial and spectral resolution in the NIR-IR range, say 1–5 μm. In other words, it is necessary to extend the *Chandrayaan-1* M³ spectral range up to 5 μm while preserving its spatial resolution.
9. A big problem is how to explain the relationship between the superficial and bulk water ice; the latter was found in permanently shadowed areas near the lunar poles by the *Lunar Prospector* and *LRO* neutron spectrometers. It does not seem impossible to assume that the OH/H₂O compounds are delivered to cold traps by electrostatically levitated dust that moves as the terminator shifts because of the lunar rotation. These particles being charged positively by electron photo-emission should deposit preferentially onto shadowed areas that have negative electric sign. Permanently shadowed areas are always charged negatively. Thus, depending of topography, they may be traps of the lunar dust. Submicron particles should be saturated by implanted hydrogen from the solar wind in full volume providing OH/H₂O compounds that may reach 10 wt% for anorthosite particles ~0.1 μm (ice-in-silicate model).
10. The available technique of the 3 μm band determination is still not perfect enough. This is valid in a first approximation for rather even surfaces at the thermal equilibrium. Near the lunar terminator the latter assumption does not hold, hence, Kirchhoff's law is perhaps violated. The lunar surface is rough in all scales. This produces the anisothermality effect (Bandfield et al., 2011) that may significantly influence the surface temperature determination. Additional important factor is multiple scattering of radiation between elements of roughness (Clark et al., 2011). Thus, the usually used technique of thermal emission removal is oversimplified and must be applied with caution.
11. Photometric imagery in several spectral bands in the Vis-NIR range allows chemical composition maps of the lunar surface. This relates to the chromophore elements, Fe and Ti. The content of other elements may be mapped too, if there are correlations between their abundance and the content of Fe and Ti. For calibration, different ground-truth data have been used, including *Clementine* UVVis spectral measurements of sampling sites (Lucey et al., 1995, 1998, 2000a), *Lunar Prospector* chemical measurements (Shkuratov et al., 2005a), and LSCC data (Shkuratov et al., 2003b). Significant problems arise with prognosis of TiO₂ content, as the correlation between this parameter and the color ratio C(750/415 nm) is very non-linear and, perhaps, is not universal for different

- composition types of the lunar surface (Gillis et al., 2003; Korokhin et al., 2008). A promising way to resolve this problem is to use color-ratio shifts to the UV spectral range (Robinson et al., 2007, 2011).
12. By analog with the prognosis of chemical composition, mineral-content imagery is also feasible (Lucey, 2004; Shkuratov et al., 2005b; Pieters et al., 2006; Cahill et al., 2009, 2010; Yan et al., 2010). Mineral maps are constructed using direct correlations between spectral parameters and mineral content (Shkuratov et al., 2005b; Pieters et al., 2006) established with samples of the lunar regolith. The technique developed in Lucey (2004), Cahill et al. (2009, 2010) and Yan et al. (2010) uses the Hapke scattering model that potentially may produce problems in prognosis that are related to the model's drawbacks. Therefore, straightforward methods, like direct correlations, seem to be preferable.
 13. With the calibration dependencies, like (47)–(49), one may use the data on the lunar colorimetry in the Vis–NIR spectral range for prognoses of the degree of lunar soil maturity. There are several different parameters of maturity. Three of them – the maturity degree I_s/FeO , agglutinate content, and optical maturity parameter OMAT – have been compared. These three distributions are fairly similar, though important differences also are observed. For instance, the correlation between I_s/FeO and agglutinate content has two branches corresponding to the mare/highland division (Shkuratov et al., 2007a). One of the reasons for the discrepancy could be different melting temperatures of mare and highland materials.
 14. The ${}^3\text{He}$ content of the lunar regolith from the data of optical measurements can be roughly estimated. This is based on the results by Taylor (1994), who from laboratory measurements found that the concentration of ${}^3\text{He}$ in the regolith is closely correlated with the parameter $[\text{TiO}_2 \cdot I_s/\text{FeO}]$ representing the content of titanium dioxide and the regolith maturity. An attempt to map the ${}^3\text{He}$ concentration using the distributions of the TiO_2 content and the I_s/FeO parameter determined from optical observations of the lunar visible hemisphere was reported in Shkuratov et al. (1999c). The map of the ${}^3\text{He}$ concentration and the map of the thickness of the regolith layer (Shkuratov and Bondarenko, 2001) allow estimates of the amount of the isotope ${}^3\text{He}$ that can be extracted from 1 m² of the lunar regolith.
 15. Although the first images of the lunar surface areas in three polarimetric parameters, P_{min} , α_{inv} , and h have been obtained (Shkuratov et al., 2008; Opanasenko et al., 2009), their interpretation is still not sufficiently developed. The depth of the negative polarization branch, which varies over the lunar surface from 0.2% to 1.6%, may depend on the degree of the optical heterogeneity of the regolith material (Shkuratov, 1987). This potentially may allow remote estimates of the albedo contrast degree for the light- and dark-colored components of lunar soil. Unfortunately, by now, variations of $|P_{min}|$ only offer a hope to be interpreted; the diagnostic use of other parameters of the negative polarization branch is also unclear.
 16. The negative polarization of the Moon at small phase angles is perhaps generated with single-particle scattering (e.g., Shkuratov et al., 2004, 2006). The mechanism of the negative branch for single particles is not evident and cannot be explained simply. One may say that this branch results from the interference of electromagnetic waves multiply scattered within particles, but this is not informative. The role of the coherent backscattering enhancement in the formation of the lunar negative polarization branch at scattering between particles perhaps is not significant. A number of experimental results (e.g., Figs. 9, 10, and 15) have shown that this enhancement may not be important even for the lunar brightness opposition effect.
 17. In the investigations of positive polarization, it seems worthwhile to construct images depicting the distribution of the parameter that characterizes deviations from the regression line of the albedo–polarization degree correlation. This parameter is related to sizes of particles of the lunar surface. However, it must be emphasized that there are uncertainties both in calibrating the laboratory determination of average particle size of the lunar regolith and the shortage of the observational data.

Acknowledgment

The authors gratefully acknowledge the research support from NASA grant NNX11AB25G Lunar Advanced Science and Exploration Research (LASER), "Imaging photometric and polarimetric remote sensing of the Moon". We are grateful to Mr. Frank Wang and Ms. Lu Yang who being the Publishing Content Coordinators for Planetary and Space Science invited us to prepare this review article. We also thank the reviewers for remarks; especially, we are grateful to Bruce Hapke for his patience at reading this long manuscript and thoughtful discussion.

References

- Adams, J.B., 1974. Visible and near-infrared diffuse reflectance spectra of pyroxenes as applied to remote sensing of solid objects in the Solar system. *J. Geophys. Res.* 79 (32), 4829–4836.
- Adams, J.B., McCord, T.B., 1971. Alteration of lunar optical properties: age and composition effects. *Science* 171, 567–571.
- Adams, J.B., Horz, F., Gibbons, R.V., 1979. Effects of shock-loading on the reflectance spectra of plagioclase, pyroxene, and glass. *Lunar Planet. Sci. Conf.* 10th, LPI, Houston, pp. 1–3.
- Akhmanova, M.V., Dement'ev, B.V., Markov, M.N., Sushchinsky, M.M., 1973. Infrared reflection characteristics of lunar mare regolith. *Space Res.* XIII 2, 965–967.
- Akimov, L.A., 1976. Influence of mesorelief on the brightness distribution over a planetary disk. *Sov. Astron.* 19 (3), 385–388.
- Akimov, L.A., 1979a. Brightness distribution over the lunar and planetary disks. *Astron. Zh.* 56, 412–418.
- Akimov, L.A., Antipova-Karataeva, I.I., Shkuratov, Y.G., 1979b. Indicatrix measurements of lunar samples from landing sites of Luna 24, Luna 16, and Luna 20. *Lunar Planet. Sci. Conf.* 10th, LPI, Houston, pp. 9–11.
- Akimov, L.A., 1988a. Light reflection by the Moon, I. *Kinem. Phys. Celest. Bodies* 4 (1), 3–10.
- Akimov, L.A., 1988b. Light reflection by the Moon, II. *Kinem. Phys. Celest. Bodies* 4 (2), 10–16.
- Akimov, L.A., Shkuratov, Y.G., 1981. The distribution of the brightness phase gradient over the lunar surface in two spectral bands. *Preliminary Investigations. Astron. Tsirk.*, GAIsh Moscow 1167, 3–6.
- Akimov, L.A., Velikodsky, Y.I., Korokhin, V.V., 1999. Dependence of lunar highland brightness on photometric latitude. *Kinem. Phys. Celest. Bodies* 15 (4), 232–236.
- Akimov, L.A., Velikodsky, Y.I., Korokhin, V.V., 2000. Dependence of latitudinal brightness distribution over the lunar disk on albedo and surface roughness. *Kinem. Phys. Celest. Bodies* 16 (2), 137–141.
- Anand, M., 2010. Lunar water: a brief review. *Earth Moon Planets* 107 (1), 65–73.
- Andersson, S., van Dishoeck, E.F., 2008. Photodesorption of water ice: a molecular dynamics study. *Astron. Astrophys.* 491, 907–916.
- Araki, H., Tazawa, S., Noda, H., Ishihara, Y., Goossens, S., Sasaki, S., Kawano, N., Kamiya, I., Otake, H., Oberst, J., Shum, C., 2009. Lunar global shape and polar topography derived from Kaguya-LALT laser altimetry. *Science* 323, 897–900.
- Arnold, J.R., 1979. Ice in the lunar polar regions. *J. Geophys. Res.* 84, 5659–5668.
- Azzam, R., Bashara, N., 1977. *Ellipsometry and Polarized Light*. Elsevier, North-Holland (529 pp.).
- Bandermann, L.W., Kemp, L.C., Wolstenholme, R.D., 1972. Circular polarization of light scattered from rough surfaces. *Mon. Not. R. Astron. Soc.* 158 (3), 291–304.
- Bandfield, J.L., Hayne, P.O., Ghent, R.R., Greenhagen, B.T., Paige, D.A., 2011. Lunar surface roughness and anisothermality effects on infrared measurements. *Lunar Planet. Sci. Conf.*, LPI, Houston, #2468.
- Bell, J.F., Hawke, B.R., 1981. The Reiner gamma formation: composition and origin as derived from remote sensing observations. *Proc. Lunar Planet. Sci. Conf.* 12th, pp. 679–694.
- Belskaya, I.N., Barucci, A.M., Shkuratov, Yu.G., 2003. Opposition effect of Kuiper belt objects: preliminary estimation. *Earth Moon Planets* 92, 201–206.

- Blewett, D.T., Lucey, P.G., Hawke, B.R., Jolliff, B.L., 1997. Clementine images of the lunar sample-return stations: refinement of FeO and TiO₂ mapping techniques. *J. Geophys. Res.* 102, 16,319–16,325.
- Blewett, D.T., Hughes, C.G., Hawke, B.R., Richmond, N.C., 2007. Varieties of the lunar swirls. *Lunar Planet. Sci. Conf.* 38th, Abstract no. 1232, LPI, Houston, USA.
- Bohren, C.F., Huffman, D.R., 2004. Absorption and Scattering of Light by Small Particles. Wiley-VCH Verlag GmbH & Co (530 pp).
- Buratti, B.J., Hiller, J.K., Wang, M., 1996. The lunar opposition surge: observation by *Clementine*. *Icarus* 124, 490–499.
- Buratti, B.J., Hicks, M.D., Nettles, J., Staid, M., Pieters, C.M., Sunshine, J., Boardman, J., Stone, T.C., 2011. A wavelength dependent visible and infrared spectrometric function for the Moon on ROLO data. *J. Geophys. Res., Planets*. doi:10.1029/2010JE003724.
- Burns, R., 1993. Mineralogical Applications of Crystal Field Theory. Cambridge University Press 459 pp.
- Cadenhead, D., Brown, M., Rice, D., Stetter, J., 1977. Some surface area and porosity characterization of lunar soils. *Lunar Planet. Sci. Conf.* 8th, LPI, Houston, USA, pp. 1291–1303.
- Cahill, J.T.S., Lucey, P.G., Wieczorek, M.A., 2009. The compositional variations of the lunar crust: results from radiative transfer modeling of central peak spectra. *J. Geophys. Res.* 114 (E9). doi:10.1029/2008JE003282.
- Cahill, J.T.S., Lucey, P.G., Stockstill-Cahill, K.R., Hawke, B.R., 2010. Radiative transfer modeling of near-infrared reflectance of lunar highland and mare soils. *J. Geophys. Res., Planets* 115, E12021. doi:10.1029/2010JE003602.
- Charette, M.P., McCord, T.B., Pieters, C.M., Adams, J.B., 1974. Application of remote spectral reflectance measurements to lunar geology classification and determination of titanium content of lunar soils. *J. Geophys. Res.* 79 (11), 1605–1613.
- Chen, C.-Y., Klette, R., Kakarala, R., 2002. Albedo recovery using photometric stereo approach. In: Proceedings of the 16th International Conference on Pattern Recognition (ICPR'02), vol. 3, Quebec, Canada, August 2002, pp. 700–703.
- Clark, R.N., 2009. Detection of adsorbed water and hydroxyl on the Moon. *Science* 326, 562–564.
- Clark, R.N., Pieters, C.M., Green, R.O., Boardman, J.W., Petro, N.E., 2011. Thermal removal from near-infrared imaging spectroscopy data of the Moon. *J. Geophys. Res., Planets* 10.1029/2010JE003751.
- Cloutis, E.A., Gaffey, M.J., 1993. Lunar regolith analogues: spectral reflectance properties of compositional variations. *Icarus* 102, 203–224.
- Cloutis, E.A., Sunshine, J.M., Morris, R.V., 2004. Spectral reflectance-compositional properties of spinels and chromites: implications for planetary remote sensing and geothermometry. *Meteorit. Planet. Sci.* 39 (4), 545–565.
- Cloutis, E., Klima, R., Kaledzka, L., Coradini, A., Golubeva, L., McFadden, L., Shestopalov, D., Vilas, F., 2010. The 506 nm absorption feature in pyroxene spectra: nature and implications for spectroscopy-based studies of pyroxene-bearing targets. *Icarus* 207, 295–313.
- Cocks, F.H., 2010. ³He in permanently shadowed lunar polar surfaces. *Icarus* 206, 778–779.
- Colaprete, A., 16 colleagues, 2010. Detection of water in the LCROSS ejecta plume. *Science* 330 (6003), 463–468.
- Cook, A.C., Robinson, M.S., 2000. Mariner 10 stereo image coverage of Mercury. *J. Geophys. Res.* E 105 (4), 9429–9444.
- Crider, D.H., Vondrak, R.R., 2002. Hydrogen migration to the lunar poles by solar wind bombardment of the Moon. *Adv. Space Res.* 30 (8), 1869–1874.
- Criswell, D., 1972. Lunar dust motion. *Lunar Planet. Sci. Conf.* 3rd, LPI, Houston, USA, pp. 2671–2680.
- Davies, D.W., Johnson, T.V., Matson, D.L., 1979. Lunar multispectral mapping at 2.26 μm: first result. *Lunar Planet. Sci. Conf.* 10th, LPI, Houston, USA, pp. 1819–1828.
- Degtyarev, V., Kolokolova, L., 1992. Possible application of circular polarization for remote sensing of cosmic bodies. *Earth Moon Planets* 57, 213–223.
- Denevi, B.W., Robinson, M.S., Hapke, B.W., Lawrence, S.J., Wiseman, S.M., Jolliff, B.L., and the LROC Team, 2010. Global ultraviolet through visible color observations of the Moon with the lunar reconnaissance orbiter wide angle camera. *Lunar Planet. Sci. Conf.* 41st, No. 2263, LPI, Houston, USA.
- Dollfus, A., 1962. The polarization of moonlight. In: Kopal, Z. (Ed.), Physics and Astronomy of the Moon. Academic Press, pp. 131–139 (Chapter 5).
- Dollfus, A., Bowell, E., 1971. Polarimetric properties of the lunar surface and interpretation. I. Telescope observation. *Astron. Astrophys.* 10, 29–53.
- Dollfus, A., 1998. Lunar surface imaging polarimetry: 1-μm roughness and grain size. *Icarus* 136, 69–103.
- Dyar, M.D., Hibbitts, C.A., Orlando, T.M., 2010. Mechanisms for incorporation of hydrogen in and on terrestrial planetary surfaces. *Icarus* 208, 425–437.
- Eberhardt, P., Geiss, J., Graf, H., 1970. Trapped solar wind noble gases, exposure age and K/Ar-Age in *Apollo* 11 lunar fine material. *Apollo 11 Lunar Planet. Sci. Conf.*, LPI, Houston, USA, pp. 1037–1070.
- Eke, V.R., Teodoro, L.F.A., Elphic, R.C., 2009. The spatial distribution of polar hydrogen deposits on the Moon. *Icarus* 200, 12–18.
- Eliason, E.M., McEwen, A.S., Robinson, M.S., Lee, E.M., Becker, T.L., Gaddis, L., Weller, L.A., Isbell, C.E., Shinaman, J.R., Duxbury, T., Malaret, E., 1999. Clementine: A global multi-spectral map of the Moon from the Clementine UVVIS imaging instrument. *Lunar Planet. Sci. Conf.* 30th, LPI, Houston, USA, pp. 1933–1934.
- Elphic, R.C., Eke, V.R., Teodoro, L.F.A., Lawrence, D.J., Bussey, D.B.J., 2007. Models of the distribution and abundance of hydrogen at the lunar south pole. *Geophys. Res. Lett.* 34, L13204.
- Elphic, R.C., Paige, D.A., Siegler, M.A., Vasavada, A.R., Eke, V.R., Teodoro, L.F.A., Lawrence, D.J., 2010. South pole hydrogen distribution for present lunar condition: implication. In: Proceedings of the 41st Lunar and Planetary Science, no. 2732, LPI, Houston, USA.
- Engelhardt, W., Hurle, H., Luft, E., 1976. Microimpact-induced changes of textural parameters and modal composition of the lunar regolith. *Lunar Planet. Sci. Conf.* 7th, LPI, Houston, USA, pp. 373–392.
- Evsyukov, N.N., 1973a. Albedo Map for the Visible Hemisphere of the Moon. Naukova Dumka, Kiev.
- Evsyukov, N.N., 1973b. Color Map of the Visible Hemisphere of the Moon. Naukova Dumka, Kiev.
- Zhe, Fa Wen, Qiu, Jin Ya, 2010. Global inventory of helium-3 in lunar regoliths estimated by a multi-channel microwave radiometer on the Chang-E1 lunar satellite. *Chin. Sci. Bull.* 55 (35), 4005–4009.
- Farrell, W., Killen, R., Vondrak, R., Hurley, D., Stubbs, T.J., Delory, G., Halekas, J., 2011. Could lunar polar ice be a “fountain” source for the dayside water veneer? *Lunar Planet. Sci. Conf.* 42nd, #1770, LPI, Houston.
- Feldman, W.C., Lawrence, D.J., Elphic, R.C., Barraclough, B., Maurice, S., Genetay, I., Binder, A.B., 2000. Polar hydrogen deposits on the Moon. *J. Geophys. Res.* 105 (E2), 4175–4195.
- Feldman, W.C., Maurice, S., Lawrence, D.J., Little, R.C., Lawson, S.L., Gasnault, O., Wiens, R.C., Barraclough, B.L., Elphic, R.C., Prettyman, T.H., Steinberg, J.T., Binder, A.B., 2001. Evidence for water ice near the lunar poles. *J. Geophys. Res.* 106, 23231–23252.
- Fox, G.K., Code, A.D., Anderson, C.M., Babler, B.L., Bjorkman, K.S., Johnsos, J.J., Maede, M.R., Nordsieck, K.H., Weitenbeck, A.J., Zellner, N.E.B., 1998. Solar system observations by the Wisconsin Ultraviolet Photopolarimeter Experiment—III: the first ultraviolet spectropolarimetry of the Moon. *Mon. Not. R. Astron. Soc.* 298, 303–309.
- Gaffey, M.J., 2010. Space weathering and the interpretation of asteroid reflectance spectra. *Icarus* 209 (2), 564–574.
- Galilei, G., 1638. Dialogue of the Great World Systems (trans. G. De Santillana, 1953). Chicago University Press, Chicago.
- Garrick-Bethell, I., Head, J.W., Pieters, C.M., 2011. Spectral properties, magnetic fields, and dust transport at lunar swirls. *Icarus*. doi:10.1016/j.icarus.2010.11.036.
- Garvin, J.B., Robinson, M.S., Hapke, B., Bell, J.F., Skillman, D., Ulmer, M., Pieters, C., 2006. UV imaging of the Moon from the Hubble Space Telescope. *Lunar Planet. Sci. Conf.* 37th, no. 2100, LPI, Houston, USA.
- Gehrels, T., Coffen, T., Owings, D., 1964. Wavelength dependence of polarization. III. The lunar surface. *Astron. J.* 69 (10), 826–852.
- Gibson, E.K., Johnson, S.M., 1971. Thermal analysis—inorganic gas release studies of lunar samples. *Lunar Planet. Sci. Conf.* 2nd, LPI, Houston, USA, pp. 1351–1366.
- Gillis, J., Jollif, B., Elphic, R., 2003. A revised algorithm for calculating TiO₂ from Clementine UVVis data: a synthesis of rock, soil, and remotely sensed TiO₂ concentrations. *J. Geophys. Res.* 108 (E2).
- Gladstone, G., 19 colleagues, 2010. LRO-LAMP observations of the LCROSS impact plume. *Science* 330 (6003), 472–476.
- Goguen, J.D., Stone, T.C., Kieffer, H., Buratti, B.J., 2010. A new look at photometry of the Moon. *Icarus* 208, 548–557.
- Grynk, E.S., Shkuratov, Y.G., 2002. The scattering matrix of transparent particles of random shape in the geometrical optics approximation. *Opt. Spectrosc.* 93 (6), 885–893.
- Grynk, E., Shkuratov, Yu., 2003. Scattering matrix for semitransparent particles of different shapes in geometric optics approximation. *J. Quant. Spectrosc. Radiat. Trans.* 78 (3–4), 319–340.
- Grundy, W., Doute, S., Schmitt, B., 2000. A Monte Carlo ray-tracing model for scattering and polarization by large particles with complex shapes. *J. Geophys. Res.* 105, 29,290–29,314.
- Hapke, B., 1971. Optical properties of the lunar surface. In: Kopal, Z. (Ed.), Physics and Astronomy of the Moon. Academic Press, New York, pp. 155–211.
- Hapke, B., 1993. Theory of Reflectance and Emissivity Spectroscopy. Cambridge University Press, Cambridge (450 pp).
- Hapke, B., 2001. Space weathering from Mercury to the asteroid belt. *J. Geophys. Res.* 106, 10,039–10,073.
- Hapke, B., 2002. Bidirectional reflectance spectroscopy. 5. The coherent backscatter opposition effect and anisotropic scattering. *Icarus* 157, 523–534.
- Hapke, B., 2008. Bidirectional reflectance spectroscopy, 6: effects of porosity. *Icarus* 195, 918–926.
- Hapke, B., Cassidy, W., Wells, E., 1975. Effects of vapor-phase deposition processes on the optical, chemical and magnetic properties of the lunar regolith. *Moon* 13, 339–353.
- Hapke, B., Nelson, R., Smith, W., 1993. The opposition effect of the Moon: the contribution of coherent backscatter. *Science* 260, 509–511.
- Hapke, B., Nelson, R., Smith, W., 1998. The opposition effect of the Moon: coherent backscatter and shadow hiding. *Icarus* 133, 89–97.
- Hapke, B., Denevi, B., Sato, H., Robinson, M., 2011. The opposition effect of the Moon as seen by the Lunar Reconnaissance Orbiter wide angle camera. *Lunar Planet. Sci. Conf.* 42nd, #1080, LPI, Houston.
- Harris, A., 12 colleagues, 1989. Phase relations of high albedo asteroids: the unusual opposition brightening of 44 Nysa and 64 Angelina. *Icarus* 81, 365–374.
- Haruyama, J., 18 colleagues, 2008. Lack of exposed ice inside lunar south pole Shackleton crater. *Science* 322 (5903), 938–939.

- Haruyama, J., Morota, T., Shirao, M., Hiesinger, H., van der Bogert, C.H., Pieters, C.M., Lucey, P.G., Ohtake, M., Nishino, M., Matsunaga, T., Yokota, Y., Miyamoto, H., Iwasaki, A., 2011. Water in lunar holes? *Lunar Planet. Sci. Conf.* 42nd, #1134.
- Haskin, L., Warren, P., 1991. Lunar chemistry. In: Heiken, G.H., Vaniman, D.T., French, B.M. (Eds.), *Lunar Sourcebook*. Cambridge University Press, Cambridge, pp. 357–474 (Chapter 8).
- Hauri, E.H., Weinreich, T., Saal, A.E., Rutherford, M.C., Van Orman, J.A., 2011. High pre-eruptive water contents preserved in lunar melt inclusions. *Science*. doi:10.1126/science.1204626.
- Hawke, B.R., Coombs, C.R., Clark, B., 1990. Ilmenite-rich pyroclastic deposits: An ideal lunar resource. *Lunar Planet. Sci. Conf.* 20th, LPI, Houston, USA, pp. 249–258.
- Hawke, B.R., Peterson, C.A., Blewett, D.T., Bussey, D.B.J., Lucey, P.G., Taylor, G.J., Spudis, P.D., 2003. Distribution and modes of occurrence of lunar anorthosite. *J. Geophys. Res.* 108 (E6), 5050. doi:10.1029/2002JE001890.
- Helfenstein, P., Veverka, J., 1987. Photometric properties of lunar terrains derived from Hapke's equation. *Icarus* 72, 342–357.
- Helfenstein, P., Veverka, J., Hillier, J., 1997. The lunar opposition effect: a test of alternative models. *Icarus* 128, 2–14.
- Henry, R.C., Fastie, W.M., Lucke, R.L., Hapke, B.W., 1976. A far-ultraviolet photometer for planetary surface analysis. *Moon* 15, 51–65.
- Henry, R.C., Feldman, P.D., Kruk, J.W., Davidsen, A.F., Durrance, S.T., 1995. Ultraviolet albedo of the Moon with the Hopkins ultraviolet telescope. *Astrophys. J.* 454, L69–L72.
- Herrick, R.R., Sharpton, V.L., 2000. Implications from stereo-derived topography of Venusian impact craters. *J. Geophys. Res. E* 105 (8), 20,245–20,262.
- Hicks, M.D., Buratti, B.J., Staid, M., Pieters, C., Nettles, J., Boardman, J.W., Sunshine, J., 2010. A Visible and infrared spectrophotometric model for the Moon based on ROLO and Chandrayaan-1 Moon Mineralogical Mapper Data. *Lunar Planet. Sci. Conf.* 41st, No. 2076, LPI, Houston, USA.
- Hicks, M.D., Buratti, B.J., Nettles, J., Staid, M., Sunshine, J.M., Pieters, C.M., Besse, S., Boardman, J.W., 2011. A photometric function for analysis of lunar images in the visual and infrared based on Moon Mineralogy Mapper observations. *J. Geophys. Res., Planets*. doi:10.1029/2010JE003733.
- Hillier, J.K., Buratti, B.J., Hill, K., 1999. Multispectral photometry of the Moon and absolute calibration of the Clementine UV/Vis camera. *Icarus* 141, 205–225.
- Housley, R.M., Grant, R.W., Paton, N.E., 1973. Origin and characteristics of excess Fe metal in lunar glass welded aggregates. *Lunar Planet. Sci. Conf.* 4th, LPI, Houston, USA, pp. 2737–2749.
- Immer, C., Metzger, P., Hintze, P., Nick, A., Horan, R., 2011. Apollo 12 Lunar Module exhaust plume impingement on Lunar Surveyor III. *Icarus* 211 (2), 1089–1102.
- Isaacson, P.J., Pieters, C.M., 2010. Deconvolution of lunar olivine reflectance spectra: implications for remote compositional assessment. *Icarus* 210, 8–13.
- James, C., Letsinger, S., Basu, A., Wentworth, S., McKay, D., 2002. Size distribution of Fe⁰ globules in lunar agglutinitic glass. *Lunar Planet. Sci. Conf.* 33rd, Abstract no. 1827, LPI, Houston, USA.
- Johnson, J.R., Larson, S.M., Singer, R.B., 1991a. Remote sensing of potential lunar resources. 1. Nearside compositional properties. *J. Geophys. Res.* 96, 18861–18882.
- Johnson, J.R., Larson, S.M., Singer, R.B., 1991b. A re-evaluation of spectral ratios for lunar mare TiO₂ mapping. *Geophys. Res. Lett.* 18 (11), 2153–2156.
- Johnson, J., Swindle, T., Lucey, P., 1999. Estimated solar wind-implanted helium-3 distribution on the Moon. *Geophys. Res. Lett.* 26, 385–388.
- Kaydash, V.G., Gerasimenko, S.Y., Shkuratov, Y.G., Opanasenko, N.V., Velikodskii, Y.I., Korokhin, V.V., 2009a. Photometric function variations observed on the near side of the Moon: mapping. *Sol. Syst. Res.* 43 (2), 89–99.
- Kaydash, V., Kreslavsky, M., Shkuratov, Yu., Gerasimenko, S., Pinet, P., Josset, J.-L., Beauvivre, S., Foing, B., the AMIE SMART-1 Team, 2009b. Photometric anomalies of the lunar surface studied with SMART-1 AMIE data. *Icarus* 202 (2), 393–413.
- Kaydash, V.G., Gerasimenko, S.Y., Shkuratov, Y.G., Opanasenko, N.V., Velikodskii, Y.I., Korokhin, V.V., 2010. Mapping of phase ratio of color index for two areas of the lunar nearside. *Sol. Syst. Res.* 44 (4), 267–280.
- Kaydash, V., Shkuratov, Y., Korokhin, V., Videen, G., 2011. Photometric anomalies in the Apollo landing sites as seen from the Lunar Reconnaissance Orbiter. *Icarus* 211, 89–96.
- Keller, L.P., McKay, D.S., 1993. Discovery of vapor deposits in the lunar regolith. *Science* 261 (5126), 1305–1307.
- Kemp, J.C., Wolstencroft, R.D., Swedling, J.B., 1971. Circular polarization: Jupiter and other planets. *Nature* 232, 165–168.
- Kemp, G.C., Henson, G.D., Steiner, C.T., Powell, E.R., 1987. The optical polarization of the sun measured at a sensitivity of parts in ten million. *Nature* 326 (6110), 270–273.
- Kennelly, E.J., Price, S.D., Kraemer, K.E., Aschbrenner, R., 2010. Calibration against the Moon. I. A disk-resolved lunar model for absolute reflectance calibration. *Icarus* 210, 14–36.
- Kieffer, H.H., Wildey, R.L., 1996. Establishing the Moon as a spectral radiance standard. *J. Atmos. Oceanic Technol.* 13, 360–375.
- Kieffer, H.H., Stone, T., 2005. The spectral irradiance of the Moon. *Astron. J.* 129, 2887–2901.
- Killen, R.M., Benkhoff, J., Morgan, T.H., 1997. Mercury's Polar Caps and the generation of an OH exosphere. *Icarus* 125, 195–211.
- Klima, R.L., Pieters, C.M., Dyar, M.D., 2007. Spectroscopy of synthetic Mg–Fe pyroxenes I: spin-allowed and spin-forbidden crystal field bands in the visible and near-infrared. *Meteorit. Planet. Sci.* 42, 235–253.
- Klumov, B.A., Berezhnoi, A.A., 2002. Possible origin of lunar ice. *Adv. Space Res.* 30 (8), 1875–1881.
- Korokhin, V., Akimov, L., 1997. Mapping of phase parameters of the lunar-surface brightness. *Sol. Syst. Res.* 31 (2), 128–136.
- Korokhin, V.V., Velikodskiy, Y.I., 2005. Parameters of the positive polarization maximum of the Moon: mapping. *Sol. Syst. Res.* 39 (1), 45–53.
- Korokhin, V.V., Velikodskiy, Y.I., Shkuratov, Y.G., Mall, U., 2007. The phase dependence of brightness and color of the lunar surface: a study based on integral photometric data. *Sol. Syst. Res.* 41 (1), 19–27.
- Korokhin, V.V., Kaydash, V.G., Shkuratov, Y.G., Stankevich, D.G., Mall, U., 2008. Prognosis of TiO₂ abundance in lunar soil using a non-linear analysis of Clementine and LSSC data. *Planet. Space Sci.* 56 (8), 1063–1078.
- Korokhin, V.V., Velikodskiy, Y.I., Shkuratov, Y.G., Kaydash, V.G., Gerasimenko, S.Y., Opanasenko, N.V., Videen, G., Pieters, C., 2010. Removal of topographic effects from lunar images using Kaguya (LALT) and telescope observations. *Planet. Space Sci.* 58, 1298–1306.
- Kramer, G., Combe, J.-P., McCord, T., Pieters, C., Head, J., Taylor, L., Staid, M., 2010. Colorful views of the Moon: comparing spectra from Clementine and the Moon Mineralogy Mapper. *Lunar Planet. Sci. Conf.* 41st, Abstract no. 2338, LPI, Houston, USA.
- Kuga, Y., Ishimaru, A., 1984. Retroreflectance from a dense distribution of spherical particles. *J. Opt. Soc. Am. A1* (8), 831–835.
- Kreslavsky, M.A., Shkuratov, Y.G., 2003. Photometric anomalies of the lunar surface: Results from Clementine data. *J. Geophys. Res.*, 108. doi:10.1029/2002JE001937 5015.
- Kreslavsky, M.A., Shkuratov, Y.G., Velikodskiy, Y.I., Kaydash, V.G., Stankevich, D.G., Pieters, C.M., 2000. Photometric properties of the lunar surface derived from Clementine observations. *J. Geophys. Res.* 105 (E8), 20,281–20,296.
- Kreslavsky, M.A., Shkuratov, Yu.G., Kaydash, V.G., Omelchenko, V.V., Blewett, D.T., Lucey, P.G., 2001. Lunar opposition spike observed by Clementine NIR camera: preliminary results. *Lunar Planet. Sci. Conf.* 32nd, Abstract no. 1140, LPI, Houston, USA.
- Kvaratskheliya, O.I., 1988. Spectropolarimetry of the lunar surface and samples of the lunar soil. *Bull. Abastumani. Astrophys. Obs.* 64, 1–312.
- Lane, A.L., Irvine, W.M., 1973. Monochromatic phase curves and albedos for the lunar disk. *Astron. J.* 78 (3), 267–277.
- Lanzerotti, L.J., Brown, W.L., Johnson, R.E., 1981. Ice in the polar regions of the Moon. *J. Geophys. Res.* 86, 3949–3950.
- Lawrence, D.J., Feldman, W.C., Elphic, R.C., Hagerty, J.J., Maurice, S., McKinney, G.W., Prettyman, T.H., 2005. Improved modeling of Lunar Prospector neutron spectrometer data: Implications for hydrogen deposits at the lunar poles. *J. Geophys. Res.*, 111. doi:10.1029/2005JE002637.
- Le Mouelic, S., Langevin, Y., Erard, S., Pinet, P., Daydou, Y., Chevrel, S., 2000. Discrimination between maturity and composition of lunar soils from integrated Clementine UVVIS-NIR data: Application to Aristarchus Plateau. *J. Geophys. Res.* 105, 9445–9455.
- Li, L., 2008a. Quantifying lunar soil composition with partial least squares modeling of reflectance. *Adv. Space Res.* 42, 267–274.
- Li, L., 2008b. Partial least squares methods for spectrally estimating lunar soil FeO abundance: A stratified approach to revealing nonlinear effect and qualitative interpretation. *J. Geophys. Res.* 113, E12013. doi:10.1029/2008JE003213.
- Li, L., Lucey, P.G., 2009. Quantifying TiO₂ abundance of mare soils: a stratified partial least squares approach to qualitative interpretation. *Lunar Planet. Sci. Conf.* 40th, No. 2226, LPI, Houston, USA.
- Lipsky, Y.N., Pospergelis, M.M., 1967. Several results of measuring the complete Stokes vector for lunar surface features. *Astron. Zh.* 44, 410–412.
- Lord, H.C., 1968. Hydrogen and helium implantation into olivine and enstatite: Retention coefficients, saturation concentrations, and temperature-release profiles. *J. Geophys. Res.* 73, 5271–5280.
- Lucey, P.G., 2004. Mineral maps of the Moon. *Geophys. Res. Lett.* 31 (8), L08701. doi:10.1029/2003GL019406.
- Lucey, P.G., Taylor, G.I., Malaret, E., 1995. Abundance and distribution of iron on the Moon. *Science* 268, 1150–1153.
- Lucey, P., Blewett, D., Hawke, R., 1998. FeO and TiO₂ Concentrations in the South Pole-Aitken Basin: implication for mantle composition and basin formation. *J. Geophys. Res. (Planets)* 103, 3701–3708.
- Lucey, P.G., Blewett, D.T., Bradley, L.L., 2000a. Lunar iron and titanium abundance algorithm based on final processing of Clementine ultraviolet-visible images. *J. Geophys. Res.* 105, 20,297–20,305.
- Lucey, P.G., Blewett, D.T., Taylor, G.J., Hawke, B.R., 2000b. Imaging of the lunar surface maturity. *J. Geophys. Res.* 105, 20,377–20,386.
- Lumee, K., Bowell, E., 1981. Radiative transfer in the surfaces of atmosphereless bodies. I. Theory. *Astron. J.* 86 (11), 1694–1704.
- Lyot, B., 1929. Recherches sur la polarisation de la lumiere des planetes et de quelques substances terrestres. *Ann. Obs. Meudon* 8 (1), 1–161.
- Managadze, G.G., Cherepin, V.T., Shkuratov, Y.G., Kolesnik, V.N., Chumikov, A.E. Simulating OH/H₂O formation by solar wind at the lunar surface. *Icarus*, in press. doi:10.1016/j.icarus.2011.06.025.
- Matsunaga, T., 22 colleagues, 2008. Discoveries on the lithology of lunar crater central peaks by SELENE Spectral Profiler. *Geophys. Res. Lett.* 35, L23201. doi:10.1029/2008GL035868.
- Melosh, H., 1989. Impact Cratering: A Geologic Process. Oxford University Press, New York.
- Merlin, F., Barucci, M.A., de Bergh, C., Fornasier, S., Doressoundiram, A., Perna, D., Protopapa, S., 2010. Surface composition and physical properties of several

- trans-Neptunian objects from the Hapke scattering theory and Shkuratov model. *Icarus* 208, 945–954.
- McCord, T.B., 1969. Color differences on the lunar surface. *J. Geophys. Res.* 74 (12), 3131–3142.
- McCord, T.B., Charette, M.P., Johnson, T.V., Lebofsky, L.A., Pieters, C.M., Adams, J.B., 1972. Lunar spectral types. *J. Geophys. Res.* 77, 1349–1359.
- McCord, T.B., Pieters, C., Feiberg, M.A., 1976. Multispectral mapping of the lunar surface using ground based telescopes. *Icarus* 29, 1–34.
- McCord, T.B., Taylor, L.A., Combe, J.-Ph., Kramer, G., Pieters, C.M., Sunshine, J.M., Clark, R.N., 2011. Sources and physical processes responsible for OH/H₂O in the lunar soil as revealed by the Moon Mineralogy Mapper (M3). *J. Geophys. Res., Planets*. doi:10.1029/2010JE003711.
- McCoy, J.E., Criswell, D.R., 1974. Evidence for a high altitude distribution of lunar dust. *Lunar Planet. Sci. Conf.* 5th, LPI, Houston, USA, pp. 2991–3005.
- McCoy, J.E., 1976. Photometric studies of light scattering above the lunar terminator from Apollo solar corona photography. *Lunar Planet. Sci. Conf.* 7th, LPI, Houston, USA, pp. 1087–1112.
- McKay, D., Heiken, G., Basu, A., Blanford, G., 1991. The lunar regolith. In: Heiken, G.H., Vaniman, D.T., French, B.M. (Eds.), *Lunar Sourcebook*, 1991. Cambridge University Press, New York, pp. 285–356 (Chapter 7).
- McEwen, A.S., 1991. Photometric functions for photoclinometry and other applications. *Icarus* 92, 298–311.
- McEwen, A.S., 1996. A precise lunar photometric function. *Lunar Planet. Sci. Conf.* 27th, LPI, Houston, USA, pp. 841–842.
- McEwen, A.S., Eliason, E., Lucey, P., Malaret, E., Pieters, C., Robinson, M., Sucharski, T., 1998. Summary of radiometric calibration and photometric normalization steps for the Clementine UVVis Images. *Lunar Planet. Sci. Conf.* 27th, LPI, Houston, USA, pp. 1466–1467.
- Mikhail, J.S., 1970. Color variations with phase of selected regions of the lunar surface. *Moon* 2, 167–201.
- Minnaert, M., 1941. The reciprocity principle in lunar photometry. *Astrophys. J.* 93, 403–410.
- Mishchenko, M.I., Dlugach, J.M., 1993. Coherent backscatter and the opposition effect for E-type asteroids. *Planet. Space Sci.* 41, 173–181.
- Mishchenko, M.I., Dlugach, J.M., Yanovskij, E.G., Zakharchova, N.T., 1999. Bidirectional reflectance of flat, optically thick particulate layers: an efficient radiative transfer solution and applications to snow and soil surfaces. *J. Quant. Spectrosc. Radiat. Transfer* 63, 409–432.
- Mishchenko, M.I., Rosenbush, V.K., Kiselev, N.N., 2006. Weak localization of electromagnetic waves and opposition phenomena exhibited by high-albedo atmosphereless solar system objects. *Appl. Opt.* 45, 4459–4463.
- Mishchenko, M.I., Dlugach, J.M., Liu, Li, 2009a. Azimuthal asymmetry of the coherent backscattering cone: theoretical results. *Phys. Rev.* A80, 053824.
- Mishchenko, M., Dlugach, J., Liu, L., Rosenbush, V., Kiselev, N., Shkuratov, Y., 2009b. Direct solutions of the Maxwell equations explain opposition phenomena observed for high-albedo solar system objects. *Astrophys. J. Lett.* 705, L118–L122.
- Mitrofanov, I.G., 28 colleagues, 2010. Hydrogen mapping of the lunar South Pole using the LRO neutron detector experiment LEND. *Science* 330 (6003), 483–486.
- Morgan, T.H., Shemansky, D.E., 1991. Limits to the lunar atmosphere. *J. Geophys. Res.* 96, 1351–1367.
- Moroz, L.V., Eisenko, A.V., Semjonova, L.F., Pieters, C.M., 1993. Optical effects of regolith processes on S-type asteroids as simulated by laser impulse alteration of ordinary chondrite. *Lunar Planet. Sci. Conf.* 24th, LPI, Houston, USA, pp. 1011–1012.
- Morris, R., 1980. Origins and size distribution of metallic iron particles in lunar regolith. *Lunar Planet. Sci. Conf.* 11th, LPI, Houston, USA, pp. 1697–1712.
- Muinonen, K., 1989. Electromagnetic scattering by two interacting dipoles. In: Proceedings of the 1989 URSI International Symposium on Electromagnetic Theory, Stockholm. pp. 428–430.
- Muinonen, K., 2004. Coherent backscattering of light by complex random media of spherical scatterers: numerical solution. *Waves Random Media* 14, 365–388.
- Muinonen, K., Shkuratov, Yu., Ovcharenko, A., Piironen, J., Stankevich, D., Miloslavskaya, O., Keraenen, S., Josset, J.-L., 2002. The SMART-1 AMIE experiment: implication to the lunar opposition effect. *Planet. Space Sci.* 50 (14–15), 1339–1344.
- Munoz, O., Volten, H., de Haan, J., Vassen, W., Hovenier, J., 2000. Experimental determination of scattering matrices of olivine and Allende meteorite particles. *Astron. Astrophys.* 360, 777–788.
- Munoz, O., Volten, H., Hovenier, J.W., Shkuratov, Y.G., van der Zande, W.J., Waters, L.B.F.M., 2006. Experimental and computational study of light scattering by irregular dust particles with extreme refractive indices: hematite and rutile. *Astron. Astrophys.* 446, 525–535.
- Nakamura, Y., Dorman, J., Duennebier, F., Lammlein, D., Lathan, G., 1975. Shallow lunar structure determined from the passive seismic experiment. *Moon* 13, 3–15.
- Naranen, L., Parviainen, H., Muinonen, K., Josset, J.-L., Beauvivre, S., Pinet, P., Chevrel, S., Koschny, D., Grieber, B., Foing, B., 2010. Lunar single-scattering, porosity, and surface roughness characteristics with SMART-1/AMIE. In: Muinonen, K. (Ed.), *Proceedings of the Electromagnetic and Light Scattering XII*, June 28–July 2, 2010. Helsinki University, Finland, pp. 202–205.
- Neckel, H., 2000. Sun: spectral distribution. In: Cox, A.N. (Ed.), *Allen's Astrophysical Quantities* 4th ed. AIP Press; Springer, New York, pp. 353–355.
- Nicodemus, F.E., 1965. Directional reflectance and emissivity of an opaque surface. *Appl. Opt.* 4, 767–773.
- Noble, S., Pieters, C., Hiroi, T., Taylor, L., 2006. Using the modified Gaussian model to extract quantitative data from lunar soils. *J. Geophys. Res.* 111, E11009. doi:10.1029/2006JE002721.
- Noble, S., Pieters, C., Keller, L.P., 2007. An experimental approach to understanding the optical effects of space weathering. *Icarus* 192, 629–642.
- Nozette, S., 33 colleagues, 1994. The Clementine mission to the Moon: scientific overview. *Science* 266, 1835–1839.
- Nozette, S., Lichtenberg, C., Spudis, P., Bonner, R., Ort, W., Malaret, E., Robinson, M., Shoemaker, E., 1996. The Clementine bistatic radar experiment. *Science* 274, 1495–1498.
- Oberst, J., Preusker, F., Phillips, R.J., Watters, T.R., Head, J.W., Zuber, M.T., Solomon, S.C., 2010. The morphology of Mercury's Caloris basin as seen in MESSENGER stereo topographic models. *Icarus* 209, 230–238.
- O'Leary, B., Briggs, B., 1973. Optical properties of Apollo-12 Moon samples. *J. Geophys. Res.* 78 (5), 792–797.
- Oetking, P., 1966. Photometric studies of diffusely reflecting surfaces with applications to the brightness of the Moon. *J. Geophys. Res.* 71 (10), 2505–2513.
- Ohtake, M., 22 colleagues, 2009. The global distribution of pure anorthosites on the Moon. *Nature* 461 (7261), 236–240.
- Ong, L., Asphaug, E.I., Korycansky, D., Coker, R.F., 2010. Volatile retention from cometary impacts on the Moon. *Icarus* 207, 578–589.
- Opanasenko, N.V., Shkuratov, Y.G., 1994. Results of simultaneous polarimetry and photometry of the Moon. *Sol. Syst. Res.* 28 (4–5), 398–417.
- Opanasenko, A.N., Shkuratov, Y.G., Opanasenko, N.V., 2007. Topography of three localities on the Moon from combined Clementine and Hubble space telescope images. *Lunar Planet. Sci. Conf.* 38th, Abstract no. 1564, LPI, Houston, USA.
- Opanasenko, N.V., Opanasenko, A.N., Shkuratov, Y.G., Kaydash, V.G., Velikodsky, Y.I., Korokhin, V.V., 2009. The negative polarization parameters of the light scattered by the lunar surface: mapping. *Sol. Syst. Res.* 43, 210–214.
- Papike, J.J., Ryder, G., Shearer, C.K., 1998. Lunar samples. In: Papike, J.J. (Ed.), *Planetary Materials*. Mineralogical Society of America, Washington, DC, pp. 5.1–5.234.
- Petrov, D.V., Shkuratov, Y.G., Stankevich, D.G., Shevchenko, V.V., Kozlova, E., 2003. The area of cold traps on the lunar surface. *Sol. Syst. Res.* 37 (4), 260–265.
- Petrov, D.V., Synelnyk, E.N., Shkuratov, Yu.G., Videen, G., 2006. The T-matrix technique for calculations of scattering properties of ensembles of randomly oriented particles with different size. *J. Quant. Spectrosc. Radiat. Transfer* 102, 85–110.
- Petrov, D., Shkuratov, Y., Videen, G., 2007. Analytical light-scattering solution for Chebyshev particles. *J. Opt. Soc. Am. A* 24 (4), 1103–1119.
- Petrov, D., Shkuratov, Y., Videen, G., 2011. Electromagnetic wave scattering from particles of arbitrary shapes. *J. Quant. Spectrosc. Radiat. Transfer*. doi:10.1016/j.jqsrt.2011.01.036.
- Petrova, E.V., Tishkovets, V.P., Jockers, K., 2007. Modeling of opposition effects with ensembles of clusters: interplay of various scattering mechanisms. *Icarus* 188, 233–245.
- Pieters, C., 1978. A summary of spectral reflectance data. *Lunar Planet. Sci. Conf.* 9th, LPI, Houston, USA, pp. 2825–2849.
- Pieters, C.M., 1982. Copernicus crater central peaks: lunar mountain of unique composition. *Science* 215, 59–61.
- Pieters, C.M., 1983. Strength of mineral abortion features in the transmitted component in near-infrared light: first results from RELAB. *J. Geophys. Res.* 88, 9534–9544.
- Pieters, C.M., 1999. The Moon as a spectral calibration standard enabled by lunar samples: the Clementine example. In: *Proceedings of the Workshop on New Views of the Moon II: Understanding the Moon through the Integration of Diverse Datasets*, Abstract no. 8025, LPI, Houston, USA.
- Pieters, C.M., Taylor, L.A., 2003. Systematic global mixing and melting in lunar soil evolution. *Geophys. Res. Lett.* 30 (20), 2048. doi:10.1029/2003GL08212.
- Pieters, C., Fischer, E., Rode, O., Basu, A., 1993. Optical effects of space weathering: the role of the finest fraction. *J. Geophys. Res.* 98, 20,817–20,824.
- Pieters, C.M., Stankevich, D.G., Shkuratov, Y.G., Taylor, L.A., 2002. Statistical analysis of the links between lunar mare soil mineralogy, chemistry and reflectance spectra. *Icarus* 155, 285–298.
- Pieters, C.M., Shkuratov, Y.G., Kaydash, V.G., Stankevich, D.G., Taylor, L., 2006. Lunar soil characterization consortium analyses: pyroxene and maturity estimates derived from Clementine data. *Icarus* 184, 83–101.
- Pieters, C.M., Goswami, J.N., Clark, R.N., the M3 Science Team, 2009a. Character and spatial distribution of OH/H₂O on the surface of the Moon seen by M3 on Chandrayaan-1. *Science* 326, 568–572.
- Pieters, C.M., 19 colleagues, 2009b. The Moon Mineralogy Mapper (M3) on Chandrayaan-1. *Curr. Sci.* 96 (4), 500–505.
- Pieters, C.M. and 24 colleagues, 2009c. Mineralogy of the lunar crust in spatial context: First results from the Moon Mineralogy Mapper (M³). *Lunar Planet. Sci. Conf.* 40th, Abstract no. 2052, LPI, Houston, USA.
- Pieters, C.M. and 26 colleagues, 2010. Identification of a new spinel-rich lunar rock type by the Moon Mineralogy Mapper (M3). *Lunar Planet. Sci. Conf.* 41st, no. 1854, LPI Houston, USA.
- Pieters, C.M. and 25 colleagues, 2011. Mg-spinel lithology: a new rock-type on the lunar farside. *J. Geophys. Res., Planets*, 10.1029/2010JE003727.
- Pinet, P., Chevrel, S., Martin, P., 1993. Copernicus: a regional probe of the lunar interior. *Science* 260 (5109), 797–801.

- Pinet, P.C., Shevchenko, V.V., Chevrel, S.D., Daydou, Y., Rosemberg, C., 2000. Local and regional lunar regolith characteristics at Reiner Gamma Formation: Optical and spectroscopic properties from Clementine and Earth-based data. *J. Geophys. Res., Planets* 105 (E4), 9457–9475.
- Pinet, P., Cerroni, P., Josset, J.-L., Beauvivre, S., Chevrel, S., Muinonen, K., Langevin, Y., Barruci, M., De Santis, M., Shkuratov, Yu., Shevchenko, V., Planke, P., Hofmann, B., Josset, M., Ehrenfreund, P., Sodnik, P., Koschny, D., Almeida, M., Foing, B., 2005. The advanced Moon micro-imager experiment (AMIE) on Smart-1: scientific goals and expected results. *Planet. Space Sci.* 53 (13), 1309–1318.
- Pohn, H.A., Wildey, R.L., 1970. A photoelectric-photographic study of the normal albedo of the Moon (map, scale 1: 5 000 000). Geological Survey Professional Papers, No. 599-E.
- Pohn, H., Radin, H.W., Wildey, R.L., 1969. The Moon's photometric function near zero phase angle from Apollo 8 photography. *Astron. J. Lett.* 157 (3), 193–195.
- Poulet, F., Cuzzi, J., Cruikshank, D., Roush, T., Ore, C., 2002. Comparison between the Shkuratov and Hapke scattering theories for solid planetary surfaces: application to the surface composition of two Centaurs. *Icarus* 160, 313–324. doi:10.1006/icar.2002.6970.
- Prettyman, T.H., Hagerty, J.J., Feldman, W.C., Lawrence, D.J., Vaniman, D.T., McKinney, G.W., 2006. Elemental composition of the lunar surface: analysis of gamma ray spectroscopy data from Lunar Prospector. *J. Geophys. Res., Planets* 111, E12007. doi:10.1029/2005JE002656.
- Psarev, V., Ovcharenko, A., Shkuratov, Yu., Belskaya, I., Videen, G., 2007. Photometry of surfaces with complicated structure at extremely small phase angles. *J. Quant. Spectrosc. Radiat. Transfer* 106, 455–463.
- Qiu, J., Goode, P.R., Pallé, E., Yurchyshyn, V., Hickey, J., Montañés-Rodríguez, P., Chu, M.-C., Kolbe, E., Brown, C.T., Koonin, S.E., 2003. Earthshine and the Earth's albedo: 1. Earthshine observations and measurements of the lunar phase function for accurate measurements of the Earth's Bond albedo. *J. Geophys. Res.* 108, D22. doi:10.1029/2003JD003610 (ACL 12-1, CitelID 4709).
- Raitala, J., Kreslavsky, M., Shkuratov, Yu., Starukhina, L., Kaydash, V., 1999. Non-mare volcanism on the Moon: Characteristics from remote sensing data. *Lunar Planet. Sci. Conf.* 30th, No. 1457, LPI, Houston, USA.
- Robinson, M.S., Jolliff, B.L., 2002. Apollo 17 landing site: Topography, photometric corrections, and heterogeneity of the surrounding highland massifs. *J. Geophys. Res.* 107 (E11), 5110. doi:10.1029/2001JE001614.
- Robinson, M.S., Hapke, B.W., Garvin, J.B., Skillman, D., Bell III, J.F., Ulmer, M.P., Pieters, C.M., 2007. High resolution mapping of TiO₂ abundances on the Moon using the Hubble Space Telescope. *Geophys. Res. Lett.* 34, L13203. doi:10.1029/2007GL029754.
- Robinson, M.S., 22 colleagues, 2010. Lunar Reconnaissance Orbiter Camera (LROC) instrument overview. *Space Sci. Rev.* 150, 81–124.
- Robinson, M., Denevi, B., Sato, H., Hapke, B., Hawke, B., 2011. LROC WAC ultraviolet reflectance of the Moon. *Lunar Planet. Sci. Conf.* 42nd, #1842, LPI, Houston.
- Rosenberg, G.V., 1956. On albedo of colored turbid media. In: Collection Devoted to the Memory of Academician P.P. Lazarev. Moscow: Academic Science, USSR. pp. 132–142.
- Roth, J., 1983. Chemical sputtering. In: Behrisch, R. (Ed.), *Sputtering by Particle Bombardment II*. Springer, Berlin, pp. 91–146.
- Rougier, G., 1933. Photometry photoélectrique global de la Lune. *Ann. Obs. Strasbourg* 2, 205–399.
- Saal, A.E., Hauri, E.H., Cascio, M.L., Van Orman, J.A., Rutherford, M.C., Cooper, R.F., 2008. Volatile content of lunar volcanic glasses and the presence of water in the Moon's interior. *Nature* 454, 192–195.
- Saiki, K., Saito, K., Okuno, H., Suzuki, A., Yamanoi, Y., Hirata, N., Nakamura, R., 2008. Estimation of the lunar reflectance by ground-based observation using a tunable liquid-crystal filter telescope. *Earth Planets Space* 60, 417–424.
- Saito, Y., Yokota, S., Tanaka, T., Asamura, K., Nishino, M.N., Fujimoto, M., Tsunakawa, H., Shibuya, H., Matsushima, M., Shimizu, H., Takahashi, F., Mukai, T., Terasawa, T., 2008. Solar wind proton reflection at the lunar surface: low energy ion measurement by MAP-PACE onboard SELENE (KAGUYA). *Geophys. Res. Lett.* 35, L24205. doi:10.1029/2008GL036077.
- Sanin, A. and 25 colleagues, 2010. Mapping of lunar hydrogen according to the LEND neutron measurements onboard the NASA LRO. *Lunar Planet. Sci. Conf.* 41st, Abstract no. 2437, LPI, Houston, USA.
- Sharonov, V.V., 1964. The nature of the Planets. Gosud. Izd. Fiz. Mat. Lit. (1958: Priroda Planet) transl. by Israel Progr. Sci. Trans. 420 pp.
- Shestopalov, D.I., McFadden, L.A., Golubeva, L.F., Khomenko, V.M., Gasanova, L.O., 2008. Vestaoid surface composition from analysis of faint absorption bands in visible reflectance spectra. *Icarus* 195, 649–662.
- Shevchenko, V.V., Skobeleva, T.P., 1995. Abundance of the fine fraction of lunar soil according to remote-sensing data. *Astron. Vestn.* 29 (1), 84–93.
- Shevchenko, V.V., Pinet, P., Chevrel, S., 1993. Remote-sensing studies of immature lunar soils (Reiner-γ formation). *Sol. Syst. Res.* 27 (4), 16–30.
- Shkuratov, Y.G., 1981. Connection between the albedo and polarization properties of the Moon. Fresnel component of reflected light. *Sov. Astron.* 25 (4), 490–494.
- Shkuratov, Y.G., 1983. A model of the opposition effect in the brightness of airless cosmic bodies. *Sov. Astron.* 27 (5), 581–583.
- Shkuratov, Y.G., 1985. On the origin of the opposition effect and negative polarization for cosmic bodies with solid surface. In: *Astronomicheskii Circular*, No. 1400. Sternberg State Astronomical Institute, Moscow, pp. 3–6.
- Shkuratov, Y.G., 1987. Negative polarization of sunlight scattered from celestial bodies: interpretation of the wavelength dependence. *Sov. Astron. Lett.* 13 (3), 182–183.
- Shkuratov, Y., 1988. Diffraction model of the brightness surge of complex structure surfaces. *Kinem. Phys. Celest. Bodies* 4, 33–39.
- Shkuratov, Yu.G., Basilevsky, A.T., 1981. An attempt at mapping the parameter of surface micro porosity of lunar regolith: correlation between albedo and polarization properties of the Moon. *Lunar Planet. Sci.* 12th, LPI, Houston, USA, pp. 1981–1983.
- Shkuratov, Y.G., Opanasenko, N.V., 1990. On the limb polarimetric effect in the Moon discovered by Lyot. *Astron. Vestn.* 24 (4), 333–336.
- Shkuratov, Y.G., Opanasenko, N.V., 1992. Polarimetric and photometric study of the Moon: telescope observation and laboratory simulation: 2, the positive polarization. *Icarus* 99, 468–484.
- Shkuratov, Y.G., Helfenstein, P., 2001. The opposition effect and the quasi-fractal structure of regolith: I, theory. *Icarus* 152, 96–116.
- Shkuratov, Y.G., Bondarenko, N.V., 2001. Regolith thickness mapping of the Moon by radar and optical data. *Icarus* 149, 329–338.
- Shkuratov, Y., Grynk, Y., 2005. Scattering by semitransparent particles of different shapes and media consisting of these particles in geometric optics approximation: consequences for photometry and spectroscopy of the planetary regoliths. *Icarus* 173, 16–28.
- Shkuratov, Y., Zubko, E., 2008. Comment on "Modeling of opposition effects with ensembles of clusters: Interplay of various scattering mechanisms" by Elena V. Petrova, Victor P. Tishkovets, Klaus Jockers, 2007 [Icarus 188, 233–245]. *Icarus* 194, 850–852.
- Shkuratov, Y.G., Opanasenko, N.V., Kreslavsky, M.A., 1992. Polarimetric and photometric properties of the Moon: telescope observation and laboratory simulation. 1. The negative polarization. *Icarus* 95, 283–299.
- Shkuratov, Y., Starukhina, L., Kreslavsky, M., Opanasenko, N., Stankevich, D., Shevchenko, V., 1994a. Principle of perturbation invariance in photometry of atmosphereless celestial bodies. *Icarus* 109, 168–190.
- Shkuratov, Y.G., Muinonen, K., Bowell, E., Lumme, K., Peltoniemi, J., Kreslavsky, M.A., Stankevich, D.G., Tishkovets, V.P., Opanasenko, N.V., Melkumova, L.Ya., 1994b. A critical review of theoretical models for the negative polarization of light scattered by atmosphereless solar system bodies. *Earth Moon Planets* 65 (3), 201–246.
- Shkuratov, Y.G., Melkumova, L.Y., Opanasenko, N.V., Stankevich, D.G., 1996. Phase dependence of the color Index of solid surfaces of celestial bodies. *Sol. Syst. Res.* 30, 71–79.
- Shkuratov, Y., Kreslavsky, M., Ovcharenko, A., Stankevich, D., Zubko, E., Pieters, C., Arnold, G., 1999a. Opposition effect from Clementine data and mechanisms of backscatter. *Icarus* 141, 132–155.
- Shkuratov, Y., Starukhina, L., Hoffmann, H., Arnold, G., 1999b. A model of spectral albedo of particulate surfaces: implications for optical properties of the Moon. *Icarus* 137, 235–246.
- Shkuratov, Yu.G., Kaydash, V.G., Opanasenko, N.V., 1999c. Iron and titanium abundance and maturity degree distribution on lunar nearside. *Icarus* 137, 222–234.
- Shkuratov, Yu.G., Starukhina, L.V., Kaydash, V.G., Bondarenko, N.V., 1999d. Distribution of ³He abundance over the lunar nearside. *Sol. Syst. Res.* 33 (5), 409–420.
- Shkuratov, Yu.G., Kaydash, V.G., Kreslavsky, M.A., Opanasenko, N.V., 2001. Absolute calibration of the Clementine UVVis data: comparison with ground-based observation of the Moon. *Sol. Syst. Res.* 35 (1), 29–34.
- Shkuratov, Yu., Ovcharenko, A., Zubko, E., Miloslavskaya, O., Nelson, R., Smythe, W., Muinonen, K., Piironen, J., Rosenbush, V., Helfenstein, P., 2002. The opposition effect and negative polarization of structurally simulated planetary regoliths. *Icarus* 159, 396–416.
- Shkuratov, Yu.G., Petrov, D.V., Videen, G., 2003a. Classical photometry of pre-fractal surfaces. *J. Opt. Soc. Am.* 20 (11), 2081–2092.
- Shkuratov, Yu., Stankevich, D., Kaydash, V., Omelchenko, V., Pieters, C., Pinet, P., Chevrel, S., Daydou, Y., Foing, B., Sodnik, Z., Josset, J.-L., Taylor, L., Shevchenko, V., 2003b. Composition the lunar surface as will be seen from SMART-1: simulation using Clementine data. *J. Geophys. Res., Planets* 108 (E4) (1–1–12).
- Shkuratov, Yu., Ovcharenko, A., Zubko, E., Volten, H., Muñoz, O., Videen, G., 2004. The negative polarization of light scattered from particulate surfaces and of independently scattering particles. *J. Quant. Spectrosc. Radiat. Transfer* 88, 267–284.
- Shkuratov, Yu., Kaydash, V., Stankevich, D., Pinet, P., Chevrel, S., Daydou, Y., 2005a. Derivation of elemental abundance maps at intermediate resolution from optical interpolation of Lunar Prospector Gamma-Ray spectrometer data. *Planet. Space Sci.* 53, 1287–1301.
- Shkuratov, Yu.G., Kaydash, V.G., Pieters, C., 2005b. Lunar clinopyroxene and plagioclase: surface distribution and composition. *Sol. Syst. Res.* 39 (4), 255–266.
- Shkuratov, Yu.G., Stankevich, D.G., Petrov, D.V., Pinet, P.C., Cord, A.M., Daydou, Y.H., 2005c. Interpreting photometry of regolith-like surfaces with different topographies: shadowing and multiple scatter. *Icarus* 173, 3–15.
- Shkuratov, Yu., Bondarenko, S., Ovcharenko, A., Pieters, C., Hiroi, T., Volten, H., Munoz, O., Videen, G., 2006. Comparative studies of the reflectance and degree of linear polarization of particulate surfaces and independently scattering particles. *J. Quant. Spectrosc. Radiat. Transfer* 100 (1–3), 340–358.
- Shkuratov, Yu., Kaydash, V.G., Starukhina, L.V., Pieters, C., 2007a. Lunar surface agglutinates: mapping composition anomalies. *Sol. Syst. Res.* 41, 177–185.
- Shkuratov, Yu., Opanasenko, N., Zubko, E., Grynk, Ye., Korokhin, V., Pieters, C., Videen, G., Mall, U., Opanasenko, A., 2007b. Multispectral polarimetry as a tool to investigate texture and chemistry of lunar regolith particles. *Icarus* 187, 406–416.

- Shkuratov, Yu., Opanasenko, N., Opanasenko, A., Zubko, E., Bondarenko, Y., Kaydash, V., Videen, G., Velikodsky, Yu., Korokhin, V., 2008. Polarimetric mapping of the Moon at a phase angle nearby minimum of polarization degree. *Icarus* 198, 1–6.
- Shkuratov, Yu., Kaydash, V., Gerasimenko, S., Opanasenko, N., Velikodsky, Yu., Korokhin, V., Videen, G., Pieters, C., 2010. Probable swirls detected as photometric anomalies in Oceanus Procellarum. *Icarus* 208, 20–30.
- Shorthill, R.W., Saari, J.M., Baird, F.E., LeCompte, J.R., 1969. Photometric properties of selected lunar features. NASA Contractor Report CR-1429.
- Shoshany, M., 1991. The equifinality of bidirectional reflectance distribution functions of various microstructures. *Int. J. Remote Sensing* 12 (11), 2267–2281.
- Sridharan, R., Ahmed, S.M., Das, T.P., Sreelatha, P., Pradeepkumar, P., Naik, N., Supriya, P., 2010. "Direct" evidence for water (H_2O) in the sunlit lunar ambience from CHACE on MIP of Chandrayaan 1. *Planet. Space Sci.* 58, 947–950.
- Stankevich, D.G., Shkuratov, Yu.G., 2000. The shadowing effect in regolith-type media: numerical modeling. *Sol. Syst. Res.* 34 (4), 285–294.
- Stankevich, D.G., Shkuratov, Y.G., Petrov, D.V., 2001. Estimation of the area of the perpetually shaded lunar surface. *Sol. Syst. Res.* 35 (6), 452–457.
- Stankevich, D.G., Shkuratov, Yu.G., 2002. Multiple scattering of light in regolith-like media: geometric optics approximation. *Sol. Syst. Res.* 36 (5), 409–416.
- Stankevich, D., Shkuratov, Yu., 2004. Monte Carlo ray-tracing simulation of light scattering in particulate media with optically contrast structure. *J. Quant. Spectrosc. Radiat. Transfer* 87 (3–4), 289–296.
- Stankevich, D., Shkuratov, Yu., Muinonen, K., 1999. Shadow-hiding effect in ingomogeneous and layered particulate media. *J. Quant. Spectrosc. Radiat. Transfer* 63 (2–6), 445–458.
- Stankevich, D.G., Shkuratov, Yu.G., Muinonen, K.O., Miloslavskaya, O.V., 2000. Simulation of shadings in systems of opaque particles. *Opt. Spectrosc.* 88 (4), 619–622.
- Stankevich, D., Shkuratov, Yu., Grynko, E., Muinonen, K., 2003. Computer simulation of multiple scattering in random gaussian media. *J. Quant. Spectrosc. Radiat. Transfer* 76 (1), 1–16.
- Stankevich, D., Istomina, L., Shkuratov, Yu., Videen, G., 2007a. Electromagnetic phase differences in the coherent backscattering enhancement mechanism for random media consisting of large non-transparent spheres. *Appl. Opt.* 46 (9), 1562–1567.
- Stankevich, D., Istomina, L., Shkuratov, Yu., Videen, G., 2007b. The coherent backscattering effects in a random medium as calculated using a ray tracing technique for large non-transparent spheres. *J. Quant. Spectrosc. Radiat. Transfer* 106, 509–519.
- Starukhina, L.V., Shkuratov, Y.G., 2000. The lunar poles: water ice or chemically trapped hydrogen? *Icarus* 147, 585–587.
- Starukhina, L.V., Shkuratov, Y.G., 2001. A theoretical model of lunar optical maturation: effects of submicroscopic reduced iron and particle size variations. *Icarus* 152, 275–281.
- Starukhina, L.V., Shkuratov, Y.G., 2004. Swirls on the Moon and Mercury: meteoroid swarm encounters as a formation mechanism. *Icarus* 167 (1), 136–147.
- Starukhina, L.V., Shkuratov, Y.G., Skorik, S.K., 1999. Spread of condense products in a regolith-like medium: estimates and laboratory modeling. *Sol. Syst. Res.* 33 (3), 212–215.
- Stubbs, T.J., Vondrak, R.R., Farrell, W.M., 2006. A dynamic fountain model for lunar dust. *Adv. Space Res.* 37, 59–66.
- Sunshine, J.M., Farnham, T.L., Feaga, L.M., Groussin, O., Merlin, F., Milliken, R.E., A'Hearn, M.F., 2009. Temporal and spatial variability of lunar hydration as observed by the Deep Impact Spacecraft. *Science* 326, 565–568.
- Sunshine, J.M., Besse, S., Petro, N.E., Pieters, C.M., Head, J.W., Taylor, L.A., Klima, R.L., Isaacson, P.J., Boardman, J.W., Clark, R.C., the M3 Team, 2010. Hidden in plain sight: spinel-rich deposits on the nearside of the Moon as revealed by Moon Mineralogy Mapper (M3). *Lunar Planet. Sci. Conf.* 41st, Abstract no. 1508, LPI, Houston, USA.
- Sytinskaya, N.N., Sharonov, V.V., 1952. Studying of reflectivity of lunar surface. *Sci. Notes Leningrad Univ.* 153, 114–154.
- Sytinskaya, N.N., 1964. Albedo values for separate features of the lunar surface. *Sov. Astron.* 7 (6), 827–828.
- Taylor, L., 1994. Helium-3 on the Moon: model assumptions and abundances. *Engineering Construction & Operations in Space IV*, ASCE Publication, Proceedings of Space, vol. 94, pp. 678–686.
- Taylor, L.A., Mao, H.-K., Bell, P.B., 1973. "Rust" in the Apollo-16 rocks. In: *Proceedings of the Fourth Lunar and Planetary Science Conference; Geochim. Cosmochim. Acta. Suppl.* 4(1), 829–839.
- Taylor, L.A., Rossman, G.R., Qi, Q., 1995. Where has all the lunar water gone? *Lunar Planet. Sci.* 36th, LPI, Houston, pp. 1399–1400.
- Taylor, L.A., Pieters, C.M., Morris, R.V., Keller, L.P., McKay, D.S., Parchen, A., Wentworth, S.J., 1999. Integration of the chemical and mineralogical characteristics of lunar soils with reflectance spectroscopy. *Lunar Planet. Sci. Conf.* 30th, Abstract no. 1859, LPI, Houston, USA.
- Taylor, L.A., Pieters, C.M., Morris, R.V., Keller, L.P., McKay, D.S., 2001. Lunar mare soils: space weathering and the major effects of surface correlated nanoparticle Fe. *J. Geophys. Res.* 106, 27,985–28,000.
- Taylor, S.R., Pieters, C.M., MacPherson, G.J., 2006. Earth–Moon system, planetary science, and lessons learned. *Rev. Mineral. Geochem.* 60 (1), 657–704.
- Thompson, T.W., 1987. High-resolution lunar radar at 70-cm wavelength. *Earth Moon Planets* 37, 59–70.
- Tishkovets, V., Mishchenko, M., 2009. Approximate calculation of coherent backscattering for semi-infinite discrete random media. *J. Quant. Spectrosc. Radiat. Transfer* 110, 139–145.
- Tompkins, S., Pieters, C.M., 1999. Mineralogy of the lunar crust: results from Clementine. *Meteorit. Planet. Sci.* 34, 25–41.
- Trowbridge, T.S., 1984. Rough-surface retroreflection by focusing and shadowing below a randomly undulating interface. *J. Opt. Soc. Am. A1* (10), 1019–1027.
- Tyynelä, J., Zubko, E., Muinonen, K., Videen, G., 2007. Interrelating angular scattering characteristics to internal electric fields for wavelength-scale spherical particles. *J. Quant. Spectrosc. Radiat. Transfer* 106, 520–534.
- van Diggelen, J., 1951. A photometric investigation of the slopes and heights of the ranges of hills in the maria of the Moon. *Bull. Astron. Instrum. Netherlands* 11, 283–289.
- Velikodsky, Y.I., Opanasenko, N.V., Akimov, L.A., Korokhin, V.V., Shkuratov, Y.G., Kaydash, V.G., Videen, G., Ehgamberdiev, Sh.A., Berdalieva, N.E., 2011. New Earth-based absolute photometry of the Moon. *Icarus* 10.1016/j.icarus.2011.04.021.
- Videen, G., Wetmore, A., Petre, M., Shkuratov, Y., 2006. Analytic description of enhanced backscattering and negative polarization from a cloud of dipoles. *J. Quant. Spectrosc. Radiat. Transfer* 100 (1–3), 406–414.
- Watson, K., Murray, B.C., Brown, H., 1961. The behavior of volatiles on the lunar surface. *J. Geophys. Res.* 66, 3033–3045.
- Weitz, C.A., Head, J.W., Pieters, C.M., 1998. Lunar regional dark mantle deposits: geologic, multispectral, and modeling studies. *J. Geophys. Res.* 103, 22,725–22,759.
- Whitaker, E.A., 1972. Lunar color boundaries and their relationship with topographic features: a preliminary survey. *Moon* 4, 348–355.
- Wildey, R.L., 1978. The Moon in Heiligenchein. *Science* 200 (4347), 1265–1266.
- Wildey, R.L., Pohn, H.A., 1964. Detailed photoelectric photometry of the Moon. *Astron. J.* 69 (8), 619–634.
- Wittenberg, L., Santarius, J., Kulchinski, G., 1986. Lunar source of 3He for fusion power. *Fusion Technol.* 10, 167–178.
- Wöhler, C., Berezhnoy, A., Evans, R., 2009. Estimation of lunar elemental abundances using Clementine UVVIS+NIR data. In: *Proceedings of the EPSC Abstracts*, vol. 4, EPSC2009-263.
- Wolff, M., 1980. Theory and application of the polarization-albedo rules. *Icarus* 44, 780–792.
- Yamamoto, S., Nakamura, R., Matsunaga, T., Ogawa, Y., Ishihara, Y., Morota, T., Hirata, N., Ohtake, M., Hiroi, T., Yokota, Y., Haruyama, J., 2010. Possible mantle origin of olivine around lunar impact basins detected by SELENE. *Nat. Geosci.* 10.1038/ngeo897.
- Yan, B., Wang, R., Gan, F., Wang, Z., 2010. Minerals mapping of the lunar surface with Clementine UVVIS/NIR data based on spectra unmixing method and Hapke model. *Icarus* 208, 11–19.
- Yokota, Y., Matsunaga, T., Ohtake, M., Haruyama, J., Ogawa, Y., Nakamura, R., Honda, C., Morota, T., Saiki, K., Kawabe, S., Nagasawa, K., Kitazato, K., LISM Working Group, 2009. Lunar phase curve at VIS/NIR wavelength observed by Selena spectral profiler. *Lunar Planet. Sci. Conf.* 40th, Abstract no. 2525, LPI, Houston, USA.
- Zeller, E.J., Ronca, L.B., Levy, P.W., 1966. Proton-induced hydroxyl formation on the lunar surface. *J. Geophys. Res.* 71, 4855–4860.
- Zellner, B., Leake, M., Lebertre, T., Duseaux, M., Dollfus, A., 1977. The asteroid albedo scale. I. Laboratory polarimetry of meteorites. *Lunar Planet. Sci. Conf.* 8th, LPI, Houston, USA, pp. 1091–1110.
- Zubko, E., Shkuratov, Yu., Kiselev, N., Videen, G., 2006. DDA simulations of light scattering by small irregular particles with various structure. *J. Quant. Spectrosc. Radiat. Transfer* 101, 416–434.
- Zubko, E., Shkuratov, Yu., Mishchenko, M., Videen, G., 2008. Light scattering in a finite multi-particle system. *J. Quant. Spectrosc. Radiat. Transfer* 109, 2195–2206.
- Zubko, E., Kimura, H., Shkuratov, Y., Muinonen, K., Yamamoto, T., Okamoto, H., Videen, G., 2009. Effect of absorption on light scattering by agglomerated debris particles. *J. Quant. Spectrosc. Radiat. Transfer* 110 (14–16), 1741–1749.
- Zubko, E., Videen, G., Shkuratov, Y., Muinonen, K., Yamamoto, T., 2011. The Umov effect for single irregularly shaped particles with size comparable with wavelength. *Icarus* 212 (1), 403–415.